Flexible Optical Pressure Sensor Based on Bending-Loss-Induced Intensity Modulation with Inverse-Model-Based Pressure Reconstruction in Polymer Optical Fibers Embedded in Elastomeric Substrates

by

Alberto ALONSO ROMERO

THESIS PRESENTED TO ÉCOLE DE TECHNOLOGIE SUPÉRIEURE
IN PARTIAL FULFILLEMENT FOR THE DEGREE OF
DOCTOR OF PHILOSOPHY
Ph.D.

MONTREAL, APRIL 24, 2026

ÉCOLE DE TECHNOLOGIE SUPÉRIEURE
UNIVERSITÉ DU QUÉBEC

BOARD OF EXAMINERS

THIS THESIS HAS BEEN EVALUATED

BY THE FOLLOWING BOARD OF EXAMINERS

Mr. Bora Ung, Thesis Supervisor
Department of Electrical Engineering, École de Technologie Supérieure

Mr. Jean-Marc Lina, Thesis Co-supervisor
Department of Electrical Engineering, École de Technologie Supérieure

Mr. Kaiwen Zhang, President of the Board of Examiners
Department of Software Engineering and IT, École de Technologie Supérieure

Mr. Georges Kaddoum, Member of the jury
Department of Electrical Engineering, École de Technologie Supérieure

Mr. Yann Facchinello, External Evaluator
Zimmer Biomet

THIS THESIS WAS PRESENTED AND DEFENDED

IN THE PRESENCE OF A BOARD OF EXAMINERS AND PUBLIC

MARCH 10, 2026

AT ÉCOLE DE TECHNOLOGIE SUPÉRIEURE

ACKNOWLEDGMENTS

After several years of work, effort, and personal sacrifice, this doctoral work marks the end of a very demanding and meaningful stage in my academic and personal life. While this achievement may appear to be an individual one, it would not have been possible without the support, guidance, and help of many people and institutions who accompanied me throughout this process.

I would like to thank my research director, Professor Bora Ung, and my co-director, Professor Jean-Marc Lina, for giving me the opportunity to be part of this challenging research environment. I am grateful for their guidance, patience, and continuous support during the development of this doctoral work, as well as for the trust they placed in me throughout the process. Their commitment to research and their enthusiasm for science played an important role in the completion of this thesis and in my academic and professional development.

Also, I would like to thank the Fonds de recherche du Québec – Nature et technologies (FRQNT) for the financial support provided during a significant part of my doctoral studies. I also thank the École de technologie supérieure (ÉTS) for believing in me and for allowing me to pursue my PhD within its academic environment, as well as for providing the institutional support that made this work possible.

Similarly, I would like to thank my lab colleagues and friends for sharing their knowledge and experience with me, and for being present during both the hardest and the best moments of this stage. In particular, I thank Koffi, Camila, Karina, and Mostafa for their advice, support, and many conversations that helped make long and demanding workdays easier. The professional and personal exchanges with them are among the most valuable experiences I take from this process.

My deepest thanks go to Kendra for her unconditional support, generosity, and patience over these years, especially during the most intense and chaotic periods of the final stage of this

project. I truly value what we have learned together as partners in life and in adventure, as well as the encouragement and trust she gave me day after day. This achievement is also hers, and I share it with her with love.

I am deeply grateful to my family, whose support has been essential since the beginning of this journey. I thank my mother, Glorinela, for her unconditional love, strength, and the sacrifices she has made throughout her life, as well as for the values of responsibility and perseverance she taught me and that have guided my path. I thank my father, Jacobo, for the discipline, guidance, and constant support that played an important role in shaping my character. I also thank my sisters, Berenice and Diana, my nephews Héctor and Bris, and Dennys for their affection, support, and encouragement, even from a distance. This achievement also reflects their presence and support, and I share it with them with deep appreciation.

Finally, this academic path began many years ago with a simple but powerful idea passed on by my grandfather: that learning and knowledge are some of the most valuable tools we have to grow, understand, and move forward. That early influence sparked the curiosity that eventually led me to pursue the highest level of academic studies, and it continues to guide my life today.

With affection and gratitude.

Conception, caractérisation et validation expérimentale de preuve de concept d'un capteur de pression optique flexible basé sur la modulation d'intensité induite par les pertes par courbure dans des fibres optiques polymères intégrées dans des substrats élastomériques

Alberto ALONSO ROMERO

RÉSUMÉ

Les capteurs de pression flexibles capables de s'adapter à des surfaces non planes et de permettre la cartographie spatiale de la pression suscitent un intérêt croissant dans divers domaines de l'ingénierie. Toutefois, les approches de détection électronique conventionnelles présentent souvent des contraintes techniques liées aux interférences électromagnétiques, à la complexité du câblage, à la dérive de calibration et à la dégradation des performances sous des sollicitations mécaniques répétées, en particulier lorsqu'elles sont mises en œuvre sur des surfaces étendues ou dans des systèmes de détection distribuée. Ces défis ont motivé l'exploration de mécanismes de transduction alternatifs favorisant l'évolutivité et la stabilité du signal.

Cette thèse présente la conception et l'évaluation expérimentale d'une plateforme flexible de détection de pression optique basée sur des mécanismes de pertes par courbure dans des fibres optiques polymères, couplée à un cadre de modélisation inverse pour la localisation spatiale et l'estimation de la pression. Le système développé se compose de coussins élastomériques flexibles intégrant des fibres optiques polymères disposées selon des configurations en grille, de circuits d'acquisition optoélectroniques à faible coût pour l'excitation optique et l'acquisition du signal, ainsi que d'un ensemble de modèles mathématiques reliant les variations mesurées de l'intensité lumineuse à la pression appliquée.

L'approche proposée intègre un modèle inverse basé sur la pseudoinverse de Moore–Penrose afin de déterminer la localisation des événements de pression appliquée, ainsi que des modèles d'estimation spécifiques à chaque point permettant de reconstruire des cartes de pression bidimensionnelles. Le système a été développé et évalué selon une stratégie expérimentale progressive, allant de configurations de détection fondamentales vers une grille multipoints capable de représenter des distributions spatiales de pression sur la surface de détection. La caractérisation expérimentale a été réalisée sous des conditions de chargement statique contrôlées, permettant une évaluation quantitative des performances de localisation, des erreurs d'estimation de la pression et de la cohérence de la reconstruction.

Les résultats indiquent que le système proposé est capable de générer des réponses spatiales cohérentes et interprétables sous des sollicitations mécaniques, en utilisant des matériaux et des composants optoélectroniques à faible coût. Les performances de localisation présentent un comportement stable en fonction de la résolution de la grille, tandis que la précision de l'estimation de la pression dépend fortement d'une localisation spatiale correcte. Les analyses quantitatives confirment la relation directe entre l'erreur de localisation et la qualité de l'estimation, soulignant le rôle de la cartographie spatiale dans les performances des systèmes

de détection de pression optique. Dans ce contexte, l'intégration d'une modélisation physique avec des estimateurs calibrés par point a permis la reconstruction de cartes de pression sans recourir à des approches basées sur l'apprentissage.

L'évaluation expérimentale a également mis en évidence des défis clés liés à l'atténuation optique, au bruit électronique et au couplage mécanique au sein du substrat encapsulant, qui influencent la sensibilité et la précision des mesures, en particulier à proximité des bords du capteur et dans les zones intermédiaires. Loin de diminuer la contribution de ce travail, ces facteurs permettent de définir les limites opérationnelles du prototype actuel et d'identifier les aspects critiques influençant le comportement du système.

Dans l'ensemble, ce travail établit une preuve de concept à l'échelle du laboratoire ainsi qu'un cadre analytique pour le développement et l'évaluation de systèmes flexibles de détection de pression optique. Les résultats confirment la faisabilité de l'intégration d'une acquisition optoélectronique à faible coût avec une reconstruction basée sur des modèles inverses afin de réaliser une détection de pression distribuée, tout en établissant une base structurée pour de futures améliorations en matière de matériaux, de cohérence de fabrication et de scalabilité des modèles.

Mots-clés: capteur de pression optique flexible; fibres optiques polymères; détection par pertes de courbure; optoélectronique à faible coût; modélisation inverse; estimation de la pression; cartographie de la pression

Design, characterization, and proof-of-concept experimental validation of a flexible optical pressure sensor based on bending-loss-induced intensity modulation in polymer optical fibers embedded in elastomeric substrates

Alberto ALONSO ROMERO

ABSTRACT

Flexible pressure sensors capable of adapting to non-planar surfaces and enabling spatial pressure mapping are of growing interest across diverse engineering domains. However, conventional electronic sensing approaches often face technical constraints such as electromagnetic interference, wiring complexity, calibration drift, and performance degradation under repeated mechanical loading, particularly when implemented across extended or distributed sensing areas. These challenges have motivated the exploration of alternative transduction mechanisms to improve scalability and signal stability.

This thesis presents the design and experimental evaluation of a flexible optical pressure-sensing platform based on bending-loss mechanisms in polymer optical fibers, coupled with an inverse-modeling framework for spatial localization and pressure estimation. The developed system consists of flexible elastomeric pads with embedded polymer optical fibers arranged in grid configurations, low-cost optoelectronic acquisition circuits for optical excitation and signal acquisition, and a set of mathematical models that relate measured light-intensity variations to applied pressure.

The proposed approach integrates an inverse model based on the Moore–Penrose pseudoinverse to determine the location of applied pressure events, along with point-specific estimation models used to reconstruct two-dimensional pressure maps. The system was developed and assessed through a progressive experimental strategy, starting from fundamental sensing configurations and advancing toward a multipoint grid capable of capturing spatial pressure distributions across the sensing area. Experimental characterization was performed under controlled static loading conditions, allowing the quantitative assessment of localization performance, pressure estimation errors, and reconstruction consistency.

The findings indicate that the proposed system can generate consistent and interpretable spatial responses under mechanical loading using low-cost materials and optoelectronic components. Localization performance showed stable behavior relative to the grid resolution, while pressure estimation accuracy was strongly dependent on correct spatial localization. Quantitative analyses confirmed the direct relationship between localization error and estimation quality, underscoring the role of spatial mapping in the performance of optical pressure-sensing systems. In this context, the integration of physical modeling with calibrated point-based estimators supported pressure map reconstruction without relying on learning-based approaches.

The experimental evaluation also revealed key challenges associated with optical attenuation, electronic noise, and mechanical coupling within the encapsulating substrate, affecting

sensitivity and measurement precision, particularly near sensor edges and intermediate locations. Rather than detracting from the overall contribution, these factors help define the operational boundaries of the current prototype and identify critical aspects influencing system behavior.

Overall, this work establishes a laboratory-scale proof of concept and an analytical framework for the development and evaluation of flexible optical pressure-sensing systems. The results confirm the feasibility of integrating low-cost optoelectronic acquisition with inverse-model-based reconstruction to achieve distributed pressure sensing, while establishing a structured foundation for future improvements in materials, fabrication consistency, and model scalability.

Keywords: flexible optical pressure sensor; polymer optical fibers; bending-loss sensing; low-cost optoelectronics; inverse modeling; pressure estimation; pressure mapping

TABLE OF CONTENTS

Page

LIST OF TABLES

Page

LIST OF FIGURES

Page

LIST OF ABREVIATIONS

AgNW	Silver nanowire
CNN	Convolutional neural network
CNT	Carbon nanotube
DAQ	Data acquisition
EMI	Electromagnetic interference
e-skin	Electronic skin
FBG	Fiber Bragg grating
FET	Field-effect transistor
FN	False negative
FP	False positive
FPR	False positive rate
GOF	Goodness of fit
IP	Intermediate point
k-NN	k-Nearest neighbor
LED	Light-emitting diode
MAE	Mean absolute error
ML	Machine learning
MLP	Multilayer perceptron
MRI	Magnetic resonance imaging
OFDR	Optical frequency domain reflectometry
OFET	Organic field-effect transistor
OF	Optical fiber
P(VDF-TrFE)	Poly(vinylidene fluoride-co-trifluoroethylene)
PC	Polycarbonate

PCB	Printed circuit board
PDMS	Polydimethylsiloxane
PEN	Polyethylene naphthalate
PET	Polyethylene terephthalate
PI	Polyimide
PMMA	Poly(methyl methacrylate)
POF	Plastic optical fiber
PP	Pressure point
PTFE	Polytetrafluoroethylene
PU	Polyurethane
PU-OF	Polyurethane optical fiber
PVDF	Polyvinylidene fluoride
PZT	Lead zirconate titanate
RFI	Radio-frequency interference
RMSE	Root mean square error
ROC	Receiver operating characteristic
RSD	Relative standard deviation
SVM	Support vector machine
TIA	Transimpedance amplifier
TIR	Total internal reflection
TN	True negative
TP	True positive
UV	Ultraviolet

LIST OF SYMBOLS

%	percentage
°C	degree Celsius
µA	microampere
arb.unit	arbitrary unit
cm	centimeter
dB	decibel
Hz	hertz
kPa	kilopascal
mA	milliampere
min	minute
mm	millimeter
mmHg	millimeters of mercury
MPa	megapascal
ms	millisecond
mV	millivolt
N	newton
nA	nanoampere
nm	nanometer
Pa	pascal
V	volt
W	watt
G	system response matrix
G^t	transpose of matrix G
G_i^+	Moore-Penrose pseudoinverse matrix at pressure level i

R	inverse model response vector
R_i	inverse model response vector at pressure level i
R_{mean}	mean inverse model response vector
R_{i^*}	maximum value of R_{mean}
P	pressure level applied
$\hat{P}$	estimated maximum pressure of point i
P_{sca}	scaled pressure vector
a_i	slope coefficient of the linear pressure estimation model at point i
b_i	offset coefficient of the linear pressure estimation model at point i
a_n	polynomial coefficient of order n
$f(x)$	polynomial fitting function to model sensor response
n	polynomial order
x	independent variable
v_{in}	input voltage vector
$\bar{v}_{in}$	mean input voltage vector
$\bar{v}_{exp}$	mean experimental input voltage vector
γ	Lorentzian half-width value

INTRODUCTION

Flexible pressure sensors have become essential components in modern sensing systems due to their ability to adhere to irregular surfaces, withstand repeated deformation, and enable distributed or multi-point monitoring in a wide range of engineering contexts. The growing demand for lightweight, low-power, and mechanically flexible sensing platforms has been accelerated by advances in soft materials, micro/nanostructured interfaces, and emerging fabrication techniques. Recent reviews highlight persistent engineering challenges in this field, including mechanical crosstalk in dense sensor arrays, environmental sensitivity, calibration drift, and fundamental trade-offs between sensitivity, dynamic range, and robustness (Y. Guo et al., 2024; Ruth et al., 2020). Taken together, these factors have encouraged the development of alternative transduction mechanisms aimed at improving signal stability, scalability, and long-term reliability compared to conventional electronic approaches.

Among the most widely implemented transduction mechanisms, conventional electronic pressure sensors, such as piezoresistive, capacitive, and piezoelectric devices, remain commonly used despite being vulnerable to electromagnetic interference, parasitic effects, complex wiring architectures, and performance degradation under repeated mechanical loading. These constraints become particularly significant when designing distributed or quasi-distributed systems intended to operate over extended surfaces or in electrically noisy environments (Yan Huang et al., 2019; Yuan et al., 2024). As the need for reliable pressure mapping increases in areas such as soft robotics, smart surfaces, and wearable technologies, these constraints underscore the need for sensing approaches that are resistant to electromagnetic disturbances and support more scalable system integration.

Optical pressure sensing, particularly approaches based on bending-loss mechanisms in polymer fibers, has emerged as a promising alternative to electronic transduction. Optical systems inherently address several of these limitations, offering rapid response times and can be fabricated from soft, deformable materials (Gan et al., 2024; D. Xu et al., 2025). Moreover, recent work has demonstrated that optical fibers or waveguides, arranged either in crossing

configurations or in parallel networks, can enable two-dimensional pressure mapping with reduced wiring complexity and adjustable sensitivity (Jeroen et al., 2010). Nevertheless, challenges remain in the design of low-cost optoelectronic acquisition systems, the integration of flexible optical fibers into elastomeric substrates, and the development of computational frameworks capable of reconstructing pressure distributions from sparse optical measurements.

This thesis investigates these challenges by demonstrating a proof-of-concept optical pressure-sensing platform based on bending-loss mechanisms and inverse modeling. Flexible pressure-sensing systems are valuable across multiple engineering domains, including clinical monitoring, soft robotics, wearable technologies, and industrial inspection, where the ability to capture spatial pressure patterns is essential. The present work focuses on developing and validating key aspects associated with optical transduction, signal acquisition, and spatial pressure reconstruction using fiber-based sensors. This includes elements related to optoelectronic acquisition circuits, reconstruction strategies, and the experimental evaluation of fiber-embedded elastomeric pads. Emphasis is placed on sensing principles, system integration, and quantitative characterization of localization and pressure-reconstruction performance under controlled laboratory loading conditions.

The general objective of this research is to design, integrate, and establish a flexible optical pressure-sensing platform that combines low-cost optoelectronic acquisition with an inverse-modeling approach for spatial localization and two-dimensional pressure reconstruction based on bending-loss mechanisms.

To achieve this main goal, the following specific objectives were established:

1. Develop and implement a low-cost optoelectronic acquisition system for optical excitation and intensity measurement in polymer-fiber-based pressure sensors.

2. Formulate an inverse-modeling framework based on the Moore–Penrose pseudoinverse for spatial localization and pressure reconstruction from discrete optical attenuation measurements.

3. Assemble and experimentally characterize the prototype pressure-sensing platform, establishing its operational range and the relationship between applied loads and optical responses.

4. Experimentally assess the system by quantifying localization accuracy, pressure-estimation performance, reconstruction quality, and sensitivity under controlled static loading conditions.

The scope of this work is limited to the study of a laboratory-scale fiber-optic pressure-sensing prototype evaluated under controlled static loading conditions. The system consists of a flexible elastomeric pad with a multipoint grid of embedded polymer optical fibers and low-cost optoelectronic acquisition circuits, which is assessed in terms of spatial localization and pressure-reconstruction performance. No long-term stability tests, dynamic loading scenarios, or operation under real-world conditions are addressed in this thesis; instead, the results are intended to demonstrate the feasibility and practical challenges associated with the proposed platform as a proof of concept.

Within this context, the material presented in this thesis brings together the theoretical background, experimental development, and quantitative evaluation of the proposed sensing platform. On this basis, the remainder of this document is organized as follows.

Chapter 1 presents a literature review covering the principles of flexible pressure sensing, the constraints of traditional electronic sensors, and the advantages and challenges of optical transduction mechanisms.

Chapter 2 reproduces the first journal article derived from this project, detailing the conceptual development, fabrication, and initial characterization of prototype sensing configurations.

Chapter 3 contains the second journal article, which develops the inverse-modeling framework, introduces a multipoint sensor pad, and presents experimental results for localization, pressure estimation, reconstruction accuracy, and performance metrics.

Chapter 4 discusses the research contributions, technological limitations, and future opportunities for advancing flexible optical pressure-sensing systems.

Finally, the Conclusion summarizes the principal findings and outlines the main contributions of this research.

CHAPTER 1

LITERATURE REVIEW

1.1 Flexible Pressure Sensors

Flexible pressure sensors have attracted significant attention due to their ability to conform to dynamic and irregular surfaces, which enables a broad range of applications in areas such as healthcare monitoring, human–machine interaction, electronic skin, soft robotics, and motion or performance tracking (Dulal et al., 2022; Jia et al., 2024; Li et al., 2020; Meng et al., 2022; Tan et al., 2022; Xu et al., 2024; D. Xu et al., 2025; Hao Zhang et al., 2024). Their capacity to detect physiological signals (e.g., respiration, pulse waves, plantar pressure) as well as external mechanical stimuli (e.g., grip force, gait patterns, or body posture) has supported their integration into wearable platforms, robotic systems, and tactile interfaces across multiple technological domains (Amouzou, 2025; Gao & Chen, 2023; Li et al., 2020; D. Wang, G. Ma, et al., 2025; Wei et al., 2025; Zeng et al., 2024), as illustrated in Figure 1.1.

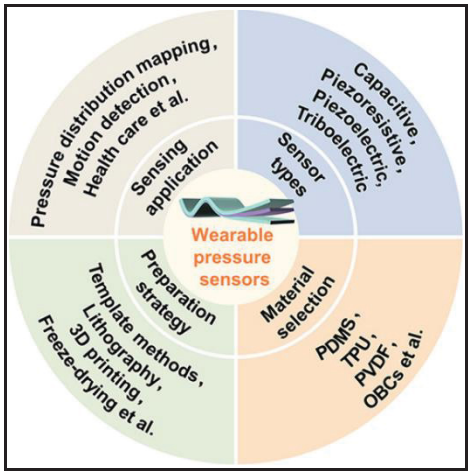

Figure 1.1 Conceptual overview of wearable pressure sensors, including sensor types, material selection, fabrication strategies, and representative application areas
Taken from K. Chang et al. (2025, p. 3)

The performance requirements commonly reported in the literature include high sensitivity for detecting subtle stimuli, a wide detection range, fast response, mechanical durability, low

power consumption, biocompatibility, and high spatial resolution (K. Chang et al., 2025; Y. Guo et al., 2024; D. Xu et al., 2025). However, experimental evidence indicates that flexible pressure sensors rarely fulfill all functional requirements simultaneously, which has driven ongoing research into more reliable and versatile transduction mechanisms (K. Chang et al., 2025; Y. Guo et al., 2024; Shiyi et al., 2025). This persistent imbalance among key performance metrics underscores the need to examine the physical principles behind existing sensing approaches, setting the stage for a more detailed discussion of existing transduction mechanisms.

While biomedical monitoring remains an important application area, flexible pressure sensors are equally relevant in robotics, prosthetics, sports performance assessment, and interactive or immersive systems, reflecting their broad technological versatility (Y. Guo et al., 2024; Heng et al., 2022; D. Wang, G. Ma, et al., 2025). This diversity of use cases, combined with the performance constraints outlined above, highlights the need to examine the different transduction mechanisms to understand the specific advantages and challenges associated with this kind of sensor.

1.1.1 Transduction Mechanisms in Flexible Pressure Sensors

Flexible pressure sensors are based on different physical principles to convert mechanical inputs into measurable electrical or optical outputs, enabling a wide range of device architectures and performance characteristics (Y. Guo et al., 2024; Homayounfar & Andrew, 2020). The most established approaches include piezoresistive, capacitive, piezoelectric, and triboelectric mechanisms, while more recent developments have introduced field-effect transistor (FET) based, electrochemical, magnetoelastic, and optical sensing strategies (Homayounfar & Andrew, 2020; Zhang et al., 2022; Zhao et al., 2023). Each mechanism relies on a fundamental transduction principle that determines the type of signal it generates, the materials and structural configurations it requires, and the performance limits it can achieve. The following paragraphs provide a concise overview of these mechanisms and outline their essential operating principles (Figure 1.2).

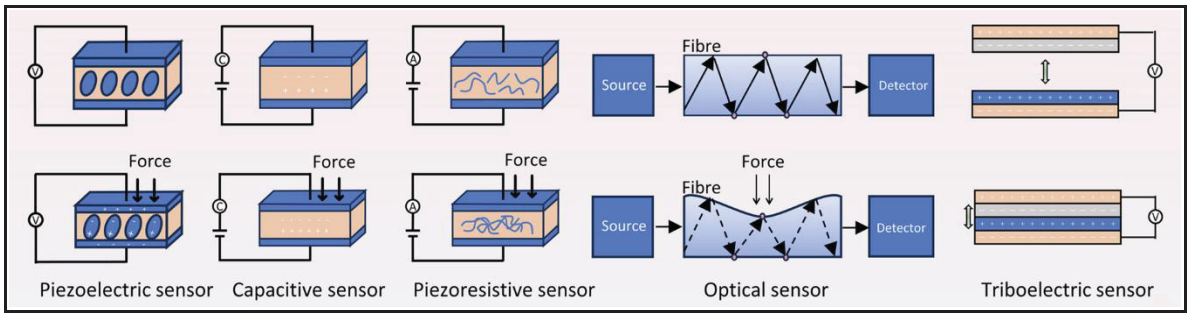

Figure 1.2 Overview of the main transduction mechanisms used in flexible pressure sensors, including piezoelectric, capacitive, piezoresistive, optical, and triboelectric approaches Adapted from Xue et al. (2024, p. 2)

One of the most widely used strategies is the piezoresistive approach, which translates mechanical deformation into electrical resistance changes through variations in geometry, intrinsic resistivity, contact resistance, and quantum tunneling effects within the sensing material (K. Chang et al., 2025; Chen & Yan, 2020; Homayounfar & Andrew, 2020; Meng et al., 2022; Yao et al., 2025). Under compression, conductive vias increase in number or area, resulting in a measurable decrease in resistance (Zhiwen Chen et al., 2025; Zhao et al., 2023). Reported sensitivities range several orders of magnitude, from ~1.2 kPa^{-1} to values above 1800 kPa^{-1} or even 2200 kPa^{-1}, operating from a few Pascals to hundreds of kPa or up to the MPa order (Y. Guo et al., 2024; Homayounfar & Andrew, 2020; Mao et al., 2024; Tan et al., 2022; Xu et al., 2024; L. Zhao et al., 2024). Architectures usually combine flexible substrates (e.g., Polydimethylsiloxane (PDMS), Polyurethane (PU), Polyethylene Terephthalat (PET), textiles) with conductive composites such as graphene, carbon nanotubes (CNTs), MXene, metal nanowires, or carbon black, often enhanced through microstructures such as pyramids, domes, porous matrices, or sequential patterns to amplify stress concentration and signal response (Gao et al., 2022; Li et al., 2020; X. Li et al., 2025; Shang et al., 2025; X. Wang et al., 2025; Hao Zhang et al., 2024; L. Zhao et al., 2024; Zhao et al., 2023; Zhao et al., 2022). Their straightforward fabrication has supported widespread use in electronic skin (e-skin), health monitoring, human–machine interfaces, and soft robotic applications (Zhiwen Chen et al., 2025; Y. Guo et al., 2024; Y. Huang et al., 2019; S. Zhang et al., 2024), with characteristic signal behavior determined by the physics of resistive transduction (Aptabusjaman et al., 2025;

Bi et al., 2023; Jia et al., 2024; Kim et al., 2024; Liu et al., 2020; Moka Vidyanag et al., 2025; Tang et al., 2024; Xu et al., 2024; S. Zhang et al., 2024; Zhi et al., 2025).

In contrast, capacitive sensing relies directly on changes in electric-field geometry, typically through variations in electrode separation, effective contact area, or the dielectric permittivity of a compressible insulating layer (Dong et al., 2024; Gu et al., 2019; D. Xu et al., 2025; Yu et al., 2022), (Figure 1.3). Their dielectric layer, often PDMS, Ecoflex, and PU, plays a major role in the sensor response, especially when designed with microstructures such as pores, wrinkles, air gaps, or pyramidal features to enhance compressibility and sensitivity (Dong et al., 2024; Yanru Li et al., 2024; Liu et al., 2025; Masihi et al., 2021; Meng et al., 2022). Reported sensitivities range from fractional values up to the order of thousands of kPa^{-1} (e.g., 0.22 kPa^{-1} (D. Xu et al., 2025), 217.5 kPa^{-1} (Dong et al., 2024), and 1613 kPa^{-1} (D. Wang, B. Li, et al., 2025)), while detection limits can extend from some Pascals to several hundred kPa or even the MPa level depending on structural design (H. Chen et al., 2025; Y. Guo et al., 2024; Yuxia Li et al., 2024).

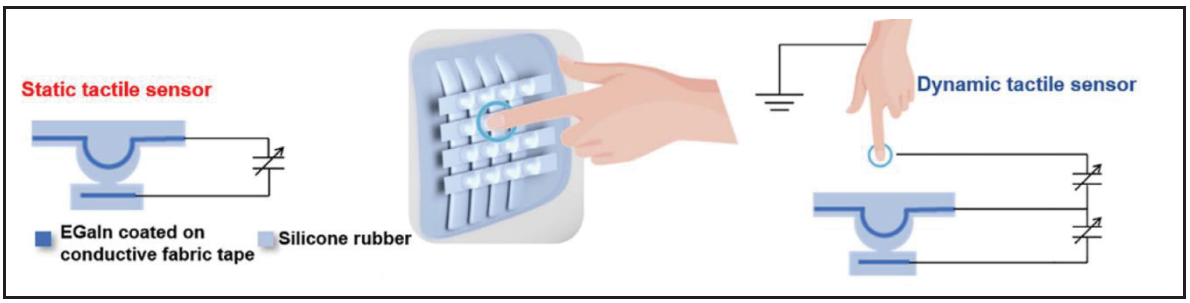

Figure 1.3 Schematic illustration of a capacitive-based tactile sensing architecture for static and dynamic pressure detection
Adapted from Xie et al. (2024, p. 17043)

Beyond the dielectric layer, electrode materials also play a key role in capacitive sensor performance. Flexible electrodes made of CNTs, graphene films, silver nanowires (AgNWs), conductive polymers, or liquid metals extend capacitive designs to stretchable and even transparent formats when required (Y. Guo et al., 2024; Yan Huang et al., 2019). These attributes explain their frequent use in e-skin systems, wearable patches, robotic interfaces, and

touch-sensing arrays (H. Chen et al., 2025; Dong et al., 2024; D. Wang, B. Li, et al., 2025; H.-C. Xu et al., 2025), where their dependence on electric-field interactions shapes characteristic signal behavior (Butt, Kazanskiy, et al., 2022; Dong et al., 2024; X. Guo et al., 2024; H. Lee et al., 2025; Tan et al., 2022; Wang et al., 2020; Xu et al., 2024; H.-C. Xu et al., 2025).

For piezoelectric mechanisms, dynamic applications are the main focus, since rapid changes in mechanical stress generate charge through dipole reorientation within piezoelectric materials (Homayounfar & Andrew, 2020; Yan Huang et al., 2019; Jeon et al., 2019; Meng et al., 2022; Xu et al., 2024; Yu et al., 2022; Zhang et al., 2022). This principle enables high sensitivity, fast response, and self-powered operation (Gu et al., 2019; Kim & Oh, 2020; D. Xu et al., 2025), with reported sensitivities around 15.08 mV/kPa (Zhen et al., 2024). However, because the generated charge dissipates over time, these devices cannot hold an output under static or slowly varying loads, which limits their use for continuous pressure readings (Meng et al., 2022; Xu et al., 2024). Common materials include piezopolymers such as polyvinylidene fluoride (PVDF) and its copolymer poly(vinylidene fluoride-co-trifluoroethylene) (P(VDF-TrFE)), along with ceramics like zinc oxide (ZnO), lead zirconate titanate (PZT), and barium titanate ($BaTiO_3$), frequently integrated as nanoparticles, nanowires, films, or electrospun fibers to achieve flexibility (Gu et al., 2019; Homayounfar & Andrew, 2020; Yan Huang et al., 2019; Li et al., 2020; Zhen et al., 2024). Many designs adopt a sandwich configuration with electrodes surrounding the piezoelectric layer, and electrospun nanofiber networks are often used when high responsiveness is needed (Gu et al., 2019; Yan Huang et al., 2019; Meng et al., 2022; Xu et al., 2024). Overall, their performance depends on the fast, transient nature of dipole-based charge generation (Heng et al., 2022; Yan Huang et al., 2019; Li et al., 2020; Meng et al., 2022; Xu et al., 2024; Zhen et al., 2024).

A different form of dynamic response appears in triboelectric sensors, which depend on contact electrification and electrostatic induction when two materials with distinct triboelectric polarities undergo repeated contact and separation (Bi et al., 2023; D. Xu et al., 2025; Yu et al., 2022). This mechanism naturally produces high voltage output, affordable architectures, and self-powered operation (Bi et al., 2023; Meng et al., 2022; D. Xu et al., 2025). Reported

data includes sensitivities of 0 - 2 kPa with response times of 16 ms (D. Xu et al., 2025), or 0 - 8.78 kPa with response times as fast as 6 ms and detection limits down to 0.8 Pa (Xie et al., 2024). Regular material pairs include PDMS, polytetrafluoroethylene (PTFE), polyimide (PI), or nylon combined with copper or aluminum, while microstructured surfaces are commonly added to increase the effective contact area and charge generation (Bi et al., 2023; Kim & Oh, 2020; Ruth et al., 2020). These devices are frequently used in wearable systems, motion detection, and energy harvesting (Bi et al., 2023; Meng et al., 2022; D. Xu et al., 2025; Yao et al., 2025), and their behavior is inherently tied to the cyclical contact–separation process and the relative motion between the triboelectric layers (Heng et al., 2022; Yao et al., 2025; Hongjian Zhang et al., 2024).

Pressure can also be detected inside the semiconductor structure itself, as in FET-based sensors, where mechanical loading modifies the gate dielectric or interfacial properties, altering the carrier density within a semiconductor channel (Butt, Kazanskiy, et al., 2022; Chen & Yan, 2020; Homayounfar & Andrew, 2020; Kim & Oh, 2020; Xu et al., 2024; Zhao et al., 2023). Because the transistor amplifies these variations, these devices achieve extremely high sensitivities (Li et al., 2020), with reported values reaching 8.4 kPa^{-1} (Schwartz et al., 2013) and 514 kPa^{-1} (Kim & Oh, 2020), and response times below 10 ms (Schwartz et al., 2013), while keeping low power consumption. Organic FETs (OFETs) combining structured elastomeric dielectrics with flexible semiconductor layers are common when mechanical adaptability with high responsiveness is required (Gu et al., 2019; Li et al., 2020; Schwartz et al., 2013). This architecture supports applications in high-resolution tactile interfaces, physiological monitoring (e.g., pulse-wave sensing), and large-area e-skin systems that benefit from amplified electrical signals (Heng et al., 2022; Homayounfar & Andrew, 2020; Xu et al., 2024). Their operation is closely tied to transistor physics, which defines both their advantages and the practical considerations involved in integrating these devices (Butt, Kazanskiy, et al., 2022; Chen & Yan, 2020; Zhao et al., 2023).

Optical sensing offers a completely different route by embedding optical fibers or waveguides within deformable matrices such as PDMS, allowing pressure-dependent changes in light

intensity, wavelength, or phase (Heng et al., 2022; Li et al., 2020; Tan et al., 2022). Bending or compressing the fiber induces losses (e.g., bend attenuation) or spectral shifts that enable the measurement of small and large loads depending on the fiber design (Li et al., 2020). Because light propagation is unaffected by electromagnetic interference (EMI), optical sensors provide high resolution and signal integrity even in harsh electromagnetic environments (Li et al., 2020; Wang et al., 2008; Wang et al., 2005), including Magnetic Resonance Imaging (MRI) systems, where electrical sensors typically fail (Leal-Junior et al., 2019; Wang et al., 2008).

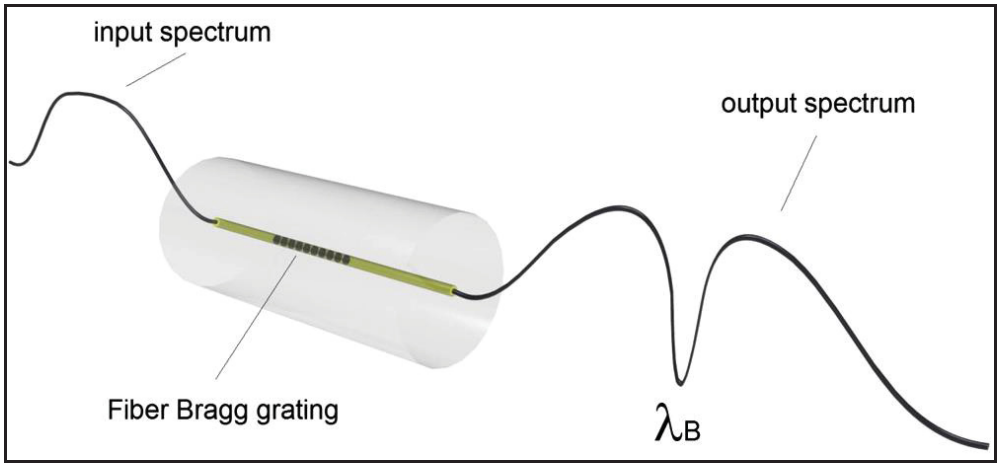

Figure 1.4 Schematic illustration of a Fiber Bragg Grating-based optical sensing principle, showing the characteristic Bragg wavelength (λ_B) in the transmitted spectrum
Taken from Roriz et al. (2013, p. 3)

Widespread implementation uses plastic or glass optical fibers, including Fiber Bragg Gratings (FBGs), embedded within soft substrates to maintain flexibility while preserving optical performance (Bai et al., 2020; Gan et al., 2024; Kanellos et al., 2010; Leber et al., 2019). These capabilities have supported applications in biomedical monitoring, biomechanical assessment, robotics, and industrial systems requiring stable, low-noise measurements (Kanellos et al., 2010; Roriz et al., 2013; Sabri et al., 2015; Wang et al., 2008), with their overall performance determined by the coupling, alignment, and mechanical interaction between the optical components and the surrounding material (Li et al., 2020; Yao et al., 2025).

Some pressure-sensing strategies emerge from ionic transport, as in electrochemical designs that interpret pressure-induced variations in ion migration, redox activity, or interfacial charge transfer at an electrode-electrolyte boundary (Huang et al., 2024; Yang et al., 2024). This mode enables electrical signals generated directly by ionic movement, allowing electrochemical sensors to operate in self-powered mode for both static and dynamic pressures detection (Huang et al., 2024). Material platforms usually combine soft ionic conductors or gel electrolytes coupled with flexible electrodes, facilitating intimate contact with deformable substrates in wearable or conformal sensing environments (Huang et al., 2024). Their overall response depends strongly on the stability of the electrolyte-electrode interface and the mechanical behavior of the ionic medium, which together shape the resulting signal characteristics in this form of transduction (Hongjian Zhang et al., 2024).

Magnetoelastic sensors work by embedding magnetic particles within soft matrices; deformation redistributes magnetic domains and alters the local magnetic field, enabling pressure readout through changes in magnetic flux (Heng et al., 2022; Meng et al., 2022). Because the signal depends on magnetic rather than electrical coupling, these sensors remain functional in wet environments and can even operate underwater without encapsulation (Meng et al., 2022). Their use has grown in applications requiring environmental robustness, while their response depends on the stability of the magnetic domains and the surrounding magnetic environment that affect field variation (Meng et al., 2022; Yao et al., 2025).

Viewed together, these mechanisms show how different physical principles lead each sensing approach to stand out in specific operating conditions. Capacitive and FET-based strategies are well suited for detecting subtle low-pressure variations because of their high responsiveness and, in the case of FETs, intrinsic amplification (Gao & Chen, 2023; Gu et al., 2019; Schwartz et al., 2013). Piezoresistive designs continue to be widely used for large-area tactile mapping where simple structures facilitate scalable fabrication (Dong et al., 2024; Y. Guo et al., 2024; Z. Huang et al., 2025). Optical and magnetoelastic mechanisms broaden the design space by enabling reliable measurements in electromagnetic or wet environments where electrical readings are challenging (de Carvalho et al., 2025; Meng et al., 2022; Min et al., 2022; Sabri

et al., 2015; Wang et al., 2008; Zimmermann et al., 2024). Meanwhile, piezoelectric and triboelectric devices provide fast responses to dynamic events, and electrochemical systems offer a route to self-powered static sensing (Heng et al., 2022; Huang et al., 2024; Meng et al., 2022; Hongjian Zhang et al., 2024). Taken together, these behaviors highlight that each mechanism works best under certain conditions, and that no single approach can satisfy all requirements. The same physical principles that make them effective also define their inherent challenges.

1.1.2 Challenges Associated with Flexible Pressure Sensors

Flexible pressure sensors exhibit several widespread challenges that arise from the mechanical and viscoelastic nature of the soft polymeric materials typically used in their fabrication. Phenomena such as hysteresis, creep, and mechanical fatigue contribute to signal offset, reduced repeatability, and progressively increasing measurement errors across repeated loading cycles (K. Chang et al., 2025; Duan et al., 2020; Gao et al., 2022; G. Huang et al., 2025; Yan Huang et al., 2019; Kim et al., 2024; H. Lee et al., 2025; Li et al., 2020; Yanru Li et al., 2024; Liu et al., 2025; Majumder et al., 2025; Tan et al., 2022; Tchantchane et al., 2025; R. Wang et al., 2025; Yang et al., 2022). Although these platforms are recognized for their ability to adapt to curved or soft surfaces, maintaining long-term functional stability remains challenging, as repeated deformation can lead to microstructural collapse, irreversible changes in conductive pathways, and progressive degradation in electrical performance (K. Chang et al., 2025; Cui et al., 2025; Duan et al., 2020; Tang et al., 2024; D. Wang, G. Ma, et al., 2025; Xu et al., 2024). Even elastomers widely used for their mechanical compliance, such as PDMS, may present practical issues related to breathability and moisture accumulation during prolonged contact, which can jeopardize comfort and stability in extended-use scenarios (K. Chang et al., 2025; T.-S. Chang et al., 2025; Y. Guo et al., 2024; Li et al., 2020; Shang et al., 2025; Tan et al., 2022).

Environmental susceptibility also compromises the reliability of flexible sensor technologies. Temperature fluctuations, humidity, and EMI can produce nonlinearities, baseline offset, or

changes in the intrinsic electrical properties of the sensing materials (Al-Mai et al., 2017; Butt, Kazanskiy, et al., 2022; Chad Webb et al., 2016; Chang et al., 2012; Y. Guo et al., 2024; Tian et al., 2024; Wang et al., 2008; Wang et al., 2005; Xu et al., 2024; Yang et al., 2025; Yao et al., 2025). Common architectures such as capacitive and resistive sensors may suffer from parasitic capacitance or this EMI sensitivity, while large-area arrays frequently experience both mechanical and electrical crosstalk that decreases spatial resolution and complicates accurate pressure-map reconstruction (Al-Mai et al., 2017; Chang et al., 2012; Y. Guo et al., 2024; H. Lee et al., 2025; H. Li et al., 2025; Luo et al., 2025; Tian et al., 2024; S. Y. Wang et al., 2025; Wang et al., 2008; Wang et al., 2005; Xu et al., 2024; Yang et al., 2025). Although encapsulation strategies and environmental compensation schemes can mitigate some of these effects, the underlying instability associated with soft materials and electrically active composites remains a persistent issue that often requires additional processing to correct or compensate.

Inherent performance constraints further limit the applicability of flexible sensing mechanisms. Designs optimized for high sensitivity frequently exhibit narrow detection ranges or saturate under moderate pressures, whereas sensors engineered for broader operating ranges tend to lose resolution for subtle pressure variations (Duan et al., 2020; J. Huang et al., 2025; Jia et al., 2024; Kim et al., 2024; Mao et al., 2024; Souri et al., 2020; Tang et al., 2024; S. Y. Wang et al., 2025; Wu, 2019; D. Xu et al., 2025; Yao et al., 2025). Furthermore, piezoelectric and triboelectric devices are inherently incapable of measuring static forces due to charge leakage, limiting their usability in continuous or steady-state monitoring tasks (Belk et al., 2025; K. Chang et al., 2025; Yan Huang et al., 2019; Huang et al., 2024; Z. Huang et al., 2025; Li et al., 2020; Meng et al., 2022; Xu et al., 2024; Yao et al., 2025; Hongjian Zhang et al., 2024). Compounding these intrinsic limitations, additional constraints arise during fabrication and system integration; many high-performance sensors rely on complex, low-throughput manufacturing processes, exhibit significant device-to-device variability, or require external signal-acquisition electronics that increase system stiffness, power consumption, and wiring complexity (Chang et al., 2012; Chen & Yan, 2020; Duan et al., 2020; Hua et al., 2024; L. Li et al., 2024; Yanru Li et al., 2024; Majumder et al., 2025; D. Xu et al., 2025; S. Zhang et al.,

2024). Collectively, these challenges underscore the difficulty of achieving a flexible pressure sensor that simultaneously provides high sensitivity, broad linearity, mechanical robustness, long-term stability, and straightforward integration into practical systems.

Beyond environmental sources, the nonlinear relationship between applied pressure and electrical output remains one of the most prevalent issues, as many sensing mechanisms exhibit segmented linearity, early saturation, or compressibility-dependent responses that limit the applicability of straightforward analytical models (Gao et al., 2022; Masihi et al., 2021; Shu et al., 2024; Tan et al., 2022; Tang et al., 2024; Wang et al., 2008; Wang et al., 2005; Xu et al., 2024; D. Xu et al., 2025). In practice, these behaviors often require both multiregime calibration strategies initially and periodic recalibration over time to adequately capture the full operating range of the device. This burden often intensifies when sensitivity shifts between low- and high-pressure regimes or when time-dependent offset originates from viscoelastic relaxation, temperature fluctuations, or incomplete structural recovery (Duan et al., 2020; Gao et al., 2022; Kisannagar et al., 2025; Souri et al., 2020; Xu et al., 2024; Yao et al., 2025; Yassin et al., 2024). Noise coming from environmental factors, motion-induced signal fluctuations, or fabrication inconsistencies further complicates signal interpretation and often requires advanced filtering or algorithmic compensation to extract meaningful measurements (Bi et al., 2023; Egger et al., 2025; Hua et al., 2024; Yan Huang et al., 2019; Lu et al., 2025; Majumder et al., 2025; Souri et al., 2020; Tian et al., 2024; H.-C. Xu et al., 2025; Yang et al., 2025; Yao et al., 2025). As a result, establishing stable, repeatable, and interpretable mappings between pressure input and sensor output remains a consistent obstacle across flexible sensor systems.

At the system level, flexible sensors often require external electronics for operation, which as mentioned earlier, adds stiffness, increases power consumption, and restricts miniaturization (Butt, Kazanskiy, et al., 2022; Liu et al., 2025; Min et al., 2021; Schwartz et al., 2013). Optical platforms also demand their own optical acquisition hardware, which can introduce additional bulk depending on the sensing configuration (Ghaffar et al., 2024; Yassin et al., 2024). Large sensor arrays introduce further complexity through dense wiring and multiplexing requirements, as well as the previously mentioned crosstalk that lowers spatial resolution (Li

et al., 2020; K. Ma et al., 2025; Moeinnia et al., 2024), with both mechanical deformation transfer and electrical interference (Y. Guo et al., 2024; H. Lee et al., 2025; H. Li et al., 2025). These issues are often intensified in architectures that embed isolated sensing units or microstructured trenches (H. Li et al., 2025; D. Xu et al., 2025; Yang et al., 2025), while high-density arrangements remain vulnerable to electrical coupling between adjacent channels (Chen & Yan, 2020; H. Lee et al., 2025; Luo et al., 2025; Moka Vidyanag et al., 2025; S. Y. Wang et al., 2025). High-resolution systems may require thin-film transistor backplanes or finely patterned electrodes, which compounds the fabrication challenges and reduces scalability (Belk et al., 2025; Bi et al., 2023; Chen & Yan, 2020; Wang et al., 2024; Zhao et al., 2022; Zhen et al., 2024). Consequently, improving spatial resolution typically compromises system flexibility, manufacturability, and long-term reliability, reinforcing the need for advanced modeling, integration strategies, and compensation techniques to achieve robust performance in practical applications.

Beyond these shared issues, several works have shown that inherent limits of electrically based flexible sensors (e.g., dense wiring, contact degradation, and electrical isolation) have motivated the exploration of optical and optoelectronic sensing strategies (Leal-Junior et al., 2019; K.-P. Lee et al., 2025; Ngiejungbwen et al., 2024; Wang et al., 2005). Because these approaches rely on different physical principles, responding differently to problems like electromagnetic interference, corrosion, or extensive conductive networks, they have increasingly been investigated as alternatives capable of reducing some of the constraints observed in conventional electronic systems, despite introducing their own design considerations (Roriz et al., 2013; Sabri et al., 2015; Zhao et al., 2016; Zimmermann et al., 2024). This interest has driven the development of the optical approaches outlined in the next section.

1.2 Optical Pressure Sensors

Optical pressure sensors include a broad range of mechanisms that convert mechanical deformation into measurable changes in light transmission. Although these systems vary in

materials, optical behavior, and signal-acquisition approaches, they share the basic premise that external forces modify the transmitted optical power in a predictable way. This section introduces the operating principles most directly connected to flexible sensing platforms and outlines the advantages, limitations, and application areas that motivate the architecture developed in the present work.

1.2.1 Working Principles of Optical Pressure Sensors

Optical pressure sensors work by converting mechanical deformation into measurable changes in light transmission along an optical fiber or waveguide. Several optical transduction families have been reported in the literature, including wavelength-shift mechanisms using Fiber Bragg Gratings (FBGs) and cavity-based interferometric approaches, both capable of high sensitivity but requiring complex, expensive, and often rigid optical acquisition systems (Roriz et al., 2013; Sabri et al., 2015; Yassin et al., 2024). In contrast, this work focuses mainly on intensity-modulated sensors based on bending-induced optical loss, owing to their straightforward implementation, low cost, and compatibility with flexible polymer substrates and large-area pressure-mapping architectures (Chang et al., 2012; Soetanto et al., 2011).

In intensity-based bending-loss sensors, the applied pressure modifies the propagation conditions of light within a polymer optical fiber or polymer waveguide. When a fiber is deformed, the optical beams traveling along the curved region may reach the core–cladding interface at angles below the critical angle, causing partial failure of total internal reflection (TIR) and resulting in measurable attenuation of the transmitted optical power. This effect arises from the refractive-index contrast between the fiber core (n_1) and cladding (n_2), which allows light to escape when bending alters the propagation conditions (Gan et al., 2024; He et al., 2023; Wang et al., 2008), as shown in Figure 1.5. Several physical mechanisms contribute to this attenuation, including macrobending loss, evanescent-field interaction with the surrounding medium, and cladding-mode perturbation in twisted or uncoated fibers (Gan et al., 2024; Ghaffar et al., 2024; He et al., 2023).

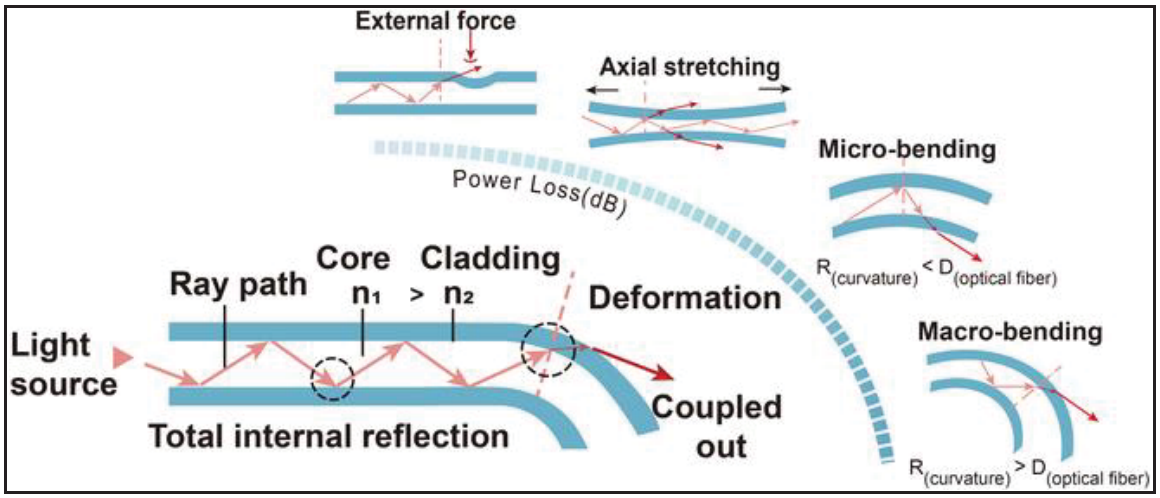

Figure 1.5 Schematic illustration of bending-loss mechanisms in optical fibers
Taken from Gan et al. (2024, p. 12)

Bending-loss mechanisms are particularly effective in polymer fibers, which exhibit high flexibility, large elastic strain limits (up to ~10% for Poly(methyl methacrylate) (PMMA)), and lower Young's modulus compared to silica fibers (Leal-Junior et al., 2019; Min et al., 2022). These mechanical properties enable strong, repeatable curvature-induced attenuation under relatively small applied forces, making polymer fibers suitable for wearable and surface-adaptive systems.

For pressure sensing, polymer fibers are typically embedded within soft, elastomeric substrates such as polydimethylsiloxane (PDMS). When an external load is applied to the surface, the substrate deforms and bends the fiber at the point of contact, producing a proportional decrease in optical intensity detected at the output. This simple transduction mechanism supports both normal-force measurement, through vertical displacement of the fiber, and shear-force measurement, where lateral displacement between stacked or intersecting fiber layers produces different bending patterns (Chang et al., 2012; Soetanto et al., 2011; Wang et al., 2005), as shown in Figure 1.6.

When arranged in orthogonal layers, intersecting fibers form discrete pressure-sensing nodes capable of producing a two-dimensional pressure map. Each applied force bends the

corresponding row and column fibers, allowing localization of the stimulus from the pattern of optical losses (Chang et al., 2012; Wang et al., 2005). This architecture supports distributed measurement across curved or flexible surfaces without requiring rigid transducers or complex interrogation electronics. Building on these fundamental operating principles, the following section examines the broader advantages and practical challenges that characterize optical pressure sensing platforms, particularly in comparison to the electrically based systems described previously.

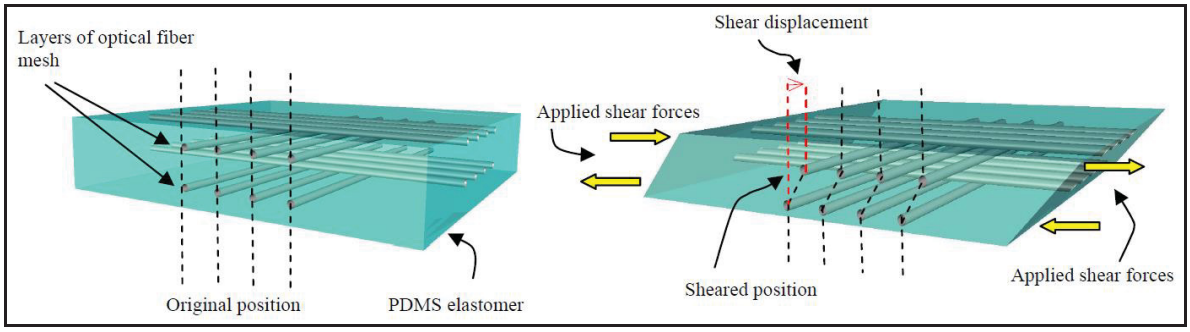

Figure 1.6 Schematic illustration of a crossed-layer polymer optical fiber architecture embedded in a PDMS elastomer for two-dimensional pressure sensing
Taken from Chao-Shih et al. (2007, p. 3)

1.2.2 Advantages and Challenges of Optical Pressure Sensors

The principles described in the previous section demonstrate the operational feasibility of bending-loss sensing; however, the adoption of polymer-fiber architectures introduces its own set of material, calibration, and integration constraints. The following subsections examine the intrinsic advantages that make optical approaches attractive for flexible sensing applications, followed by an analysis of the challenges that currently constrain their implementation.

1.2.2.1 Advantages of Optical Pressure Sensors

Optical pressure sensors offer several intrinsic advantages that directly address many of the environmental and integration challenges observed in electrically based flexible sensors. Because optical fibers are dielectric, they are inherently immune to electromagnetic and radio-

frequency interference (EMI/RFI), making them compatible with environments where electronic sensors become unreliable, including MRI scanners and high-voltage systems (de Carvalho et al., 2025; Ghaffar et al., 2024; K.-P. Lee et al., 2025; Ngiejungbwen et al., 2024; Peters, 2010; Sabri et al., 2015; Yassin et al., 2024). This immunity extends to harsh environmental conditions more broadly; their resistance to corrosion and chemical exposure enables implementation in chemically aggressive or outdoor environments where conventional sensors would rapidly degrade (Butt, Voronkov, et al., 2022; Min et al., 2021; Yassin et al., 2024). Additionally, because polymer optical fibers are dielectric, they do not conduct electricity, eliminating the risk of electric shock, which is an advantage particularly valuable in medical and hazardous settings (Ngiejungbwen et al., 2024; Sabri et al., 2015).

Beyond environmental robustness, optical fibers provide remarkable mechanical properties that facilitate integration into flexible systems. These materials exhibit high flexibility, smaller bend radii, and greater fracture toughness than their silica counterparts (Leal-Junior et al., 2019; Leitão et al., 2022; Min et al., 2021; Peters, 2010). Their low Young's modulus enhances mechanical sensitivity, and their ability to withstand elastic strains of up to 10% in PMMA and even 300% in thermoplastic elastomer waveguides, supporting large deformations without structural failure (Leber et al., 2019; Peters, 2010). The compact and lightweight nature of optical fibers further enables smooth integration into textiles, composites, or flexible substrates with minimal impact on mechanical behavior (Bahin et al., 2023; Leal-Junior et al., 2019; Min et al., 2021; Ngiejungbwen et al., 2024). Many polymer formulations are also biocompatible, making polymer fiber-based sensors suitable for wearable systems and safe for direct skin contact (Gan et al., 2024; Min et al., 2021; Ngiejungbwen et al., 2024).

From a measurement performance perspective, intensity-based and bending-loss sensors can achieve high sensitivity to curvature and pressure due to the strong dependence of optical transmission on fiber deformation (Bahin et al., 2023; Gan et al., 2024; Peters, 2010). The mechanical properties of polymers enhance this effect, enabling detection of subtle mechanical stimuli, while the wide strain capacity of the fibers supports a broad dynamic range, allowing the measurement of both small and large deformations (Leal-Junior et al., 2019; Ngiejungbwen

et al., 2024; Peters, 2010). Optical fibers also support multiplexing capabilities, enabling distributed sensing along a single waveguide, for example through wavelength-division schemes in grating-based systems, which is particularly advantageous for high-density sensor arrays and large-area monitoring (Kanellos et al., 2010; Leal-Junior et al., 2019; Min et al., 2021; Shabalov et al., 2024).

Finally, from a practical standpoint, although some high-end acquisition units (e.g., for FBGs) are costly, intensity-modulated bending-loss polymer-based sensors often use inexpensive components such as light-emitting diodes (LEDs) and photodiodes (Leal-Junior et al., 2019; Ngiejungbwen et al., 2024). Their fabrication can leverage scalable techniques such as molding, 3D printing, or melt-flow coextrusion, enabling low-cost prototyping and potential mass production (Leal-Junior et al., 2019; Leber et al., 2019; H. Ma et al., 2025; Ngiejungbwen et al., 2024).

1.2.2.2 Challenges of Optical Pressure Sensors

Despite these advantages, polymer fiber-based optical sensors face several challenges that directly affect bending-loss architectures. Material and performance limitations remain significant; polymer fibers exhibit higher intrinsic attenuation than silica, restricting usable lengths in some configurations and reducing signal-to-noise ratio in extended architectures (Bai et al., 2020; Leal-Junior et al., 2019; Min et al., 2021; Ngiejungbwen et al., 2024). More critically, their viscoelastic nature introduces hysteresis, creep, and nonlinear behavior, issues analogous to those observed in electrically based flexible sensors, particularly under sustained or dynamic loading, often needing compensation algorithms for stable measurements (Leal-Junior et al., 2019; Li et al., 2020).

Calibration and signal interpretation constitute another critical challenge for polymer-fiber optical sensors. Because bending-loss architectures respond to even small unintended deformations, cross-sensitivity, especially between strain, temperature, and incidental bending, can deform pressure readings and increase the complexity of calibration procedures (Gan et

al., 2024; Xue et al., 2024; Yassin et al., 2024). Beyond these cross-sensitivity effects, long-term stability remains a concern as well; polymer degradation, delamination, and fatigue can affect performance over extended operational periods, while silica fibers, although more stable chemically, remain fragile under bending or impact (K. Chang et al., 2025; Leal-Junior et al., 2019; K.-P. Lee et al., 2025; Min et al., 2022; S. Y. Wang et al., 2025; D. Xu et al., 2025).

Integration and system-level complexity introduce further practical constraints for optical pressure sensing platforms. Although polymer fibers simplify certain aspects of fabrication, connectorization remains challenging due to their small core size, soft mechanical behavior, and sensitivity to imperfect cuts or alignment procedures (Peters, 2010). Moreover, when scaling to large arrays, routing multiple fibers or cables through flexible structures adds mechanical complexity and can compromise durability under repeated deformations, particularly in wearable or robotic applications (Capp et al., 2025; Chen et al., 2023; Shabalov et al., 2024; Wang et al., 2008).

Finally, spatial resolution in bending-loss pressure-mapping systems is fundamentally constrained by the physical dimensions and routing of the fibers. Because the sensing node size is determined by fiber diameter, layer spacing, and minimum achievable crossing distance, these architectures cannot be easily miniaturized, and reported resolutions typically range from a few millimeters to approximately one square centimeter per point (Katrenova et al., 2022; Wang et al., 2008). In addition, crosstalk between adjacent nodes further limits resolution, as localized deformation can disturb multiple fibers simultaneously. Distinguishing between different mechanical modes (e.g., normal vs. shear, bending vs. stretching) often requires complex calibration procedures or multi-layer architectures (Bai et al., 2020; Gan et al., 2024).

Despite these limitations, optical bending loss sensors have been successfully implemented in several areas, as described in the following section.

1.2.3 Examples of Applications of Optical Pressure Sensors

Optical pressure sensors based on bending-loss and intensity modulation have been implemented across multiple application domains that require flexible structures capable of adapting to irregular surfaces and supporting distributed measurement. These demonstrations highlight the suitability of polymer fibers and elastomeric encapsulation for pressure sensing on deformable substrates, illustrating principles that directly relate to the architecture explored in this work. The following subsections summarize illustrative examples, organized by domain to contextualize their operating requirements and technical constraints.

1.2.3.1 Healthcare and Clinical Monitoring

One of the most established uses of bending-loss optical sensors is the measurement of plantar pressure during gait. Flexible insoles and mats embedding fibers in elastomeric substrates, typically PDMS, have been used to generate two-dimensional pressure maps under the foot (Chang et al., 2012; Wang et al., 2008). In these architectures, external loads bend the embedded fibers and attenuate the transmitted light, enabling the quantification of foot mechanics and the assessment of ulceration risk in diabetic patients as reported in previous research (Chang et al., 2012; Chao-Shih et al., 2007; Ngiejungbwen et al., 2024) (Figure 1.7).

Early implementations used two perpendicular fiber layers embedded in PDMS to measure both normal and shear stresses inside a shoe (Chao-Shih et al., 2007). Subsequent approaches explored instrumented insoles with multiple intensity-variation sensors fabricated through 3D printing (Ngiejungbwen et al., 2024) and large-area “smart carpets” integrating up to eighty polymer optical fibers for gait monitoring over extended surfaces (González-Cely et al., 2024). Further developments include microfabricated PDMS waveguide grids (4×4) for higher-resolution plantar mapping (Wang et al., 2008) and compact 2×2 elastomer-embedded arrays capable of discriminating normal and shear forces (Wang et al., 2005). Collectively, these systems demonstrate the scalability and architectural flexibility of bending-loss sensing architectures.

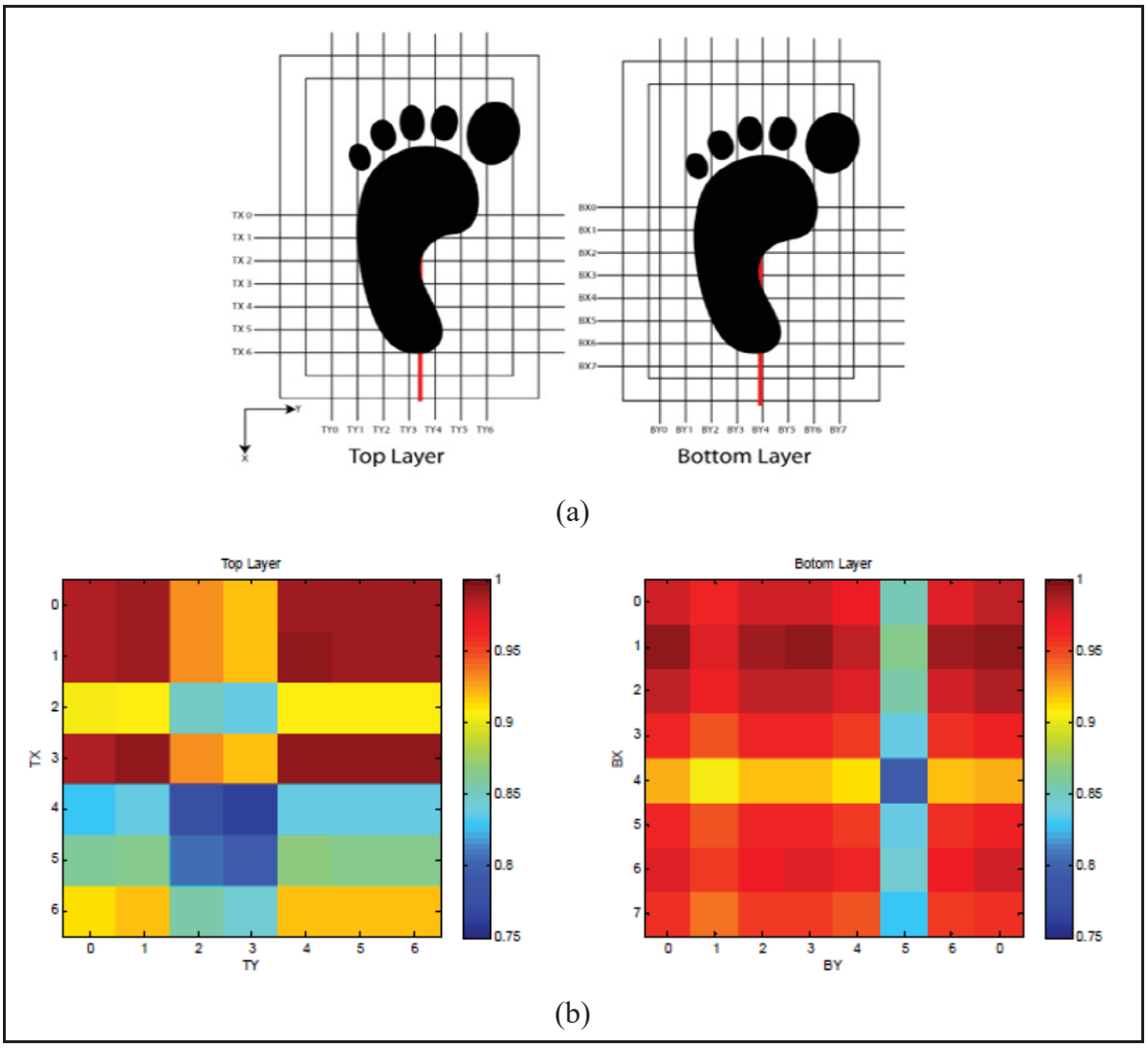

Figure 1.7 Example of a polymer optical fiber–based plantar pressure sensing platform. (a) Schematic representation of crossed fiber layers used to localize pressure through row–column intersections. (b) Corresponding pressure maps obtained from the top and bottom fiber layers under prosthetic foot loading
Adapted from Chang et al. (2012, p. 6,8)

Extending the use of distributed pressure mapping, optical systems have also been investigated for preventing pressure ulcers in individuals who remain seated or bedridden for prolonged periods. Reported approaches range from multiplexed FBG arrays embedded in flexible polymer mats (Roriz et al., 2013) to polymer-fiber designs encapsulated in soft transparent bags placed over wheelchair cushions or therapy beds (González-Cely et al., 2024). Although based on different transduction mechanisms, these systems share the goal of providing

continuous spatial pressure information to identify high-load regions and support timely weight-redistribution strategies.

1.2.3.2 Wearable and Body-Integrated Monitoring

In addition to clinical contexts, polymer fibers have also been incorporated into wearable systems for continuous monitoring. Embedded into garments, belts, or mattress layers, these fibers enable respiration and posture tracking through macrobending-induced intensity changes (Min et al., 2021; Ngiejungbwen et al., 2024). Thoracic expansion or body movement bends the fiber and modulates the transmitted light (Peters, 2010). Their mechanical ability to follow textile deformation and integrate naturally into soft structures makes polymer fibers suitable for body-integrated sensing, including environments where electronic sensors are impractical or contraindicated, such as MRI suites, benefiting from the EMI immunity discussed earlier (Figure 1.8).

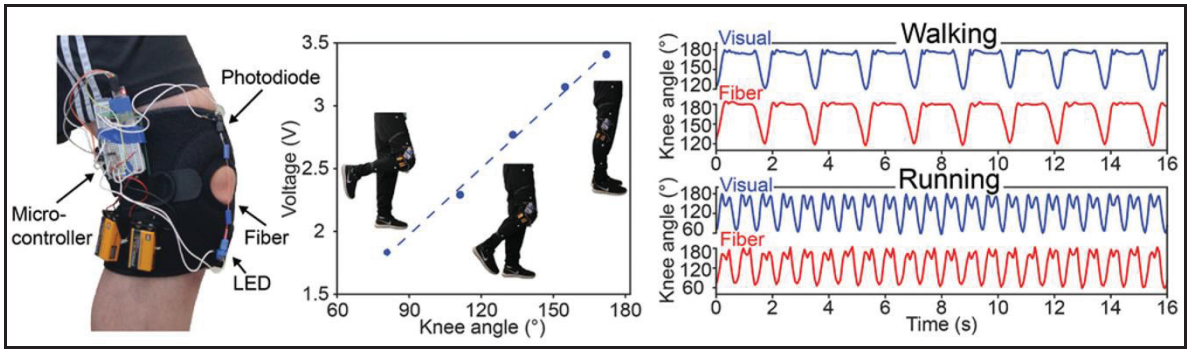

Figure 1.8 Example of a body-integrated optical fiber sensor embedded in a knee brace. Joint motion is captured through bending-loss-induced intensity modulation, illustrating the use of flexible optical fibers for wearable motion sensing
Adapted from Leber et al. (2019, p. 6)

Extending this wearable paradigm to kinematic tracking, bending-based optical curvature sensors have been integrated into devices such as knee braces, gloves, and textile-embedded motion-capture systems. In these configurations, fiber bending at the joints produces proportional optical attenuation, enabling quantitative tracking of limb movements (Leal-Junior et al., 2019; Min et al., 2022). Stretchable thermoplastic optical waveguides further

expand this functionality by supporting large reversible deformations in soft wearable structures (Leber et al., 2019). Although these systems target deformation rather than pressure, they underscore the versatility of bending-loss mechanisms for flexible sensing platforms.

1.2.3.3 Soft Robotics and Tactile Feedback

The mechanical flexibility and distributed sensing capabilities that benefit wearable systems are equally relevant in soft robotics, where grippers and prosthetic hands often rely on bending-loss and optical-coupling sensors to provide tactile feedback. One example explored in previous work embeds crossing polymer waveguides in PDMS foils, where applied forces modulate optical coupling at each intersection to generate distributed contact-pressure maps (Jeroen et al., 2010). Other implementations integrate stretchable optical waveguides into soft robotic fingers (Figure 1.9) to sense curvature, elongation, and external contact (Gan et al., 2024; Zhao et al., 2016). Together, these systems show that bending-loss mechanisms can be effectively incorporated into deformable robotic structures without restricting their motion, while still enabling multimodal tactile sensing.

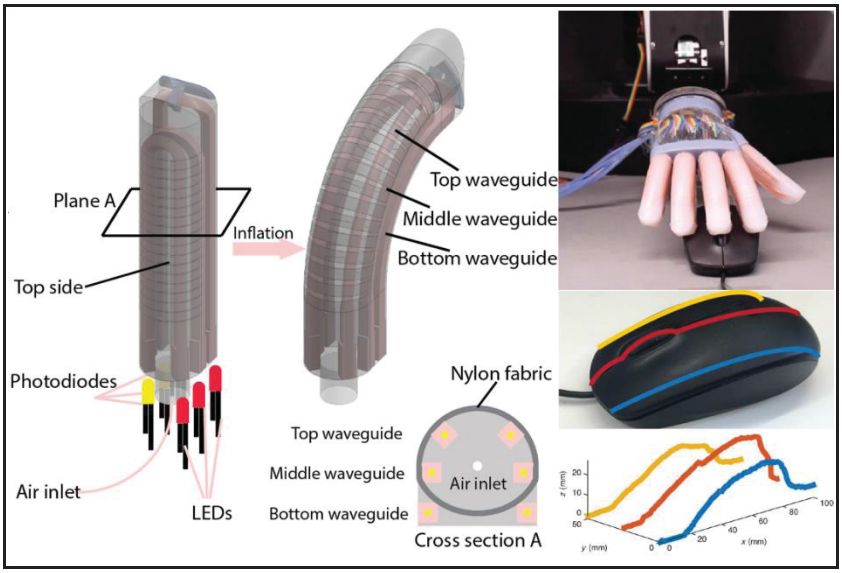

Figure 1.9 Example of a soft robotic finger instrumented with embedded polymer optical waveguides for bending-loss-based deformation and contact sensing, enabling curvature and touch detection through intensity modulation
Adapted from Zhao et al. (2016, p. 2, 6)

1.2.3.4 Industrial and Environmental Sensing

Finally, moving beyond body-worn or robotic contexts, bending-loss sensing has also been explored in large-area weight-sensing mats for industrial and outdoor environments. In these devices, a polymer fiber embedded in a soft foam base is periodically deformed by an array of "impactors" under applied load, generating measurable attenuation proportional to the distributed weight (Funnell & Thomas, 2023). This architecture is well-suited for uneven or outdoor surfaces where rigid scales are impractical, illustrating that macrobending-based optical platforms can be adapted to non-human environments and extended to large-area load monitoring without fundamental modifications to the sensing principle.

Taken together, these application areas show that bending-loss and intensity-modulated optical sensors have been implemented successfully in a wide range of settings, from body-integrated systems to soft robotics and large-area weight-sensing platforms. Despite their differences, these examples rely on the same fundamental elements: mechanically adaptive polymer fibers, elastomeric embedding, and optical attenuation under deformation, highlighting the versatility of this transduction approach. At the same time, the variability in architectures, calibration strategies, and sensing layouts illustrates that many aspects of distributed optical pressure mapping remain open design choices rather than established conventions. These demonstrations outline the evolving landscape of optical pressure sensing and help define the technical space in which the present work is positioned.

1.3 Conclusion

The literature reviewed above shows that optical pressure-sensing systems, particularly those based on bending-loss mechanisms and flexible polymer architectures, offer clear advantages for distributed measurement over curved or mechanically dynamic surfaces. Across clinical, wearable, robotic, and industrial domains, a common design logic becomes evident: leveraging mechanical flexibility to follow surface shape, embedding fibers within soft substrates to translate external loads into optical attenuation, and arranging fiber layouts in scalable patterns

to obtain spatially resolved sensing. Taken together, these developments indicate a technological trajectory centered on low-cost sensing strategies integrating mechanical flexibility with geometric adaptability.

Within this context, the present work contributes to advancing ongoing efforts by developing and experimentally validating a polymer-fiber pressure-sensing array coupled with an inverse-modeling framework for stimulus localization, pressure estimation, and spatial map reconstruction. This contribution does not claim to solve the broader challenges identified in the literature; instead, it offers a concrete and practical step toward more accessible and scalable optical pressure-mapping systems. By combining flexible materials, simplified optical acquisition, and algorithmic reconstruction, this work contributes to extending the capabilities of bending-loss platforms and provides a structured foundation for future refinements. The following chapters describe the design, calibration, and validation of this approach, situating these contributions within the technical landscape established in this review.

CHAPTER 2

OPTOELECTRONIC PRESSURE SENSOR BASED ON THE BENDING LOSS OF PLASTIC OPTICAL FIBERS EMBEDDED IN STRETCHABLE POLYDIMETHYLSILOXANE

Alberto Alonso Romero[1], Koffi Novignon Amouzou[1], Dipankar Sengupta[1], Camila Aparecida Zimmermann[1], Andréane Richard-Denis[2], Jean-Marc Mac-Thiong[2], Yvan Petit[3], Jean-Marc Lina[1] and Bora Ung[1]

[1] Department of Electrical Engineering, École de Technologie Supérieure, 1100 Notre-Dame Street West, Montreal, QC H3C 1K3, Canada
[2] Hôpital du Sacré-Cœur de Montréal, 5400 Gouin Boul. West, Montreal, QC H4J 1C5, Canada
[3] Mechanical Engineering Department, École de Technologie Supérieure, 1100 Notre-Dame Street West, Montreal, QC H3C 1K3, Canada

Article published in the journal
Sensors (MDPI) on 22 March 2023
https://doi.org/10.3390/s23063322

Abstract: We report the design and testing of a sensor pad based on optical and flexible materials for the development of pressure monitoring devices. This project aims to create a flexible and low-cost pressure sensor based on a two-dimensional grid of plastic optical fibers embedded in a pad of flexible and stretchable polydimethylsiloxane (PDMS). The opposite ends of each fiber are connected to an LED and a photodiode, respectively, to excite and measure light intensity changes due to the local bending of the pressure points on the PDMS pad. Tests were performed in order to study the sensitivity and repeatability of the designed flexible pressure sensor.

Keywords: flexible pressure sensor; plastic optical fiber; polydimethylsiloxane; bending; light intensity; commercial electronic components; simple fabrication; cost-effective

2.1 Introduction

The quick advancement of science and technology in the fields of artificial intelligence, the Internet of Things, smart devices, new materials, power supplies, sensing modalities, and assembly techniques is providing impetus for the development of new flexible skin-like sensors based on flexible electronics (Butt, Kazanskiy, et al., 2022; Gao et al., 2019; Li et al., 2020). Electronic devices that can bend, stretch, and fit curved surfaces without losing functionality are known as flexible electronic sensors (Amjadi et al., 2016; Farooq & Zhang, 2022; Kazanskiy et al., 2022; Usman et al., 2023). These sensors can be attached to the human body (externally or internally) (Li et al., 2020; Wang et al., 2021) or civil structures (Gao et al., 2022; Lopez-Higuera et al., 2011) for a variety of promising applications in healthcare, biomedicine (Wang et al., 2021), human–machine interfaces, soft robotics, sports performance, wearable electronics (Amjadi et al., 2016; Li et al., 2020), structural health monitoring, security, and environmental monitoring (Gao et al., 2022; Lopez-Higuera et al., 2011; Min et al., 2021). Their ability to conform to surfaces by removing device motion or mechanical mismatch (Gao et al., 2019; Souri et al., 2020; Wang et al., 2021) enables continuous, dynamic, and accurate assessment of a variety of physiological parameters (pulse rate, body temperature, gait analysis, heart rate, sleep quality assessment (Butt, Kazanskiy, et al., 2022; Farooq & Zhang, 2022; Homayounfar & Andrew, 2020; Usman et al., 2023), tactile perception (Farooq & Zhang, 2022; Kazanskiy et al., 2022), pressure monitoring at pressure points in bedridden patients (Liu et al., 2014; Yousefi et al., 2011), detection of pressure areas in wheelchair patients (Chenu et al., 2013), muscle activity monitoring (Butt, Kazanskiy, et al., 2022; Homayounfar & Andrew, 2020; Kazanskiy et al., 2022), among others) or the detection of stress, cracks (Duan et al., 2020; Gao et al., 2022), or damage in bigger structures such as airplanes, bridges, buildings, or other civil constructions (Lopez-Higuera et al., 2011; Min et al., 2021; Ye et al., 2014).

These adaptable sensors are made of flexible materials and can be manufactured in a variety of shapes and sizes to detect various parameters, such as pressure, through various sensing principles (Bi et al., 2023; Homayounfar & Andrew, 2020), such as electrical resistance (Chen

& Yan, 2020; Chenu et al., 2013; Iglio et al., 2018), capacitance (Chen & Yan, 2020; Yip et al., 2009), piezo-electricity (Jeon et al., 2019), resonance (Min et al., 2021), or fluctuations in light intensity (Al-Mai et al., 2017; He et al., 2023). In contrast to rigid electronic devices, which have stricter shape limitations (Han et al., 2017), higher risk of mechanical failure (particularly when subjected to strain or deformation that is incompatible with their rigid structure) (Son et al., 2016), more difficult integration with tissues or organic materials (Heng et al., 2022), and higher weight and volume (Son et al., 2016; Wang et al., 2021), flexible electronics can combine a variety of electronic components with flexible material hosts that can withstand a wide range of strains, such as tension, compression, bending, or torsion (Duan et al., 2020; Li et al., 2020), with significant benefits including design flexibility, lightness and thinness, manufacturing versatility, and cost-effectiveness (Han et al., 2017; Kim et al., 2019; Leitão et al., 2022). These sensing devices must also comply with specific requirements, such as being bio-compatible (Shen, 2021; Souri et al., 2020), safe (Li et al., 2020; Shen, 2021; Souri et al., 2020), lightweight, non-toxic (Li et al., 2020), stretchable, flexible (Li et al., 2020; Souri et al., 2020), and hydrophobic (Duan et al., 2020; Wang et al., 2021), to ensure that they are tightly integrated and adhered to. Furthermore, as wearable health monitoring devices or human–machine interaction interfaces, their design should enable them to sustain sensing performance throughout long periods of use and extensive usage cycles (Duan et al., 2020; Gao et al., 2022; Li et al., 2020; Souri et al., 2020).

Several materials have been investigated to address the challenge of fabricating flexible sensors that allow for repeated application at maximum strain, including polyethylene terephthalate (PET), polyethylene (PEN), polyurethane (PU), polyimide (PI), polycarbonate (PC), polydimethylsiloxane (PDMS), hydrogels, and cellulose fibers. PDMS is a promising and effective host material for optoelectronics due to its outstanding deformability and ease of production (Gao et al., 2022; Li et al., 2020; Qi et al., 2021; Wang et al., 2021). The incorporation of optical fibers (OFs) into the host material (PDMS) could aid in the creation of flexible OF-based sensors. Optical pressure sensors, which detect variations in the intensity of light passing through or reflected from a pressure-sensitive material to measure pressure, are the most well-known OF-based sensors. These sensors use optical sensing techniques such

as total internal reflection, absorption, and light emission (Al-Mai et al., 2017; Homayounfar & Andrew, 2020; Min et al., 2021; Roriz et al., 2013). The most common optical pressure sensing approach is one based on mechanical deformation that changes the amount of light traveling through the optical fiber (Lopez-Higuera et al., 2011; Min et al., 2022; Sabri et al., 2015). This method is based on the idea that when an optical fiber is bent or curved, light is deflected, and some energy is lost due to dispersion. The amount of light lost is proportional to the sensor's curvature or bending. This change in light intensity can be measured with a photodetector, which allows the amount of pressure exerted to be calculated (Funnell & Thomas, 2023; Leitão et al., 2022). Sensors based on this technology have some advantages over rigid electronic sensors, such as electromagnetic immunity, corrosion resistance, electrical isolation, environmental resistance, compactness, being lightweight, and high sensitivity (Min et al., 2022; Roriz et al., 2013; Sabri et al., 2015), which makes them suitable for industrial, healthcare, and bio-medical research. In this paper, we propose combining plastic optical fibers into a flexible and elastic PDMS host to build a two-dimensional flexible and stretchable sensing pad.

2.2 Materials and Methods

2.2.1 Sensor Pad Manufacturing Process

The flexible sensor samples work under the sensing technique of optical intensity modulation, in which the actuation (via pressure) of the crossing or intersection point of fibers results in optical fiber bending loss. To study the working principle of the sensor and the performance of the selected electronic devices, two samples with different numbers of OFs were designed. The first sample consists of two PMMA plastic optical fibers (POFs) encapsulated in a PDMS pad, with both fibers having a diameter of 0.25 mm (Mitsubishi Chemical Super Eska™ Optical Fiber, SK-10; Industrial Fiber Optics, Inc., Tempe, AZ, USA) and a length of ~120 cm. To induce larger optical losses, one of the fibers was crossed perpendicularly on top of the other identical fiber to create a single pressure point (PP) at the intersection of both fibers (A1). For the second sample, the design consists of 4 such optical fibers in a grid array within a

PDMS pad, with the fibers parallel to each other and spaced by 1 cm. Two of the four POFs are crossed perpendicularly on top of the other two fibers, creating a two-row (A and B) by two-column (1 and 2) arrangement of POFs. The intersection of each row and each column is related to a local PP, giving a total of 4 pressure points (A1, A2, B1, B2). For both samples, care was taken during assembly of the intersection of fibers so that the columns (1 and 2) were always above (Up) and the rows (A and B) always below (Dwn) in the crossing.

To mold the PDMS into pads, LEGO® blocks were used to create square molds of 5 cm × 5 cm, in which precise holes were drilled on each side to allow the POFs to pass through according to the crossing order mentioned above. The fibers were then encapsulated in a 20:1 weight ratio PDMS (Dow Corning, Sylgard™ 184; Dow Corporate, Midland, MI, USA) base and curing agent mixture that was mixed for about 3 min using a magnetic stirrer. This ratio provides a good trade-off between the hardness and elasticity of PDMS for the purposes of this experiment and keeps the intersections of fibers in their positions. When the mixture was ready, it was poured into the mold to completely cover the fibers, thereby creating 5 cm × 5 cm × 0.8 cm pads. The PDMS pads were degassed for one hour in a vacuum chamber to eliminate microscopic air bubbles in order to ensure good material homogeneity. After degassing, the PDMS mold was left to cure at 35 °C for six hours, after which the pads were finally extracted via demolding once they had cooled to room temperature. The manufacturing process of the pads, their three-dimensional representation, and images of actual samples are shown in Figure 2.1.

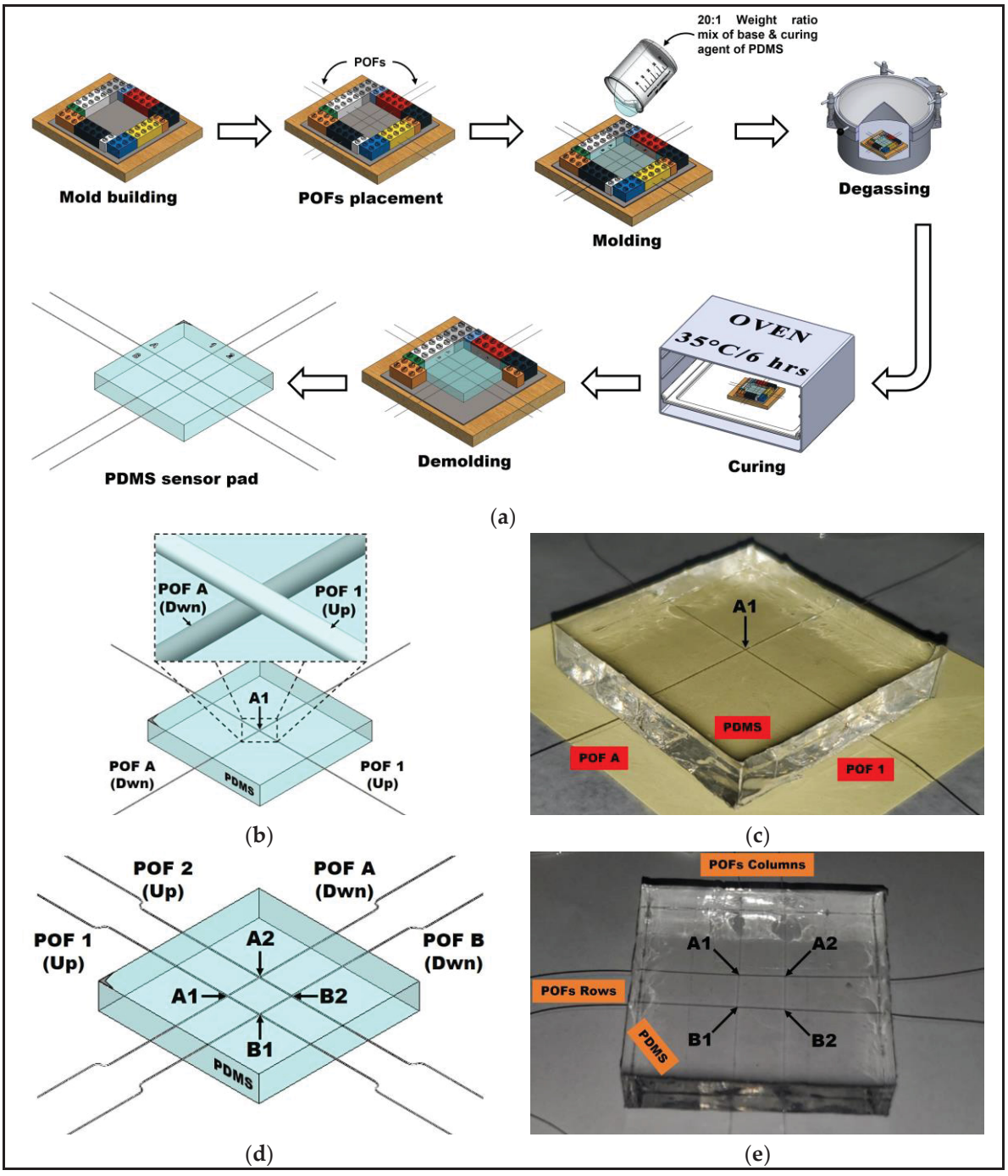

Figure 2.1 (a) Graphical representation of the manufacturing process of molding the sensor pads; (b) 3D model of the sample of 1 POF × 1 POF and the pressure point (A1) resulting from the intersection of the fibers; (c) real photo of the 1 POF × 1 POF sample and its pressure point A1; (d) 3D model of the 2 POFs × 2 POFs sample and its pressure points resulting from intersection of the fibers (A1, A2, B1, B2); (e) real photo of the 2 POFs × 2 POFs sample and its pressure points (A1, A2, B1, B2)

2.2.2 Low-Cost Electronics Design

In order to complete the optical fiber sensors' elements, low-powered and compact opto-electronics components were selected with the goal of favoring cost-effective integration into flexible sensor devices. Red LEDs (Marktech Optoelectronics, MTE7063NK2-UR; Marktech Optoelectronics, Inc., Latham, NY, USA) with a wavelength of 630 nm were coupled to one end of each fiber as a light source, while a photodiode (Marktech Optoelectronics, MTD3910N; Marktech Optoelectronics, Inc., Latham, NY, USA) with a response range of 400 to 1060 nm was coupled to the other fiber end in order to measure the change in light intensity through the fibers. ST active device mounts and ST connectors are used to couple light from LEDs going in to the optical fibers at the input with the photodiodes at the output, as shown in Figure 2.2.

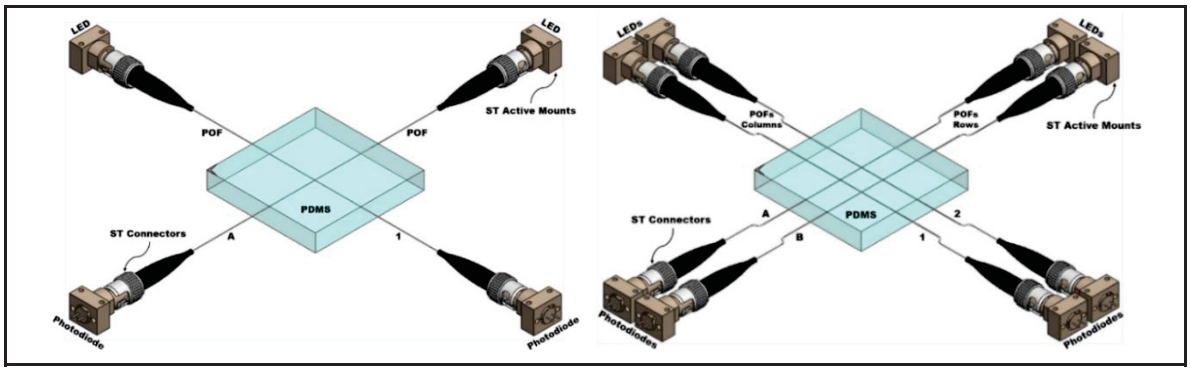

Figure 2.2 Three-dimensional models of the 1 POF × 1 POF and 2 POFs × 2 POFs sensor pads with the light sources (LEDs) and photodiodes coupled to each fiber

A measured light intensity (photodiode response) of a few µA was passed through a transimpedance amplifier (TIA) (Analog Devices, LTC6268; Analog Devices, Inc., Wilmington, MA, USA), which changed the low-level current signal of the photodiode to a usable voltage output (~4.5V). Finally, this voltage was passed through an active low-pass filter of 60 Hz with a gain of 1.5 to remove most of the electronic noise from the signal. The output signal of the whole electronic circuit, which was given the name photodiode voltage, is connected to a multimeter in order to visualize the voltage changes in response to the pressure exerted on the pressure points of the sensor pads (Figure 2.3).

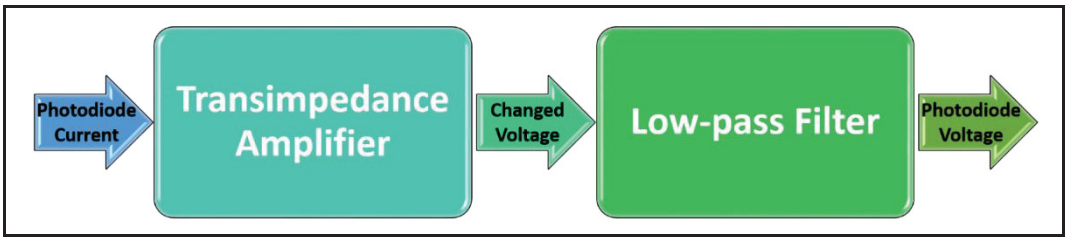

Figure 2.3 Block diagram of the electronic stages designed for the photodiodes of the sensor pads

2.2.3 Experimental Setups

The main interest is knowing the sensitivity and repeatability of the components selected for the manufacture of this flexible pressure sensor built with low-cost components. For doing that, the samples and the designed electronics were tested under two different configurations: (1) the use of scientific-grade equipment, designed and calibrated to make optical measurements, and (2) the use of a low-cost electronics setup. For each of these configurations, two measurement repetitions were carried out for each sample, in which the pressure points of each sample pad were individually tested by applying a vertical force of 0 N to 40 N with the help of a force gauge (REED Instruments, SD-6020; REED Instruments, Wilmington, NC, USA) and a 1 cm diameter 3D printed impactor. In accordance with the vertical force applied with the force gauge and the area of the circular face of the 3D printed impactor, the samples were stressed from 0 kPa up to ~509 kPa (Figure 2.4).

For each test and repetition, the same experimental protocol was followed. This started by placing the sensor pad on a metal plate and manually placing each PP under the impactor on the force gauge tip. The impactor was then placed so that it lightly touched the top face of the pad without applying any pressure (0 kPa), and a light and photodetector stabilization period was used to obtain the initial value of light intensity (voltage). The pressure was then increased to ~63 kPa (or 5 N of applied force), and after a stabilization period of a few seconds, which is when the measurement devices give a steady reading, the new light intensity value (voltage change) was recorded. Later, the pressure was increased to ~127 kPa (10 N) and the new light intensity value was recorded. After this point, the pressure increments were made every ~127

kPa until ~509 kPa was reached. When the last pressure was reached, the output light intensity was recorded and it was withdrawn, with a rest time given for materials to recover their original shape. We then proceeded to perform a second repetition on the same PP following the same steps mentioned above. After the second repetition, the pad was moved to the next PP and everything was repeated.

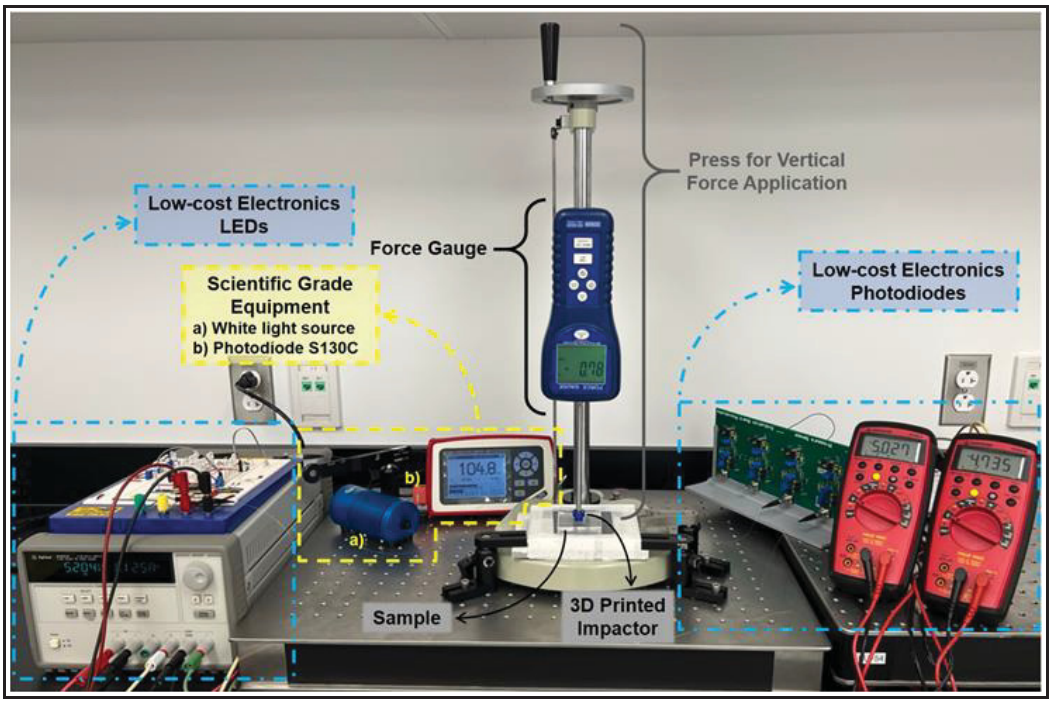

Figure 2.4 Tools and equipment used in experimental setups

For the benchmark measurements with scientific-grade equipment, once the pad was placed in the described setup, the scientific-grade equipment, a halogen white light source (Ocean Optics, HL-2000-HP Light Source; Ocean Optics (Ocean Insight), Orlando, FL, USA), and a calibrated photodiode (Thorlabs, Photodiode S130C; Thorlabs Inc., Newton, NJ, USA) were attached to each end of a fiber. The HL-2000-HP light source was coupled to the POFs using a Thorlabs' Universal Bare Fiber Terminator (Thorlabs, BFT1; Thorlabs Inc., Newton, NJ, USA), and the S130C photodiode was placed opposite and as close as possible to the other end of the fiber without any connector or coupling, as shown in Figure 2.5.

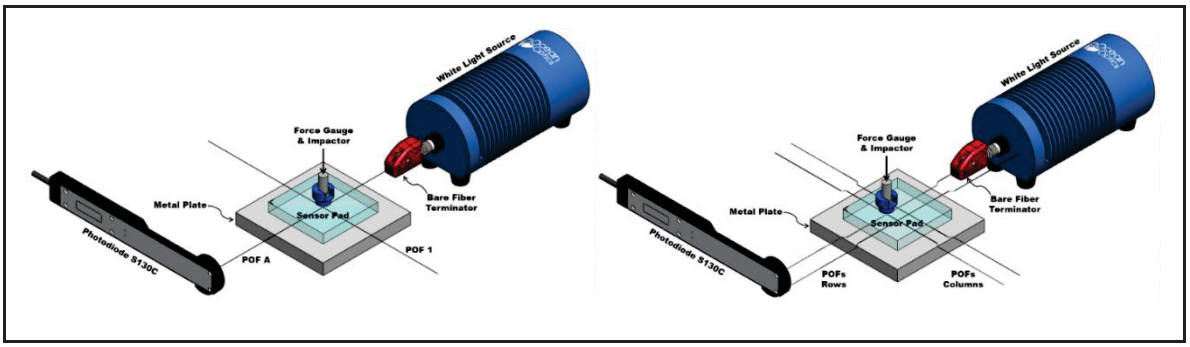

Figure 2.5 Three-dimensional representation of the experimental setups used to expose the 1 POF × 1 POF (left) and 2 POFs × 2 POFs (right) samples to the pressures selected with the scientific equipment

For the characterization of low-cost electronics, after testing the samples with the scientific-grade equipment specifically designed for optical measurements, the previously used equipment was replaced with the designed low-cost electronics. To obtain the peak emission wavelength of the LED, the supply voltage was regulated to obtain a current of 20 mA using a variable trimpot resistor. Similar to the previous setup, all visible light LEDs, photodiodes, and optical fibers were coupled using ST active mounts and ST connectors. The parameters of the electronic amplifier and filter circuits were adjusted by their variable gain resistors so that the output would give an approximate value of 5 V. Following the described experimental protocol, each PP was stressed at the selected pressures, and each new photodiode voltage was recorded manually (Figure 2.6).

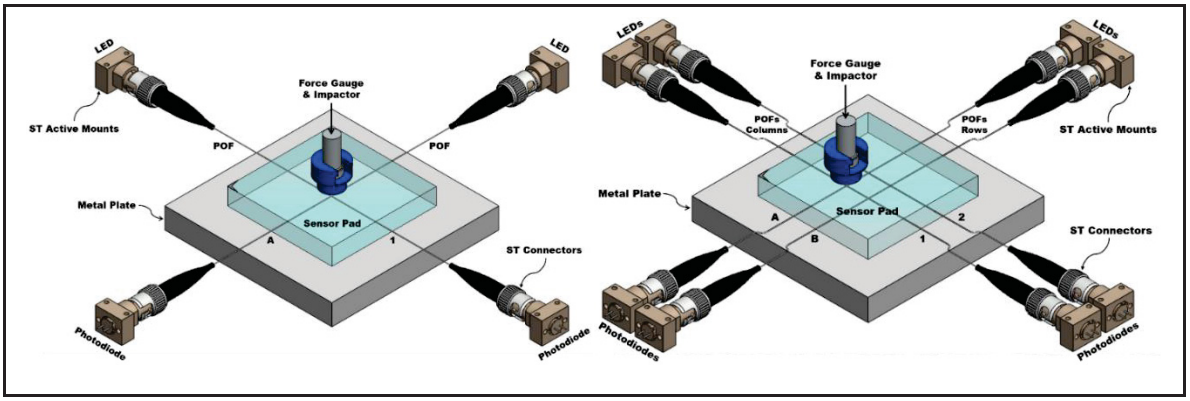

Figure 2.6 Three-dimensional representation of the experimental setups used to expose the 1 POF × 1 POF (left) and 2 POFs × 2 POFs (right) samples to the pressures selected with the LEDs and photodiodes coupled to each fiber

2.3 Results

2.3.1 Benchmark Measurements with Scientific-Grade Equipment

The results obtained from this test will serve as a reference for the repeatability and sensitivity of the samples to different values of applied pressure based on the measurements obtained with scientific-grade equipment. Following the experimental protocol described above, each PP was subjected to the selected range of pressure values, and corresponding changes in the photodiode voltage from the S130C photodiode were recorded. Using this equipment, the reference response curves of each PP of each sample were obtained (Figures 2.7 and 2.8), in which a non-linear and repetitive response can be observed in each measurement, indicating that the higher the pressure exerted, the lower the light intensity at the exit.

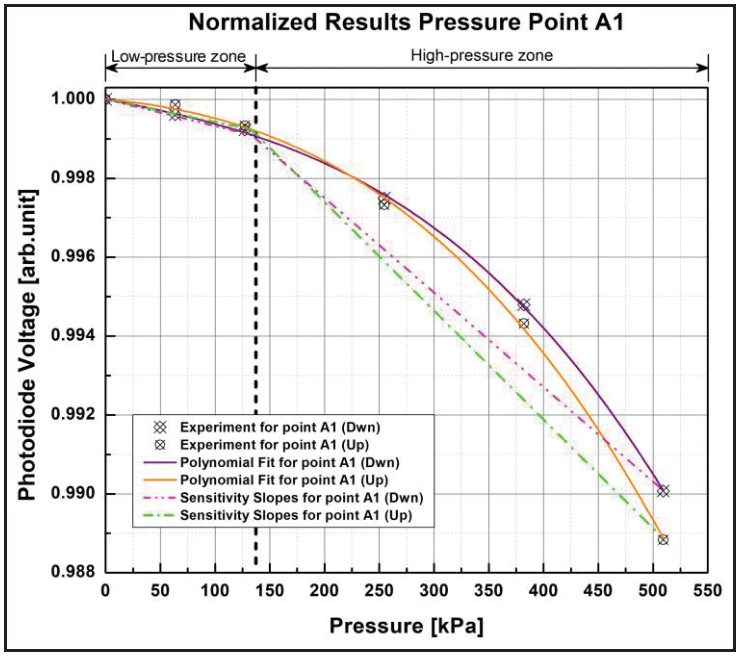

Figure 2.7 Normalized response curves of the 1 POF × 1 POF sample with the scientific-grade equipment setup for pressure point A1. The experimental data points correspond to the average of two test repetitions

In the non-linear response of both samples, it can be observed that they begin to show small changes around 63 kPa to 127 kPa, while there is greater light attenuation from ~127 kPa to ~509 kPa. For this reason, two pressure zones were defined for the measurements according

to the graphical perception of changes in photodiode voltage; therefore, there is a low-pressure zone from 0 kPa to ~133 kPa and a high-pressure zone from ~133 kPa to 550 kPa to help with analysis of the results. As can be seen in the graphs, the changes in voltage are more pronounced in the high-pressure zone as pressure increases, which would indicate that the samples are more sensitive to higher pressures. In contrast, in the low-pressure zone (below 133 kPa), the light intensity changes have a smaller magnitude than those of the high-pressure zone, which may indicate that the tested sample cannot distinguish pressure changes below this threshold.

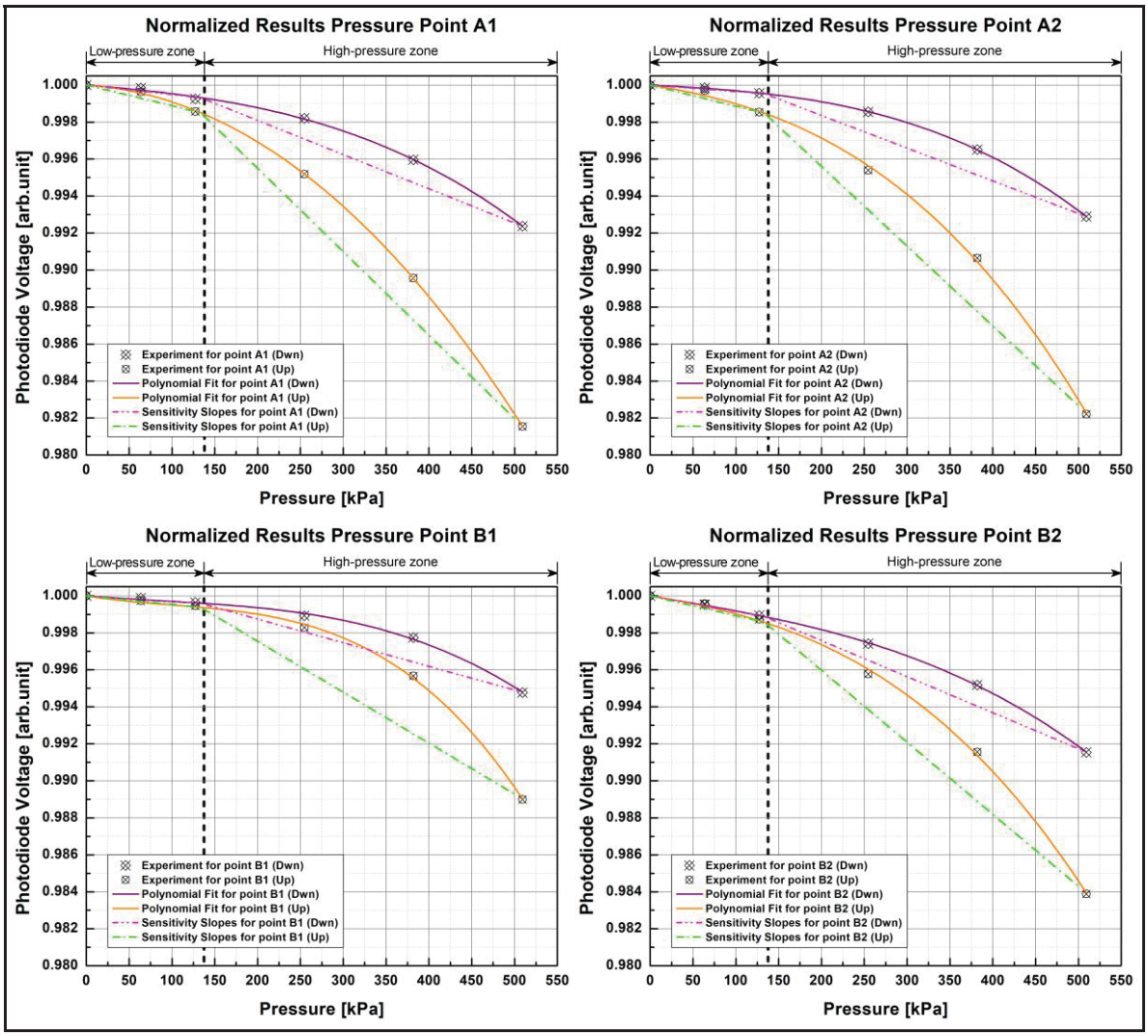

Figure 2.8 Normalized response curves of the 2 POFs × 2 POFs sample with the scientific-grade equipment setup at different pressure points. The experimental data points correspond to the average of two test repetitions

In order to verify this, the average of the results obtained from each repetition of each fiber was calculated. Polynomial fit was obtained by the polynomial functions

$$f(x) = a_n x^n + a_{n-1} x^{n-1} + \cdots + a_2 x^2 + a_1 x + a_0 \quad (2.1)$$

that best define the response of each fiber. The function that best describes the average of each pair of repetitions of every fiber was a third-order function (n = 3), where the coefficients a_3, a_2, and a_1 were calculated and the coefficient a_0 restricted to 1 ($a_0 = 1$) by the normalization of results. The third-order functions that characterize these curves have a goodness of fit (GOF) of $R^2 = 0.9995$, $R^2_{adj} = 0.9992$, and $RMSE = 1.1301 \times 10^{-4}$ and were used to obtain photodiode voltage in the low- and high-pressure zones defined in order to calculate the average slope of each zone (dash-dot and dash-dot-dot lines in Figures 2.7–2.10). In general, for the 1 POF × 1 POF sample, it was found that the low-pressure zone had an average slope of -6.227×10^{-6} arb. unit/kPa, while the high-pressure zone had a slope of $-2.576 \times$ arb. unit/kPa. On the other hand, the 2 POFs × 2 POFs sample had an average slope of -7.221×10^{-6} arb. unit/kPa for the low-pressure zone and -2.790×10^{-5} arb. unit/kPa for the high-pressure zone. Comparing these results, it can be seen that the samples did indeed have greater sensitivity to high pressures owing to their steeper slope. Similarly, it can be observed in all the graphs that, despite being in the same PP, the fibers at the top (Up) of the fiber crossing of each pressure point were more sensitive than the one lying at the bottom (Dwn) because they suffered from greater attenuation of light due to fiber bending loss.

By evaluating the relative standard deviation (RSD) of the results obtained for each value of applied pressure, we can see that the 1 POF × 1 POF sample has, on average, an $RSD = 0.0427\%$, while for the other sample (2 POFs × 2 POFs), the RSD value is equal to 0.0280%. The low RSD percentage indicates high measurement precision, i.e., low dispersion between each measurement and the average of the repetitions.

2.3.2 Characterization of Setup Using Low-Cost Electronics

After testing the samples with scientific-grade equipment, this was replaced with the designed low-cost electronics. This test helped to investigate whether the selected photodiode and the designed electronics are sensitive enough to detect small optical signal changes when pressing the PPs.

The normalized response curves of each sample for this test (Figures 2.9 and 2.10) show a non-linear and repetitive behavior very similar to that of the previous test, albeit with a smaller amplitude. In comparison with the previous test, it can be seen that within the low-pressure area, the light changes are minimal and begin to be appreciated, in most cases, from ~127 kPa onwards. Furthermore, light intensity varied within the range of $0.980\ \text{arb. unit}$ to $1\ \text{arb. unit}$ with the scientific-grade equipment, while for this test using low-cost components it was within the range of $0.990\ \text{arb. unit}$ to $1\ \text{arb. unit}$, making the response curves flatter than the previous ones; however, they still show a more significant attenuation in light intensity as pressure increases and enters the high-pressure zone. This suggests that the samples tested with the low-cost electronics also could not distinguish pressure changes below the 133 kPa threshold. This reduced magnitude or flattening of the curves results in a loss of sensitivity when using the low-cost electronics. Further, as in the previous test, the slopes in each pressure zone were calculated to see how the sensitivity of the pads was affected by the change in light source and photodetector.

In the low-pressure zone, the photodiode voltage changes were very small, and, after having calculated the slopes with the third-order functions (2.1) with a GOF of $R^2 = 0.9934$, $R^2_{adj} = 0.9891$, and $RMSE = 1.3987 \times 10^{-4}$, it is noticeable that the 1 POF × 1 POF sample has an average slope of $-1.275 \times 10^{-6}\ \text{arb. unit/kPa}$, and that the 2 POFs × 2 POFs sample has an average slope of $-1.735 \times 10^{-6}\ \text{arb. unit/kPa}$, both of which are lower than the values obtained for the low-pressure zone in the test with scientific-grade equipment. Similarly, for the high-pressure zone, slopes of $-1.216 \times 10^{-5}\ \text{arb. unit/kPa}$ and $-9.464 \times 10^{-6}\ \text{arb. unit/kPa}$ were obtained for the 1 POF × 1 POF and 2 POFs × 2 POFs samples,

respectively, presenting greater slopes than those of the low-pressure zone and reinforcing that the samples studied are more sensitive to high pressures. However, these slopes are not as steep as those obtained for this pressure zone in the reference test, confirming that there is a loss of sensitivity with low-cost electronic components. A comparison shows that there is an average loss of 66.1659% in sensitivity for the 1 POF × 1 POF sample with the low-cost electronics, which is 71.0284% for the 2 POFs × 2 POFs sample when compared to the reference scientific setup.

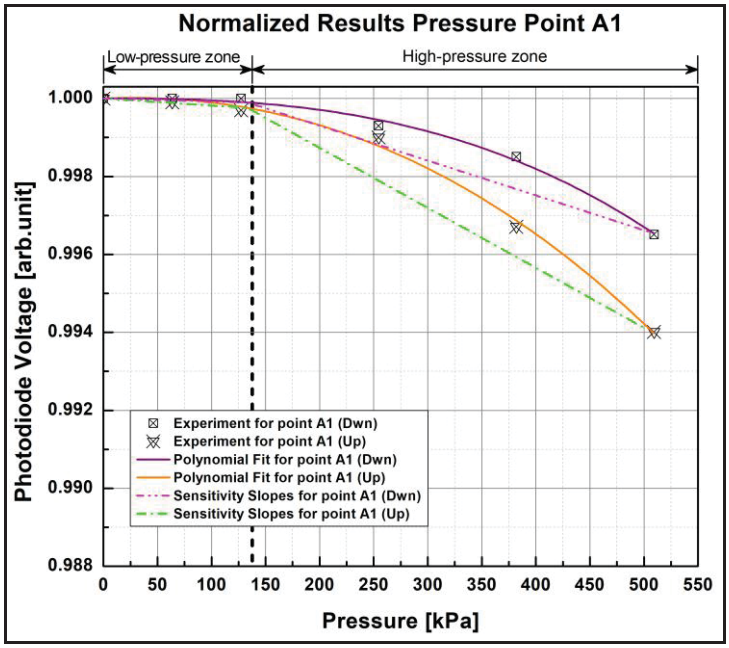

Figure 2.9 Normalized response curves of pressure point A1 for the 1 POF × 1 POF sample with the low-cost electronics setup. The experimental data points correspond to the average of two test repetitions

Despite having lower sensitivity than the scientific-grade configuration, it can be seen that the pads keep their sensitivity at higher pressures by having a steeper slope than the low-pressure zone, making the attenuation of light intensity greater as the pressure increases. Additionally, the low-cost electronics designed to detect light changes when the fibers of each PP are pressed present a non-linear and repetitive behavior similar to that of the scientific equipment, although not as severe. As in the previous case, it can be seen that the fiber at the top (Up) of the crossing in most cases exhibits higher optical attenuation and therefore greater sensitivity than the fiber located just below (Dwn).

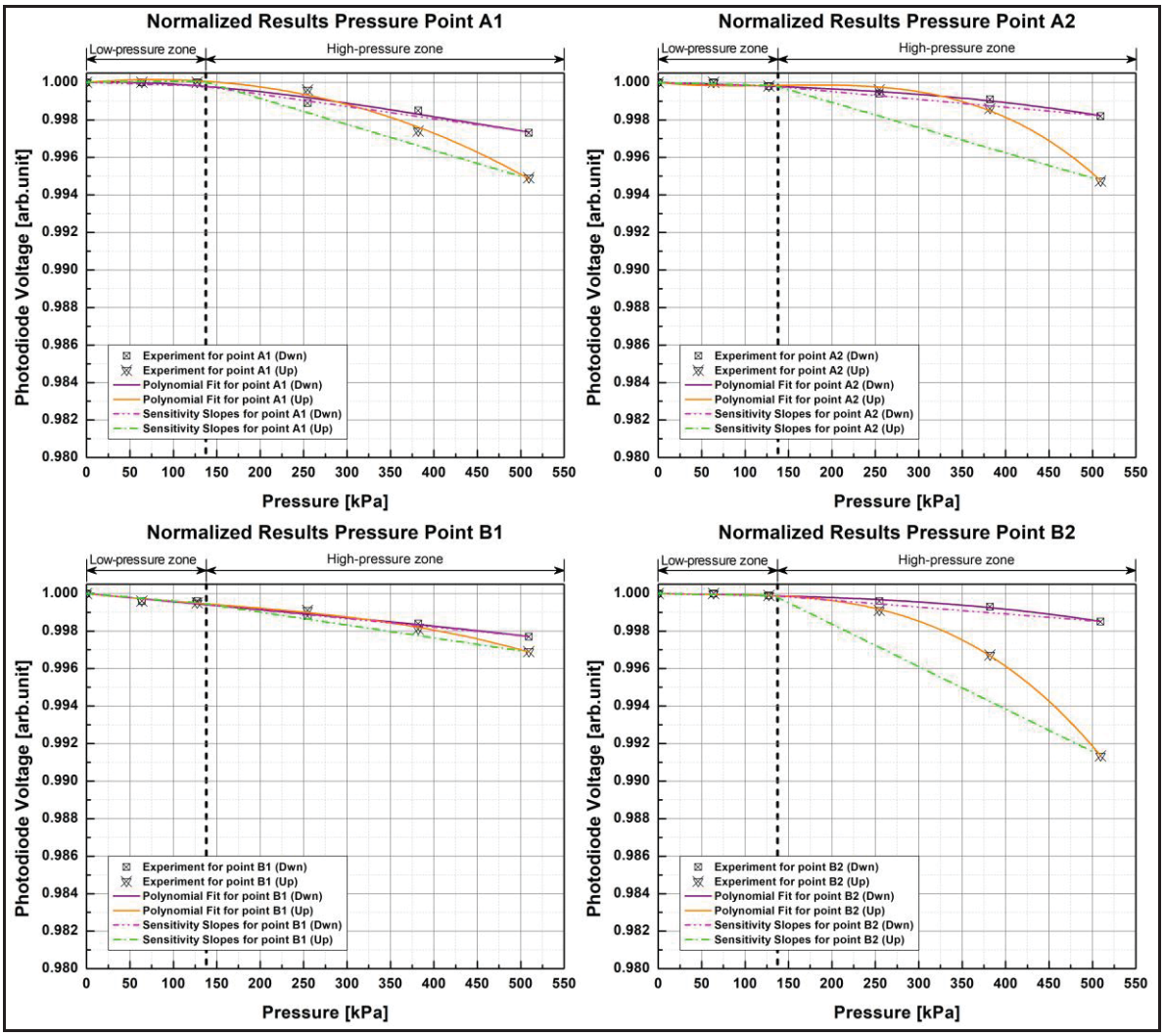

Figure 2.10 Normalized response curves of the 2 POFs × 2 POFs sample with the low-cost electronics setup at different pressure points. The experimental data points correspond to the average of two test repetitions

The RSD of the results of the samples with the designed low-cost electronics is 0.0270% for the 1 POF × 1 POF sample and 0.0368% for the 2 POFs × 2 POFs sample. As in the previous test, low RSD indicates high measurement repeatability. Comparing these results with those of the reference test, we can see for the 1 POF × 1 POF sample that the RSD of the low-cost electronics setup is 0.0157% lower than that of the scientific-grade equipment. This comparison could appear to suggest that low-cost electronics present higher measurement precision than specialized equipment; however, this is not so, since we can see in the low-pressure zone (Figure 2.9) that the results of both repetitions are minimal. There is no change

at all here, and you can even go so far as to say that the samples were insensitive in this zone. This makes evaluations of RSD come out with a lower average value since the results without change (SD = 0) are left out of the calculations. Similarly, when comparing the results of the second sample, it is observed that the low-cost electronics setup had a higher RSD and that the difference with the scientific equipment was 0.0088%, which indicates that there is some loss of precision. Likewise, the slight difference between both dispersions is because the changes in the low-pressure zones (Figure 2.10) of each pressure point are minimal or nonexistent with the electronic elements, which causes some of them to be left out (SD = 0) of the calculations, thus resulting in lower RSD.

Finally, in Figure 2.11, we note the difference between light intensity values when the applied pressure was gradually and continuously applied upward and then reversed at PP A1 of the 1 POF × 1 POF sample with the low-cost electronics setup. Since the sensor is made of flexible and stretchable materials, we observe that the response curves (Figure 2.11) present some small hysteresis behavior, with curves overlapping in their maximum and minimum endpoints. Because PMMA and PDMS are both amorphous and viscoelastic materials, the observed small hysteresis may be attributed to a combination of chain relaxation, changes in free volume (Beloshenko et al., 2006), and stress softening (Grosch et al., 1968). Stress softening is believed to be a primary factor for hysteresis in elastomers such as PDMS (Grosch et al., 1968). This has been observed in silica-filled PDMS, such as Sylgard 184, and is thought to arise from a decrease in filler–PDMS chain interaction and chain entanglement (Hanson et al., 2005; Yan et al., 2010). It can also be seen in these curves that, to reach minimum light intensity in the range of evaluated pressures, the same amount of pressure is required, irrespective of whether the fiber is placed on the top (Up) or bottom (Dwn) position.

Generally speaking, the purpose of these tests was to gradually compare the functionality, precision, repeatability, and performance of the low-cost designed elements against scientific-grade equipment. Comparing the normalized response curves of each test, it can be observed that the response of the electronic components presents a non-linear and repetitive behavior similar to that of the scientific equipment, in which photodiode voltage decreases as pressure

increases. It can be seen in the results graphs that the greatest changes in light intensity were generated mainly in the high-pressure zones, i.e., above 133 kPa, which indicates that the materials are more compressed and deformed above this pressure. In all our tests, we were able to deform the sensor pads by over 40% compared to their initial uncompressed state without causing permanent damage. All samples were also able to recover their initial state after testing. The higher sensitivity of samples above this pressure may be due to the fact that the thickness of the pad prevents the fibers from sensing the lower pressure values since there is no significant deformation or bending of the underlying POF.

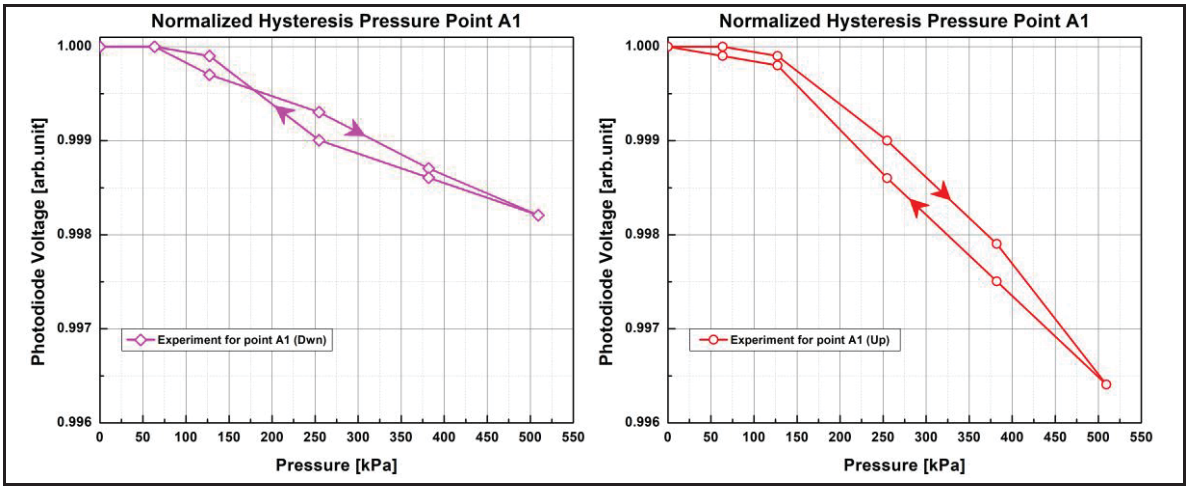

Figure 2.11 Hysteresis curves of the 1 POF × 1 POF sample with the low-cost electronics setup at pressure point A1. The experimental data points correspond to the average of two test repetitions. The arrows indicate the direction of applied pressure (i.e., downward and then upward)

It was to be expected that the low-cost electronics would experience a loss of sensitivity compared with the scientific-grade equipment. Some of the factors that could explain this loss of sensitivity would be the large coupling losses (>30 dB) observed between the LED light sources and the photodiode detectors. This meant that the low power incident on the photodiodes generated a very low current value (~1.4 µA). Additionally, even though the TIA used had the needed characteristics to amplify these low currents, a very high gain value had to be implemented, which, in some cases, reached the electronic limits of the TIA. Another factor that could have affected the results is the low number of repetitions for each PP since only two were made with each sensitive pad in each test. A higher number of repetitions will

give more results, which will increase the dispersion between them; consequently, the RSD will vary and will be able to give an updated precision value.

Another factor that could have influenced the results is the manufacturing processes of the optical fiber supplier. Although the fiber samples used for the sensor came from the same manufacturing batch, the diameters of the core and cladding varied slightly from length to length, causing their diameter to be non-uniform. Such small differences can create discrepancies when assembling the grid array of fibers for the pads. For example, discrepancies in dimensions between the top and bottom fibers can prevent them from remaining in contact after PDMS is poured into the mold, thus creating an imperfect contact point between the fibers that prevents them from properly deforming when pressed upon. We believe that this is what happened in the measurements from point B1 of the 2 POFs × 2 POFs sample (Figures 2.8 and 2.10) since, as can be noted in the graphs, the changes in light intensity are significantly smaller (approximately 45% loss in sensitivity) compared to the other pressure points. This indicates that the current manual and labor-intensive manufacturing process is prone to errors.

Despite this, the results obtained help to conclude that the selected electronic components fulfilled their functions as light sources and photodetectors since the fibers were kept illuminated at all times and their light intensity changes were detected; these changes were mainly detected at high pressures, starting at 133 kPa, exhibiting good repeatability despite having lower sensitivity and precision.

2.4 Conclusion

This paper describes the simple fabrication and proof-of-concept demonstration of a soft materials-based pressure sensor embedded with a network of plastic optical fibers. Custom molds were used to encapsulate a number of fibers into a single-layer configuration of polydimethylsiloxane (PDMS) host material that was square pad-shaped. Commercial LED sources and photodiodes were used in an intensity modulation scheme for monitoring the pressure values on the flexible pad. Based on the good repeatability and wide dynamic

measurement range obtained with this configuration, the implementation of this type of sensor could benefit industrial applications (e.g., industrial robotics, manufacturing, or structural health monitoring) where a large range of pressures (0 to 550 kPa) must be monitored. This demonstration was limited in terms of the absolute sensitivity achieved ($< 10^{-5}$ arb. unit/kP), which remained low due to the strong hardness of the PMMA fibers used in this work. A promising approach to explore in the future to improve the sensitivity of this type of sensor is to use softer plastic fibers such as elastomers. This work represents another step towards the integration of flexible sensing optical fibers within stretchable material hosts which will allow for the fabrication of flexible, accurate, conformable, and cost-effective sensors.

Author Contributions: Conceptualization and design of experiments, A.A.R., K.N.A., J.-M.L., and B.U.; methodology and the conducting of experiments, A.A.R., K.N.A., and D.S.; modeling and interpretation of results, A.A.R., K.N.A., C.A.Z., A.R.-D., J.-M.M.-T., Y.P., J.-M.L., and B.U.; project supervision the provision of resources, A.R.-D., J.-M.M.-T., Y.P., J.-M.L., and B.U. All authors have read and agreed to the published version of the manuscript.

CHAPTER 3

PERFORMANCE EVALUATION OF FLEXIBLE OPTICAL PRESSURE SENSORS USING INVERSE MODEL-BASED PRESSURE MAPPING

Alberto Alonso Romero[1], Koffi Novignon Amouzou[1], Dipankar Sengupta[1], Jean-Marc Lina[1] and Bora Ung[1]

[1] Department of Electrical Engineering, École de Technologie Supérieure, 1100 Notre-Dame Street West, Montreal, QC H3C 1K3, Canada

Article published in the journal *Applied Sciences* (MDPI)
Special Issue "State of the Art in Smart Materials and Flexible Sensors"
on 20 February 2026

Abstract: This work presents a signal processing and reconstruction system developed for a flexible optical pressure 2D mapping sensor. The sensor consists of a two-dimensional grid of polyurethane optical fibers (PU-OFs) embedded in polydimethylsiloxane (PDMS), which acts as the input device for acquiring light intensity changes caused by external surface-applied pressure. In this study, we propose a system to process these signals through an inverse model based on the Moore-Penrose pseudoinverse for spatial localization, along with a point-specific pressure estimation model to infer the magnitude of the applied force, which is then used to generate quantitative pressure maps. Experimental results show the system's overall performance, robustness, and repeatability across multiple pressure levels and locations. In most cases, localization errors remain below 5 mm, while pressure estimation errors are around 5 mmHg when the pressure is correctly localized. Performance metrics, such as recall, specificity, and precision, support the system's ability to detect, localize, and reconstruct pressure events with consistent reliability. These results establish the viability of the proposed methodology for potential integration into low-cost and flexible optical fiber-based 2D pressure monitoring systems for biomedical applications.

Keywords: flexible optical pressure sensor; polydimethylsiloxane (PDMS); polyurethane optical fibers (PU-OFs); localization model, pressure estimation, pressure mapping; performance metrics; inverse model; pseudo-inverse; ROC analysis.

3.1 Introduction

Flexible pressure sensors have become fundamental elements in modern sensing technology used in wearable bioelectronics (G. Huang et al., 2025; Z. Huang et al., 2025; G. Li et al., 2025; Mao et al., 2024; Sun et al., 2025; Zavanelli et al., 2025), robotics (Zhijian Chen et al., 2025; Jia et al., 2024; X. Li et al., 2025; Meng et al., 2024; Yu et al., 2025; Zhang et al., 2025), human–machine interfaces (H. Chen et al., 2025; Guo et al., 2025; Kim et al., 2024; Yuxia Li et al., 2024; Tchantchane et al., 2025; D. Wang, B. Li, et al., 2025; D. Wang, G. Ma, et al., 2025), preventive medicine (Ali et al., 2025; Amouzou et al., 2025; Babangida et al., 2025; Bijender et al., 2024; T.-S. Chang et al., 2025; J. Huang et al., 2025; Majumder et al., 2025; Shang et al., 2025; Tian et al., 2024; Jia Xu et al., 2025; Yoon et al., 2024; Hao Zhang et al., 2024), and sports monitoring (D. Chen et al., 2025; Gao & Chen, 2023; Y. Wang et al., 2025; Zeng et al., 2024; X. Zhang et al., 2024; J. Zhao et al., 2024). In particular, for 2D mapping applications, novel pressure-sensing devices have been developed in recent years for various applications (Aptabusjaman et al., 2025; de Carvalho et al., 2025; Im & Kim, 2024; Katrenova et al., 2022; Ke et al., 2025; Kisannagar et al., 2025; H. Li et al., 2025; Lu et al., 2024; Peruzzi et al., 2025; Shabalov et al., 2024; Takeda et al., 2024; Tang et al., 2024). Their rapid evolution is driven by advances in materials science, structural engineering, device fabrication, and the demand for high sensitivity, adaptability, and multifunctionality in a connected world (Yan Huang et al., 2019; Kim & Oh, 2020; D. Xu et al., 2025). These sensors are mainly classified according to their transduction mechanism, such as piezoresistive, capacitive, piezoelectric, triboelectric (Y. Guo et al., 2024; Kim & Oh, 2020; Yu et al., 2022; Zhao et al., 2023), electrochemical (Huang et al., 2024; Xue et al., 2024; Yang et al., 2024; Hongjian Zhang et al., 2024), transistor-based, magnetoelastic (Kim & Oh, 2020; Lu et al., 2025; Schwartz et al., 2013; Shu et al., 2025; R. Wang et al., 2025; Jing Xu et al., 2025), and optical sensors (Gan et al., 2024; Karimian et al., 2025; Taharat et al., 2025).

Piezoresistive sensors work on the principle of converting applied pressure on the device into measurable electrical resistance changes (Y. Guo et al., 2024; Li et al., 2020; X. Wang et al., 2025; Yan et al., 2024). The resistance variation is mainly due to the deformation of the

sensor's structure, which modifies the contact surface between the conductive elements, the conductive pathways, the tunneling distances between the conductive elements, or the intrinsic resistivity of the material, resulting in a measurable variation in resistance (Li et al., 2020; Ruth et al., 2020; X. Wang et al., 2025; Yu et al., 2022). Capacitive sensors operate similarly to a parallel plate capacitor, commonly used due to their simple structure design, where applied pressures translate into changes in the capacitance through modifications in electrode separation distance, the effective area of E-field overlap, or the dielectric constant of the material between them. The pressure-induced deformation of the structures results in a capacitance signal directly related to applied force (Kim & Oh, 2020; Li et al., 2020; Ruth et al., 2020; Yu et al., 2022). The piezoelectric sensors use a transduction method that utilizes voltage generated in certain materials in response to applied mechanical stress (Kim & Oh, 2020; Li et al., 2020; Yu et al., 2022). Piezoelectric pressure sensors are generally manufactured with a sandwiched fabrication modality that incorporates a charge-generating piezoelectric material layer between two vertically aligned electrode layers (Wang & Song, 2006). However, most piezoelectric sensors are fabricated using inorganic materials, which, due to their hardness, lead to a low signal-to-noise ratio, making these devices unsuitable for obtaining high output signals (Meng et al., 2022). Triboelectric sensors are based on the coupling of contact electrification and electrostatic induction (charge transfer from friction/contact between two materials) (Kim & Oh, 2020; Li et al., 2020; Yu et al., 2022). When two materials with different triboelectric polarities are brought into contact by external pressure and then separated, a potential difference is created, which drives a flow of electrons in an external circuit (Li et al., 2020). Triboelectric sensors are thus self-powered and provide electrical signals in response to dynamic pressures. The basic structure of this kind of sensor relies on a composite material, integrating conductive materials into flexible substrates (Yan Huang et al., 2019; Shen, 2021; D. Xu et al., 2025; Yu et al., 2022). The substrates are predominantly flexible and stretchable with materials such as polydimethylsiloxane (PDMS), polyimide (PI), polyethylene terephthalate (PET), polyurethane (PU) (Y. Guo et al., 2024; Yan Huang et al., 2019; Li et al., 2020; Schwartz et al., 2013; Yan et al., 2024), polytetrafluoroethylene (PTFE) and nylon (Meng et al., 2022), with a growing interest in green, biodegradable options like textiles, paper, silk, and hydrogels for enhanced wearability,

biocompatibility, and sustainability (Li et al., 2020; D. Xu et al., 2025). Furthermore, the sensing or conducting elements are made from diverse materials, including highly conductive carbon-based nanomaterials like graphene and carbon nanotubes (CNTs) (Li et al., 2020; Schwartz et al., 2013; Shen, 2021; D. Xu et al., 2025), metallic elements such as silver or gold nanowires and liquid metals (Li et al., 2020; Schwartz et al., 2013; D. Xu et al., 2025), and conductive polymers like PEDOT: PSS and polyaniline (Li et al., 2020; Yan et al., 2024). Other functional materials, such as piezoelectric polymers (e.g., PVDF) and ceramics (e.g., ZnO, $BaTiO_3$), are used to create self-powered sensors, while emerging 2D materials like MXene are being explored for their unique properties (Y. Guo et al., 2024; Li et al., 2020; Schwartz et al., 2013; D. Xu et al., 2025; Yan et al., 2024).

Despite recent advances, flexible pressure sensors still face several challenges, such as a relatively fast degradation over time due to oxidation and mechanical stress (D. Xu et al., 2025; Yan et al., 2024), malleability during manufacturing that can impact homogeneity and performance (D. Xu et al., 2025), the use of expensive materials like gold and costly fabrication (Kim & Oh, 2020; Yanru Li et al., 2024; D. Xu et al., 2025), challenges in scaling mass production (Ruth et al., 2020; Tan et al., 2022; D. Xu et al., 2025; Zhao et al., 2023), susceptibility to temperature fluctuations, parasitic capacitance, and electromagnetic interference (Y. Guo et al., 2024; Tan et al., 2022; D. Xu et al., 2025). Some sensors are primarily suited for dynamic measurements and cannot typically detect static pressure or suffer from instability without proper encapsulation (Yan Huang et al., 2019; Meng et al., 2022; Tan et al., 2022; D. Xu et al., 2025). In addition, many of the materials used do not present good durability, biocompatibility, and stability for biomedical applications (Yan Huang et al., 2019; Li et al., 2020; Yanru Li et al., 2024; Meng et al., 2022). Achieving robust adhesion between layers to prevent delamination, ensuring sensors can withstand long-term use and repeated mechanical stress without degradation, and protecting them from environmental factors like humidity or electromagnetic interference are persistent challenges that must be overcome for reliable and practical application (Y. Guo et al., 2024; Tan et al., 2022; D. Xu et al., 2025).

Optical fiber-based sensors present some advantages like electromagnetic immunity, no rust, electrical isolation, environmental resistance, compatibility, lightweight, and high sensitivity, making them suitable for biomedical research and implementation (Kanellos et al., 2010; Ochoa et al., 2021; Zhang et al., 2019), consumer applications, and environmental sensing (Butt, Voronkov, et al., 2022; Sweeney et al., 2021).

Recently, polymer materials have been considered among the most promising options for the manufacturing of a new generation of pressure-sensing devices due to their good optical, thermo-mechanical properties (Stankova et al., 2016; Zahid et al., 2017; Zimmermann et al., 2025) and biocompatibility. In particular, PDMS, which is part of the family of elastomeric materials, is a promising pressure-sensing platform owing to its high stretchability, high thermal stability, biocompatibility, easy processing, and chemical inertness. It can be directly adhered to human skin, implanted into the body, or incorporated into clothes thanks to its non-toxic nature. In addition, PDMS has high optical transparency from the near-UV to the near-infrared range, which broadens its applicability as a flexible material for opto-electronic applications, and in particular, for the development of wearable and non-invasive biophysiological sensors and polymer-based optical sensing approaches (Li et al., 2020; Pan'kov, 2025; Wang et al., 2021).

Previous optical pressure sensors based on bending loss or polymer waveguides often face a trade-off between operating range, spatial resolution, and system complexity. Several reported designs achieve large intensity variations under high loads in the hundreds of kilopascals (i.e., $\gtrsim$750 mmHg), but their response becomes less discriminative at low pressures, where reduced signal contrast and mechanical damping can hinder accurate reconstruction (Amouzou et al., 2025; Jeroen et al., 2010; Soetanto et al., 2011; Wang et al., 2008). At the other extreme, configurations based on dense fiber Bragg grating (FBG) arrays or optical frequency-domain reflectometry (OFDR) can reach millimetric or even sub-millimetric spatial resolution, but typically require bulky or expensive instrumentation (Kanellos et al., 2010; Katrenova et al., 2022; Shabalov et al., 2024; Zhang et al., 2019). Moreover, some optical pressure-mapping approaches have adopted learning-based or data-driven models to improve localization and

magnitude estimation, often at the cost of higher complexity and the need for large training datasets (de Carvalho et al., 2025; Shabalov et al., 2024; Wang et al., 2008). In grid-based configurations, when a limited set of intensity measurements is used to infer pressure at multiple predefined locations, the resulting mapping may become ill-conditioned in practice. In such cases, robust inverse formulations are needed to recover pressure distributions from those measurements.

In this context, we report the integration of a flexible optical pressure sensor with a mathematical processing framework based on an inverse model and point-specific pressure estimation models. The system consists of a 4 × 4 grid of polyurethane optical fibers fully encapsulated in a PDMS pad, defining 41 measurement points, and a dedicated data analysis model based on the Moore–Penrose pseudoinverse. Using the photodiode response signals and low-cost optoelectronic circuits, the system reconstructs two-dimensional pressure maps and allows the stimulus to be localized with a characteristic error below 5 mm, while estimating its magnitude with mean errors close to 5 mmHg when the location is correct. In contrast to approaches that rely on learning-based or data-driven techniques to improve localization or estimation, we adopt a strategy based on physical models, which preserves the interpretability of the system without requiring large training datasets and establishes a solid baseline for subsequent refinements. Taken together, the experimental results show that the proposed system provides accurate pressure localization and estimation with high sensitivity and low localization error across the studied pressure range.

3.2 Materials and Methods

3.2.1 Physical Sensing System

3.2.1.1 Flexible Optical Sensor Pad Manufacturing

The flexible sensor sample works based on the sensing technique of optical intensity modulation, where the application of pressure at the intersection points of fibers results in

optical fiber bending loss (Alonso Romero et al., 2023). This study aims to evaluate the performance of a two-dimensional pressure mapping device based on a grid array of polyurethane optical fibers (PU-OFs) and an inverse model to solve the resulting ill-conditioned system. The fibers, with a diameter of 1 mm and a length of ∼400 mm each, were chosen to optimize the transmission of the light source used in the experiments, minimizing scattering due to the lack of cladding while keeping enough for sensing by bending loss. Polyurethane fibers (Soft Flex Company™, Stretch Magic Elastic Cord®; Sonoma, CA, USA) were selected for their flexibility, elastic recovery, transparency, and durability, properties that allow them to bend under pressure, return to their original shape, and withstand repeated use without permanent damage. Although Stretch Magic Elastic Cord® is primarily an artisanal material used for beading and DIY jewelry, it proved to be suitable for this application. A cutback test performed on the material revealed an attenuation of approximately 0.24 dB/cm, which characterizes the average optical loss of the fibers used in the prototype.

The PU-OFs were arranged in a 4 × 4 grid within a PDMS pad, aligned parallel to each other, and spaced 10 mm among them. The principle of operation of this kind of grid configuration has been investigated previously (Alonso Romero et al., 2023; Chang et al., 2012; Wang et al., 2005); therefore, the sample consists of four PU-OFs crossing perpendicularly over another set of four fibers, making a grid structure of four columns by four rows of PU-OFs. Each intersection of the columns and rows corresponds to a pressure point, creating a total of 16 pressure points (PPs) for sensing, labeled A1, A2, …, D3, D4, where the upper fibers in the grid were labeled with letters (A to D), while the lower fibers were labeled with numbers (1 to 4) (see Figure 3.1c). During assembly, care was taken to keep the correct placement of the fibers, with the columns (A to D) placed above (Up) and the rows (1 to 4) placed below or down (Dwn) the columns at the intersections.

To mold the PDMS into a pad shape, a reusable multi-part acrylic mold composed of one base and four lateral walls was fabricated with a CO_2 laser cutter (Trotec Laser GmbH, Speedy 360; Marchtrenk, Austria). The precision of this method allows the fabrication of guide holes on the four lateral walls with a diameter matching that of the PU-OFs (1 mm), allowing the fibers to

be positioned and aligned during fabrication. In two opposite walls, the guide holes were drilled 1.5 mm above the mold base, corresponding to the center height of the lower fiber layer, while in the remaining two walls, the guide holes were located 2.5 mm above the base, corresponding to the center height of the upper fiber layer. This configuration places the fiber intersections (PPs) 2 mm from the mid-height of the PDMS pad. To prevent fiber displacement, the fibers were gently fixed externally without stretching or deforming them, remaining aligned wall-to-wall through the guide holes during the PDMS molding process (Figure 3.1d, left). This modular fabrication approach can be scaled by increasing the mold dimensions and the number of guide holes to place additional fibers. However, fabricating larger PDMS pads with this method increases the mm-scale alignment and handling requirements needed to maintain consistent spacing and positioning throughout manufacturing, which can be achieved in practice through repeatable industrial processes. Moreover, the optical fiber loss (0.24 dB/cm) currently limits the size of the square sensor pad to around half a meter.

A 20:1 weight ratio of base and curing agent mixture of PDMS (Dow, Sylgard™ 184; Midland, MI, USA) was used as this ratio provides an optimal balance between stiffness and elasticity, while keeping the encapsulated fibers securely in place. The mixture was poured into the mold to fully cover all 8 fibers with a self-leveling of 4 mm height. Taking into account the spacing between fibers and to minimize edge effects, the final pad dimensions are 70 mm × 70 mm × 4 mm. The mold with the PDMS mixture was placed in a vacuum chamber (Vinmax, 5-gallon vacuum degassing chamber kit; Shenzhen, Guangdong, China) to eliminate air bubbles and ensure material homogeneity. Degassing was performed for ∼1 h at approximately 0.6 bar below atmospheric pressure (≈−60 kPa), using successive vacuum/vent cycles to promote bubble expansion and removal. After degassing, the pad was cured in a laboratory oven (Fisher Scientific Company, 825F; Ottawa, ON, Canada) at 35 °C for 6 h and demolded once cooled to room temperature. Demolding was performed by first removing the mold base and carefully separating the cured PDMS pad, followed by the sequential removal of the lateral acrylic walls while minimizing mechanical stress on the embedded fibers. The smooth inner surfaces of the acrylic mold reduced adhesion and facilitated release. The manufacturing process and the resulting flexible sensor sample pad are illustrated in Figure 3.1.

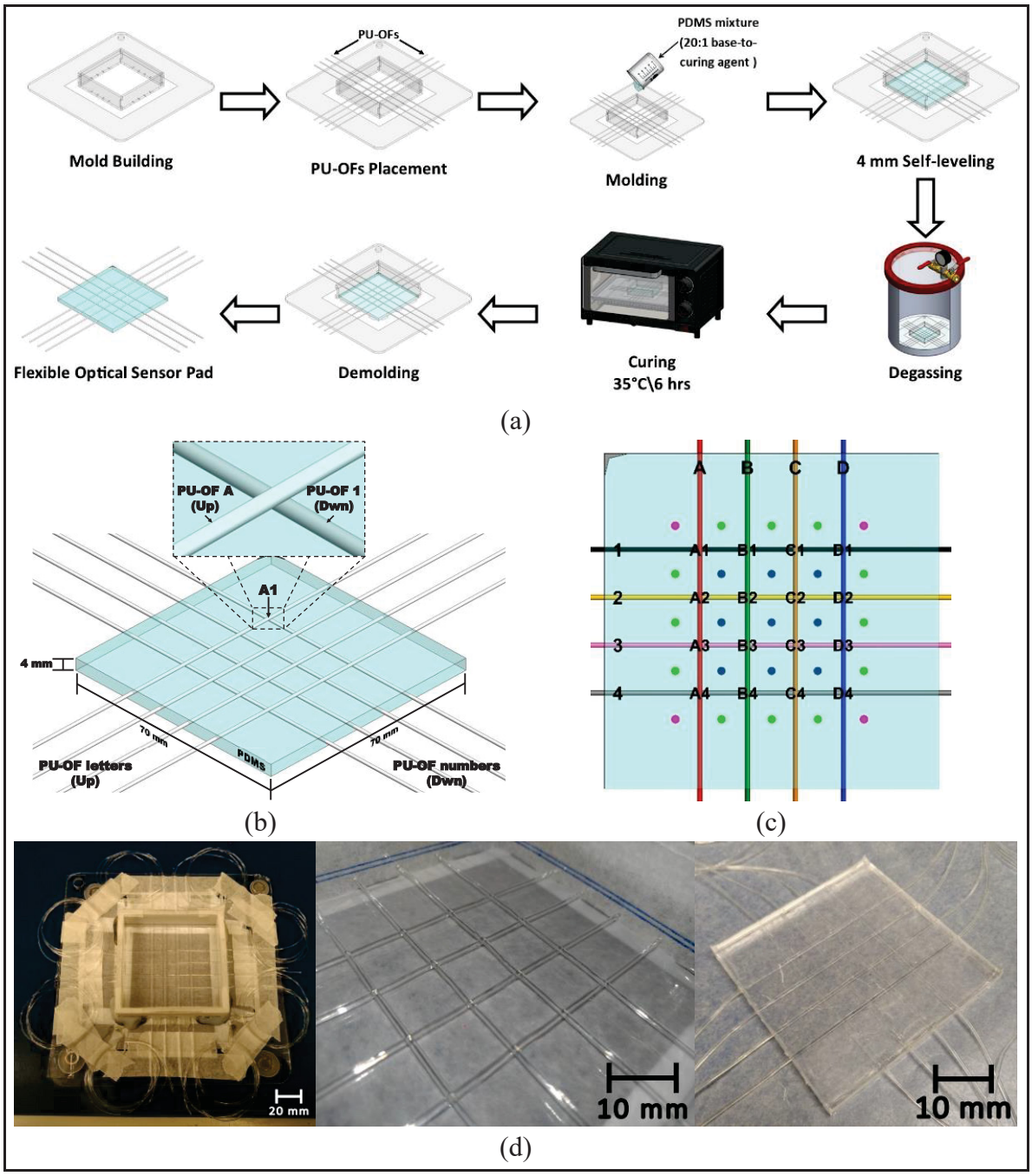

Figure 3.1 (a) Manufacturing process of molding the flexible sensor sample pad; (b) Model of the flexible sensor sample pad of 4 PU-OFs × 4 PU-OFs and an example of a pressure point (A1) resulting from the intersection of the fibers; (c) Location of all 16 pressure points (black characters) and 25 intermediate points (blue, green, and magenta points); (d) Mold, assembly, and resulting flexible sensor sample pad

3.2.1.2 Experimental Setup

For each test point investigated, 10 measurement repetitions were carried out, where the pressure points (PPs) and the intermediate points (IPs) of the flexible sensor were individually tested (see Figure 1c). A vertical force ranging from 0 N to 1 N was applied using a force gauge (REED Instruments, SD-6020; Wilmington, NC, USA) and a 3D-printed plastic impactor tip with a 10 mm diameter. According to the applied force and the circular area of the impactor, the points on the sensor pad were subjected to pressures ranging from 0 mmHg to approximately 95 mmHg (Figure 3.2).

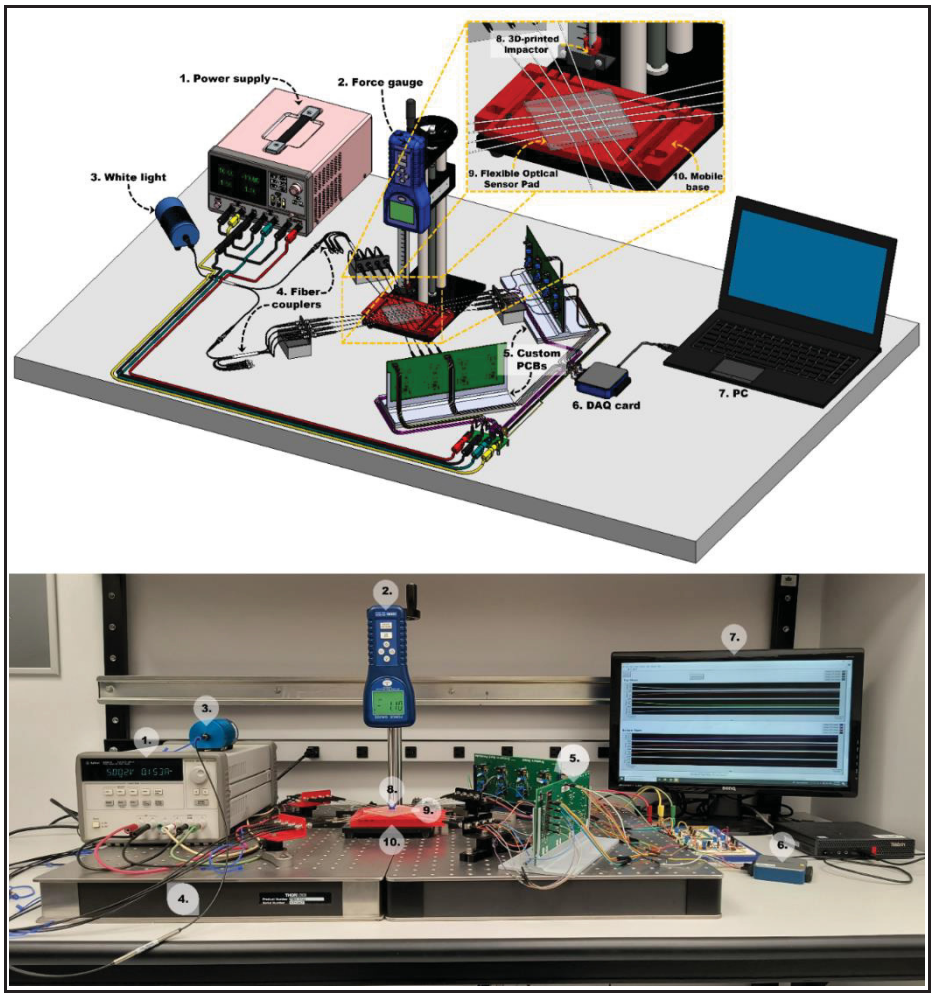

Figure 3.2 Tools and equipment used in the experimental setup. The numbered labels correspond to the same components in both the schematic (top) and the experimental setup (bottom).

Each test began by placing the sensor pad on a mobile plastic base, manually positioning each PP or IP under the impactor at the tip of the force gauge. The impactor was positioned to slightly touch the pad's surface without applying pressure (0 mmHg), followed by a stabilization period of 30 s to allow the flexible materials of the sensor to mechanically stabilize before recording the light intensity reading. The pressure was progressively increased in steps of 16 mmHg. After each increment, a short stabilization period was provided to ensure a steady reading for the new light intensity value (or photodiode voltage change) was achieved and recorded. This procedure was repeated until reaching a maximum pressure of ~95 mmHg. Subsequently, the pressure was completely released, and a rest period of 2 min was given to allow the materials to return to their original shape before proceeding with the next repetition. Each of the 10 repetitions at the same PP or IP followed this same procedure. After completing all repetitions at a given PP or IP, the pad was positioned to the next test location, and the procedure was repeated.

The sensor system used optoelectronic components specifically developed to ensure the integration between devices. A halogen white light source (Ocean Optics, HL-2000-HP Light Source; Orlando, FL, USA) with an output power of 20 W was used to optically excite the polyurethane fibers in the sensor pad. Light was distributed equally to the eight sensing fibers using three optical fiber couplers: one 1-to-2 coupler (Industrial Fiber Optics, Inc., POF Coupler 1 × 2; Tempe, AZ, USA) and two 1-to-4 couplers (Industrial Fiber Optics, Inc., POF Coupler 4 × 4; Tempe, AZ, USA). The eight outputs of the two 1-to-4 couplers were each connected one-to-one to the eight PU-OFs by means of SMA-to-SMA mating sleeves (Thorlabs Inc., ADASMA; Newton, NJ, USA), since both the coupler outputs and the fiber inputs were SMA-terminated. This configuration ensured stable optical coupling and mechanical alignment between the couplers and the sensing fibers.

To detect voltage changes owed to the intensity of light transmitted through the sensing fibers, custom-developed electronic boards (PCBs) were used. The role of the circuit boards consisted of the signal acquisition and processing from the compact and low-powered components, whose key elements are the photodiodes (Marktech Optoelectronics, MTD3910N; Latham,

NY, USA) with a response range of 400 to 1060 nm. The photodiodes are connected via male SMA connectors glued on the PU-OFs integrated in the PDMS pad to the female SMA connectors attached on the custom-made boards. The photodiode response, which is a low-intensity current in the range of a few nA, is amplified using a transimpedance amplifier (TIA) (Analog Devices, Inc., LTC6268; Wilmington, MA, USA), which converts the current signal to a voltage output (~3.5 V). This voltage signal was subsequently passed through an active low-pass filter with a cut-off frequency of 60 Hz and a gain of 1.5 to reduce electronic noise.

3.2.2 Data Acquisition and Characterization of the Physical Sensing System

The 8 outputs of the PCBs containing the photodetectors were connected to a data acquisition (DAQ) card (National Instruments, USB-6001/6002/6003; Austin, TX, USA), where the voltage changes generated by pressure applied to the pressure points were recorded. At each pressure level and each PP or IP, the 8 output values were stored in a *.xlsx Microsoft Excel file for subsequent data analysis and processing. The overall flow from signal acquisition to data processing and storage is summarized in the block diagram shown in Figure 3.3.

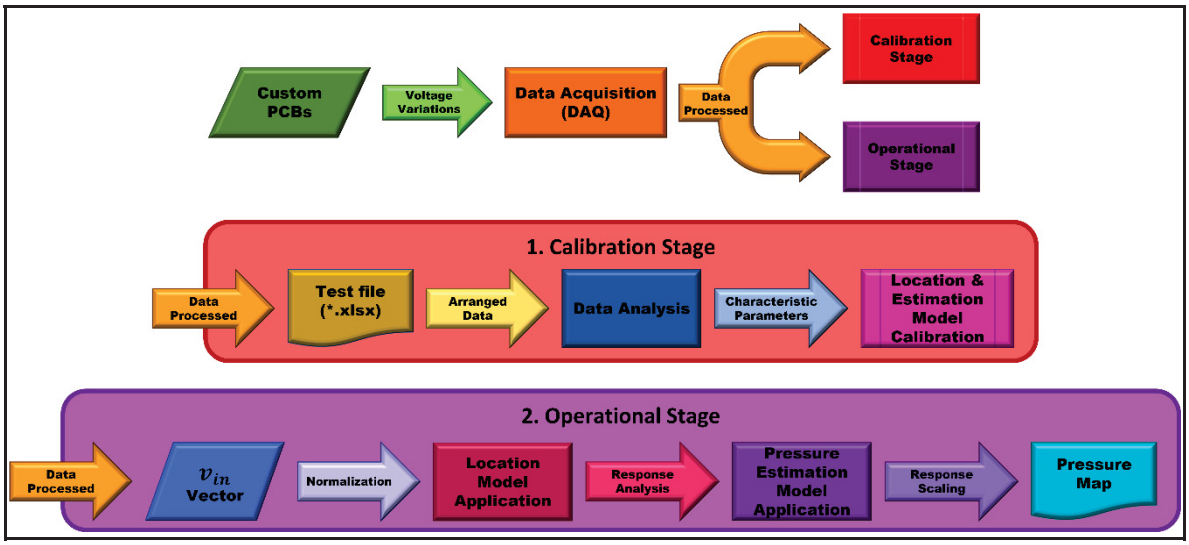

Figure 3.3 Block diagram of the data acquisition, analysis, and selection process used to extract characteristic parameters for the development of mathematical models for location and pressure estimation. The red and purple blocks represent the calibration and operational stages, respectively, while arrows indicate the data processing flow

The data stored in the *.xlsx file corresponds to the voltage changes recorded at each of the 16 pressure points and 25 intermediate points of the sensor during the 10 repetitions of the experimental process. To generate response graphs and analyze the sensor's behavior, the obtained values were averaged and normalized, facilitating their interpretation.

As shown in Figure 3.4a, corresponding to a pressure point, such as A1, and because of the configuration of the fiber grid, only the two fibers forming the PP respond to the pressure applied. In this case, two lines exhibit a steeper negative slope, indicating a voltage decrease as pressure increases when they are directly compressed. This suggests that applying pressure at the PP simultaneously affects both fibers. Previous studies (Alonso Romero et al., 2023) have demonstrated that despite sharing the same point, fibers respond differently depending on their configuration at the crossing and due to unique optical fiber transmission and coupling efficiencies at the connectors. Furthermore, the fiber positioned on top, i.e., close to the surface where the impactor is applied, experiences greater voltage loss due to increased compression from the overlap, leading to higher fiber bending optical losses. Additionally, some fibers show a slight voltage drop, likely caused by deformation of the encapsulating material (PDMS) or mechanical/electronic coupling effects, while the voltage signal from the other fibers remains virtually unchanged, indicating they are located far from the pressure zone.

In contrast, when the pressure is applied outside the crossing of a PP, the adjacent fibers are partially compressed. This is mainly due to the position of the impactor, which causes a non-uniform deformation, resulting in slight differences between response curves. The number of affected fibers depends on the location of the intermediate point. For practical purposes, the sensor area was divided into internal and edge zones, following the color legend used in Figure 3.1c. The edge zone (identified by magenta circles) includes the corner IPs (AA0.5, DD0.5, AA4.5, and DD4.5) with only two fibers responding to pressure; and the edge IPs (AB0.5, BC0.5, CD0.5, AA1.5, AA2.5, AA3.5, DD1.5, DD2.5, DD3.5, AB4.5, BC4.5, and CD4.5) are identified in lime green circles, with three fibers affected. On the other hand, the internal zone comprises the inner IPs (dark blue circles; AB1.5, BC1.5, CD1.5, AB2.5, BC2.5, CD2.5, AB3.5, BC3.5, and CD3.5) where four fibers respond simultaneously, along with the PPs

(denoted by the black characters, e.g., B2) that are located at the fiber crossings. For testing the IPs and PPs, the impactor was positioned at the center of the area defined by the surrounding fibers for IPs, and directly over the crossing for PPs.

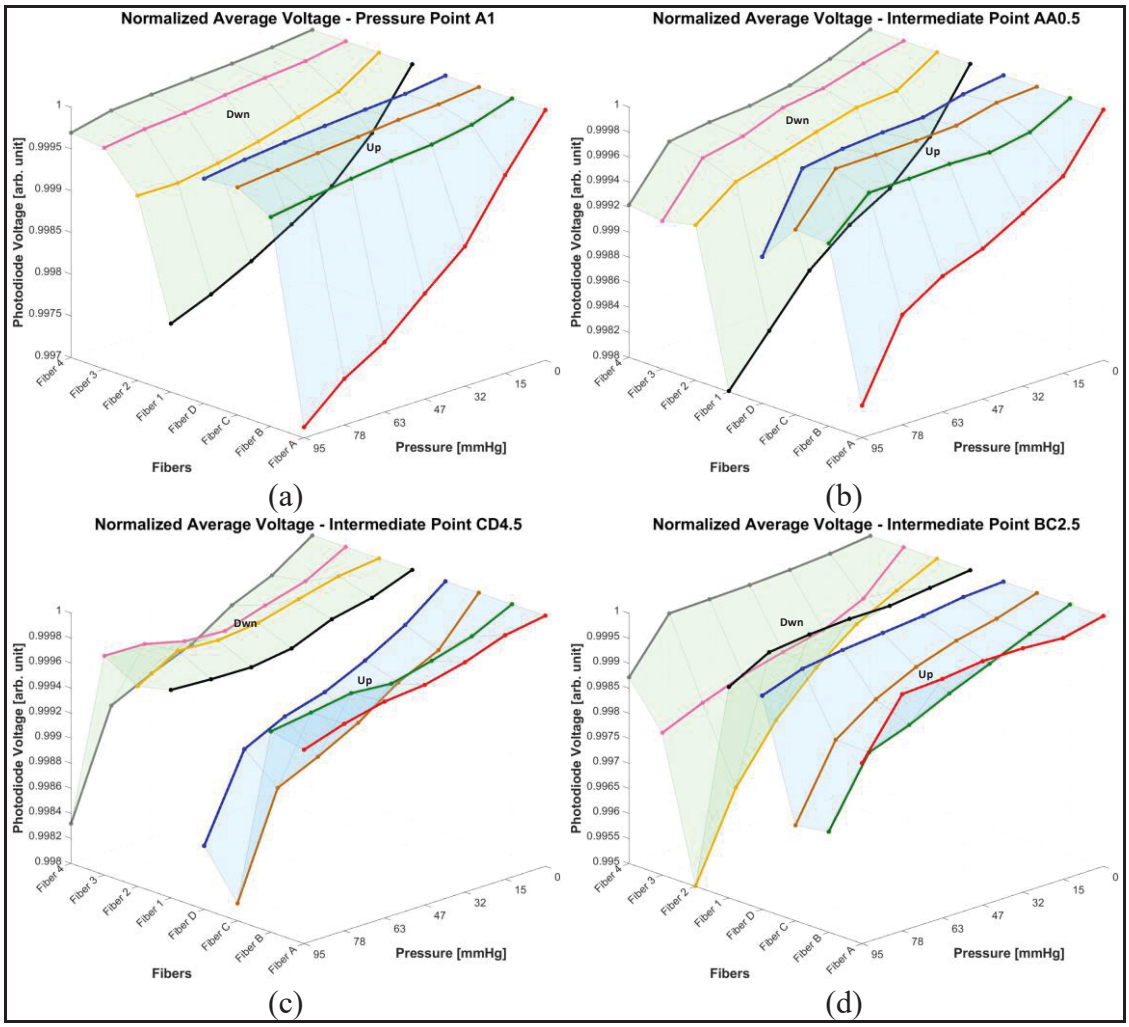

Figure 3.4 Example of normalized response curves of the flexible sensor sample pad. (a) Experimental data points correspond to pressure point A1; (b) Experimental data points correspond to the corner intermediate pressure point AA0.5; (c) Experimental data points correspond to the edge intermediate pressure point CD4.5; (d) Experimental data points correspond to the internal intermediate pressure point BC2.5. The experimental data points correspond to the average of ten repetitions. Colored lines represent each sensing fiber (A-D and 1-4), following the color coding shown in Figure 1c

Figure 3.4b shows the typical sensor response to pressure applied on a corner IP (i.e., AA0.5). In this case, the nearest fibers (Fibers A and 1) exhibit similar slopes, though with minor

differences in their rate of voltage decrease with applied pressure. These small differences may be attributed to a more evenly distributed pressure, as well as factors such as height differences between the top surface of the pad and the fiber positions, slight inaccuracies in the impactor positioning, or mechanical and electronic noise. Other fibers located further away from the point of application exhibited a mostly stable response, albeit with small voltage variations ostensibly due to the deformation of the encapsulating PDMS material and other secondary effects such as mechanical and/or electronic coupling noise, thus indicating they were unaffected by the applied pressure.

Graphs 3.4a and 3.4b illustrate the system's response to two different configurations: directly at the crossing of two fibers (i.e., A1) and at a nearby point where they are only partially compressed (i.e., AA0.5). As expected, the two closest fibers to the applied pressure points show a significantly more pronounced response curve compared to the other fibers located further away from the pressure application, with the IP point presenting the steeper slope (i.e., sensitivity) compared to the curve corresponding to the IP point.

Three different fibers are partially affected when the pressure is applied at an edge IP (Figure 3.4c). This configuration varies from previous cases, where only two fibers were involved. The results show that the three pressed fibers (Fibers C, D, and 4) also experience a negative slope in their response curves, showing that their voltage decreases as the pressure increases. Their voltage reductions are similar, suggesting that the applied pressure is distributed almost equally among the affected fibers. Again, small variations in behavior can be attributed to differences in fiber positioning, impactor alignment, and secondary effects such as host material deformation and\or mechanical–electronic coupling. The remaining fibers (Fibers A, B, 1, 2, and 3) show minimal changes in their response, indicating that they are not directly involved in the pressure zone. However, the slightly varying behavior observed in these fibers may result from the same indirect effects, such as PDMS deformation, mechanical coupling, or electronic noise. All edge IPs, with similar configuration, exhibit a similar response pattern, confirming the reproducibility of this response behavior.

Finally, when the pressure is applied at an internal intermediate point (e.g., BC2.5 located in the middle of the sensing pad), four fibers are affected by the applied force. Similarly, to the previous cases, where the pressure was almost equally distributed among fibers, for these internal locations, the results are nearly balanced across the nearest affected fibers. Looking at Figure 3.4d, it can be seen that these four fibers (Fibers B, C, 2, and 3) show a gradual voltage decrease as pressure increases. Differences in response between the fibers are minimal, suggesting that the pressure is being applied across all four fibers mostly equally, as expected.

Small uneven responses, as illustrated in the fiber 2 response curve (Figure 3.4d), can again be ascribed to minor differences in fiber positioning, uneven material response, or mechanical coupling effects derived from the contact between the impactor and the pad. Even so, the measured sensor response for IP locations was quite consistent overall for the nearest fibers, while other farthest fibers showed a mostly constant response, as expected.

The integration of the 25 intermediate pressure points enhances the sensor's spatial resolution (41 pressure points in total), as it is not only based on the responses of the 16 pressure points directly aligned with crossed fibers. By analyzing the behavior of the surrounding areas, it could enable a more precise identification of the specific point or region where the pressure is applied to the flexible sensor pad. Using the voltage variations recorded at each pressure level, work as the reference level of the characterization (i.e., via the so-called G matrices) of the inverse model implemented in this project. These matrices play a fundamental role in mapping the sensor's response, enabling a mathematical reconstruction of the pressure distribution across the sensing area of the pad.

3.3 Results

3.3.1 Description of the Data Analysis Software

3.3.1.1 Calibration and Building of the Inverse Model

Inverse model implementation in sensor systems is a useful method for interpreting and evaluating experimental data. The theory of the Moore–Penrose pseudoinverse (Equation 3.1), which is a mathematical generalization that makes optimal solutions possible for overdetermined systems such as the one described here, is the core of this work. This approach was chosen because it can handle nonrectangular matrices and provide singular solutions to the system.

$$R = G^t (GG^t)^{-1} v_{in} \tag{3.1}$$

The matrices G used in the developed system are obtained from the initial physical characterization of the sensing system (described in Section 3.2.2). Specifically, inside the G matrices, each row corresponds to the 8 photodiodes' responses (from A to D and 1 to 4) to the applied pressure in each of the 41 points tested (16 pressure points and 25 intermediate pressure points). Seven pressure levels were studied, thus yielding seven different G-matrices, one for each pressure level: 0 mmHg, 15 mmHg, 32 mmHg, 47 mmHg, 63 mmHg, 78 mmHg, and 95 mmHg (Figure 3.5).

The implementation of the inverse model is based on the following mathematical equation:

$$R_i = |G_i^+ v_{in}| \tag{3.2}$$

where G_i^+ (41×8) represents the pseudoinverse of each G_i matrix (8×41) for the $i-th$ pressure level, and v_{in} contains the input data (8×1) as voltage readings from the photodiodes. This equation transforms the voltage readings into an estimation of the applied

pressure's location (R_i) with a dimension of 41×6, ensuring that only positive values are considered in the reconstructed pressure map.

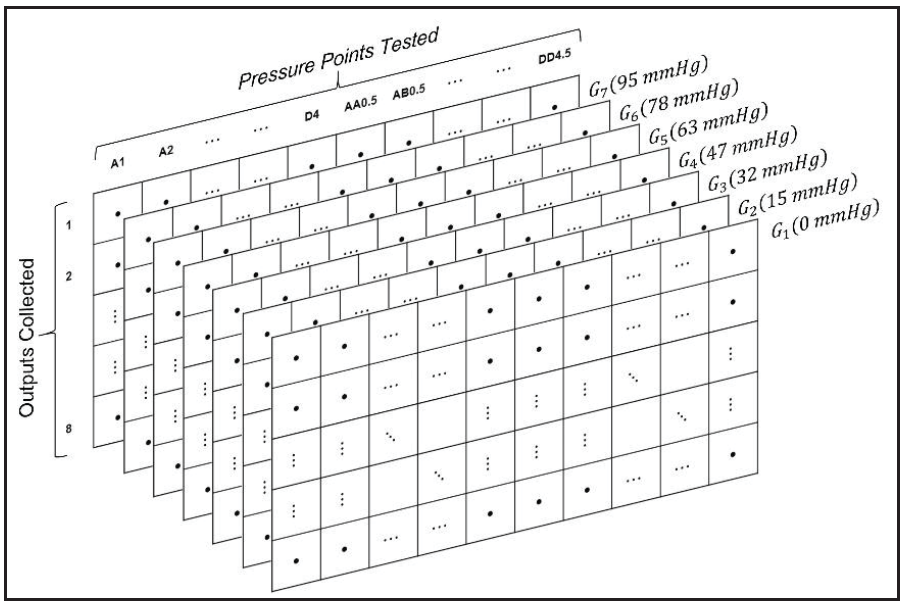

Figure 3.5 G-matrices structure of the tested pressure points and their corresponding collected outputs

It is worth noting that, although the classical Moore–Penrose pseudoinverse is sufficient for the current prototype, larger-scale systems typically require a regularized formulation to improve numerical stability. In such cases, the covariance of the sensor noise, estimated from measurements acquired without applied pressure, is incorporated into the matrix (GG^t) before inversion. This prevents noise amplification in high-dimensional systems. Since the objective of this work is to demonstrate feasibility using a reduced number of sensing points, the classical pseudoinverse provides adequate performance without requiring regularization.

The pressure localization process is divided into four stages:

1. Grid studied: As mentioned at the beginning of this paper, the flexible pressure pad measures 70 mm × 70 mm × 4 mm. This pad encapsulates in its interior a 4x4 grid of polyurethane optical fibers spaced by 10 mm between them. A total of 41 test points (PPs and IPs) were created with this configuration (Figure 3.1c).

2. Data: An input vector v_{in} is obtained, containing voltage readings from the 8 photodiodes in response to pressure applied at an unknown location. These readings exhibit a relationship with the applied pressure, where higher pressure results in lower voltage values.
3. Inverse Model Application: For each pressure level, the pseudoinverse G_i^+ is computed and applied using the inverse model formula, generating six response vectors R_i. The response for 0 mmHg is excluded, as it corresponds to the absence of applied pressure. Since the objective is to evaluate the performance of the sensor under active conditions, only the responses of the higher levels are considered for the analysis. The mathematical value of this matrix helped to define the reference value of the subsequent measurements. Each of the 6 response vectors consists of 41 elements, corresponding to the predefined study points.
4. Result Interpretation: The six response vectors are averaged (R_{mean}) to obtain a robust estimation of the pressure location. The maximum values in the resulting vector (41×1) indicate the zone most likely under pressure, leveraging the relationship between pressure and voltage to enhance localization accuracy.

The proposed implementation offers significant advantages. It provides robustness, as the use of multiple pressure levels and the averaging of their responses enhances the system's ability to handle variations in measurement conditions. It ensures generalization, as the model demonstrates the capability to interpolate between characterized measurement points, enabling pressure detection in intermediate zones. Finally, this practical approach delivers computational efficiency, allowing near-real-time processing of photodiode signals and facilitating dynamic localization of applied pressure.

Figure 3.6 shows the histogram of errors in the localization model, obtained from the 246 experimental measurements taken at the 41 test points of the sensor. Each bar represents the frequency of errors grouped into bins approximately 7 mm wide, a value that corresponds to the characteristic distances between adjacent points on the sensor, which are 10 mm apart. The

errors were calculated as the Euclidean distance between the applied pressure's actual position and the inverse model's estimate.

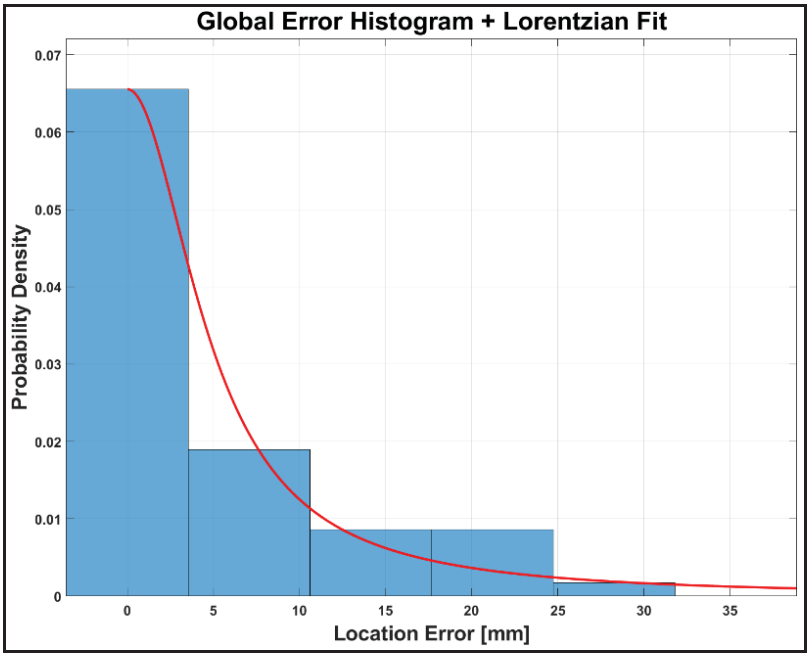

Figure 3.6 Histogram of localization errors (blue bars) with the corresponding Lorentzian fit (red curve)

For the statistical analysis of the localization system's accuracy, continuous errors were fitted using a Lorentzian distribution. This fitting, represented by the red curve in the figure, adequately models both: a high density of small errors (probability ≈ 0.065) concentrated near the origin, together with a less frequent but significant presence of larger errors, extending up to 30 mm. These atypical errors could be related to pressures applied at the edge points of the sensor, to areas of greater ambiguity, or to effects derived from the non-linearity of the inverse model.

To quantify the characteristic error distribution of the model, the gamma (γ) value of the fitted Lorentzian distribution was used, which for the localization model is ±4.86 mm. This parameter represents the half-width of the interval where approximately 50% of the most accurate measurements are concentrated. In other words, half of the inverse model's localization estimates have an error of less than ±4.86 mm with respect to the actual position

of the stimulus. Considering that the PPs are spaced 10 mm apart and are complemented by the 25 intermediate points, an error of this magnitude suggests that the inverse model is capable of estimating arbitrary positions within the continuous space on the surface of the pad, with a characteristic error below 5 mm.

The characteristic localization error of ±4.86 mm falls within the range of reported values for optical pressure sensors, typically on the order of several millimeters (∼6 mm) depending on the configuration (Kanellos et al., 2010; Shabalov et al., 2024), and remains competitive even when compared to learning-based approaches that achieve errors as low as ∼2 mm (Shabalov et al., 2024). In this sense, the present physically grounded inverse formulation offers robust localization performance while preserving model interpretability and avoiding the additional complexity associated with large training datasets.

Although the localization model shows strong performance, a complete reconstruction of the pressure profile requires both the generation of a spatial pressure map from the inverse model output and the calibration of a pressure estimation model to express these results in physical units (mmHg), as detailed in the following sections.

3.3.1.2 Spatial Pressure Map Builder

The averaged response vector derived from the inverse model is used to generate spatial pressure maps that represent the model's response across the 41 locations. These maps visualize the distribution of the applied pressure and help interpret the obtained results. As seen in Figure 3.7, the spatial maps reveal that the point with the highest response corresponds to the probable location where the force is applied. This behavior is consistent with the inverse model theory, in which the relationship between pressure and voltage allows for accurately identifying the region of highest impact. Additionally, the surrounding points exhibit lower response values, reflecting the dispersion of pressure in the adjacent areas. This pattern is expected, as in a physical system, whereby the applied force is not concentrated in a single

point but progressively distributed across neighboring regions. This behavior was consistently observed in all the studied zones, confirming the repeatability of the system's response.

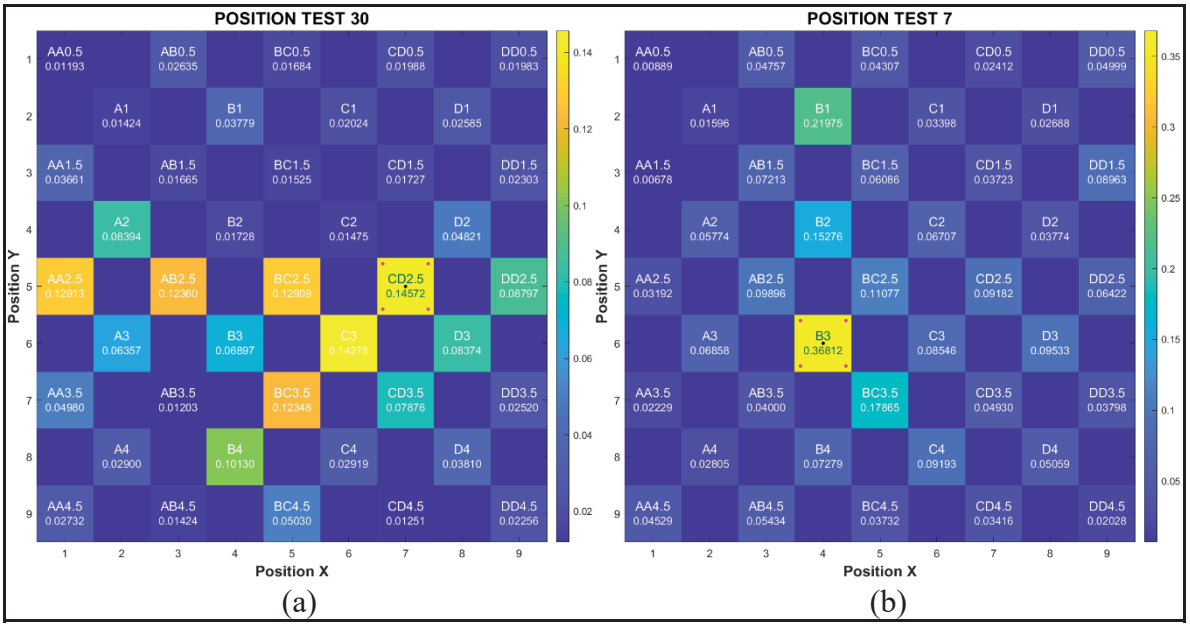

Figure 3.7 Pressure distribution maps generated from the inverse model response to the input vector. (a) Distribution map of intermediate point CD2.5 at 63 mmHg and (b) Distribution map of point B3 at 78 mmHg. The black dot marks the experimental point of pressure application. The magenta dots indicate the model's predicted maximum response. Color intensity reflects the model's response magnitude (arbitrary units), as shown by the color bar

The comparison between these generated maps for different pressure levels further validates the system's stability and effectiveness. This demonstrates that the model successfully adapts to different load conditions and provides results consistent with the magnitude of the applied pressure. Additionally, as the pressure increases, not only does the maximum response in the central zone rise, but the adjacent cells also reflect a proportional increase in their response. This suggests an effective interpolation process between the characterized points.

In the spatial maps, some grid cells appear without numerical values. These correspond to positions that were not measured during the characterization stage and thus do not yield a response for the reconstruction process. Since these points were not included in the characterization dataset, they are excluded from the analysis and are shown only for spatial

reference. Focusing on the relevant regions of the sensor guarantees consistent data interpretation. Overall, the obtained results highlight the inverse model's capability to accurately identify the pressure location and its propagation within the study area. The proper differentiation between high and low response zones, along with the consistency of the values obtained for different pressure levels, supports the system's effectiveness and its applicability in pressure location detection and spatial mapping for flexible optical sensors.

3.3.1.3 Calibration and Building of the Pressure Estimation Model

Once the point of maximum activation has been located by the inverse model, the next step is to estimate the pressure applied to that point. For this purpose, a method was implemented that takes advantage of the input vector corresponding to the detected point, using its spatial information provided by the inverse model to select the local pressure estimation model and thus calculate the magnitude of the detected event.

As previously mentioned, during the experimental characterization stage (Section 3.2.2), different known levels of pressure were applied on the sensitive pad, and the response signals acquired by the photodiodes were recorded by the DAQ. From these data, an individual pressure estimation model was developed for each testing point, using a linear fit of the form:

$$\bar{v}_{exp} = a_i \cdot P + b_i \tag{3.3}$$

where $\bar{v}_{exp}$ represents the mean value of the experimental input vector of the point i, P represents the pressure level applied during the tests, and a_i, b_i are the coefficients of the linear fit for each point i, derived from their experimental responses. This procedure is repeated for each of the 41 points tested, thus generating an independent linear estimation model for each point of the flexible optical sensor.

Subsequently, during the real estimation, once the index of the point of maximum activation is located from the vector of the inverse model R_{mean} of dimension 41×1, the estimation

model corresponding to that point is selected since each of the elements that compose it is associated with a spatial point of the sensor surface. Then, the pressure exerted on that point is estimated using the derived equation (Equation (3.4)) from the calibrated estimation model (Equation (3.3)):

$$\hat{P} = \frac{\bar{v}_{in} - b_i}{a_i} \tag{3.4}$$

where $\bar{v}_{in}$ represents the mean of the current input vector (i.e., of the signal coming at that instant from the photodiodes), a_i and b_i are the coefficients of the estimation model previously calculated for the localized point i, and $\hat{P}$ is the estimated maximum pressure at that point. This method allows for obtaining a point estimate of the pressure based exclusively on the system input, using previously calibrated models for each point.

To spatially represent the estimated magnitude of the stimulus in a consistent way, a proportional scaling of the R_{mean} vector is performed, ensuring that it preserves the relative distribution of the original vector and that its maximum value matches the estimated pressure while the values of the neighboring points reflect their relative activation (Equation (3.5)).

$$P_{sca} = \frac{R_{mean}}{R_{i^*}} \cdot \hat{P} \tag{3.5}$$

From the equation above, R_{mean} represents the inverse model response vector (41×1); $R_{i^*} = \max(R_{mean})$ is the maximum value of the vector at the located point i, $\hat{P}$ is the estimated maximum pressure at the point i, and P_{sca} is the scaled pressure vector (41×1), resulting from the proportional scaling performed. Therefore, in the end, a more realistic and continuous representation of the stimulus on the sensor surface is obtained.

The proposed approach allows for taking advantage of the accuracy of the spatial localization model, together with a pressure estimation model based on the specific response of each point. In addition, the proportional scaling of the output vector allows the spatial information

generated by the inverse model to be preserved, while its overall magnitude is adjusted to reflect the estimated stimulus intensity in pressure units of mmHg. Thus, a spatial representation consistent with the actual dynamics of the applied pressure is achieved (Figure 3.8).

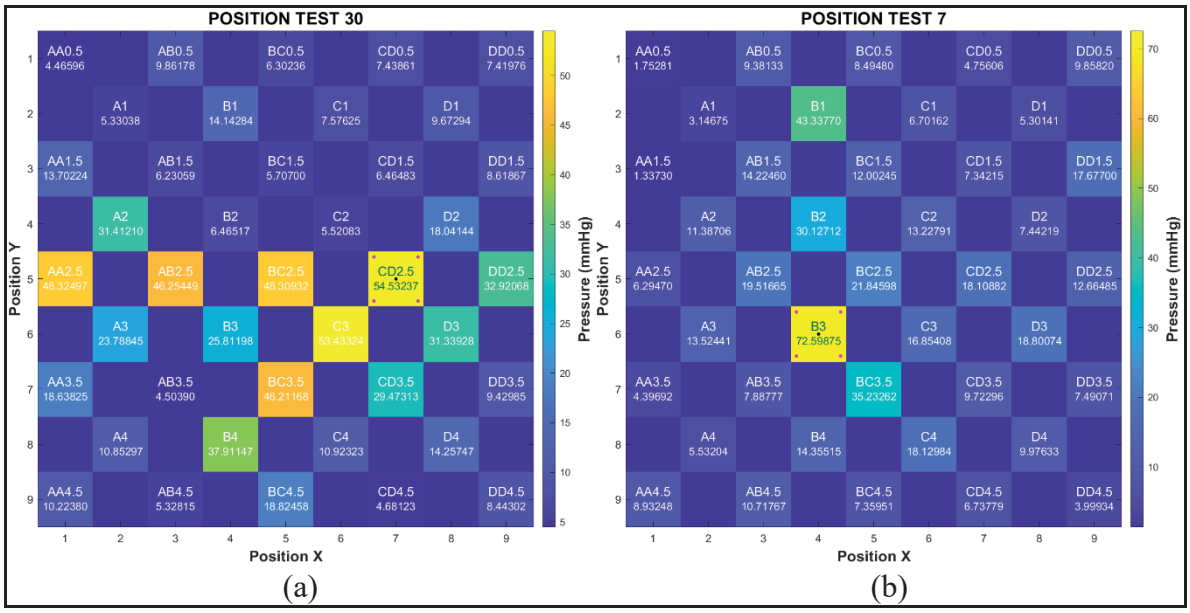

(a) (b)

Figure 3.8 Estimated pressure maps generated from the inverse model response to the input vector and the pressure estimation model. (a) Pressure map of intermediate point CD2.5 at 63 mmHg and (b) Pressure map of point B3 at 78 mmHg. The black dot marks the experimental point of pressure application. The magenta dots indicate the model's predicted maximum response. Color intensity reflects the model's response magnitude, as shown by the color bar

The pressure estimation model was evaluated on a total of 246 tests, corresponding to the six pressure levels studied, applied to the 41 pressure points of the sensor. The main indicator of model performance was the mean absolute error (MAE), which directly reflects the average error made in each estimation under real operating conditions. For this evaluation, the differences between the applied pressure and the pressure estimated by the system were calculated. The estimation scheme implemented was based on the characteristic equations calibrated individually for each of the 41 sensor points. This point-to-point strategy allowed for better preservation of local information and improved precision compared to general

models, where the maximum response values of the stimulated point were diluted by low responses from other points, thus diminishing the estimated coefficients.

The analysis was initially carried out on all test points. Subsequently, to better understand the impact of location precision on pressure estimation, the results were segmented into the two zones established in Section 3.2.2: internal (inner IPs and PPs) and edge (corner IPs and edge IPs). The overall MAE for the 41 points was 13.19 mmHg, based on a total of 246 cases. This value represents the average error of the system and establishes the starting point for evaluating its overall performance. When analyzing only the well-localized points, i.e., those in which the localization model (inverse model) correctly determined the position of the applied stimulus, the MAE dropped significantly to 5.21 mmHg, demonstrating the strong link between precise localization and estimation quality. In contrast, for mislocalized points, the MAE increased to 23.43 mmHg, confirming the negative impact of localization errors on pressure estimation. This trend persisted when analyzing the specific areas. In the internal zone, the overall MAE was 9.60 mmHg, but when considering only well-localized points, it decreased to 5.25 mmHg, while at mislocalized points, it increased to 19.26 mmHg. In the edge zone, the overall MAE reached 18.78 mmHg, with a clear difference between well-localized points (5.09 mmHg) and mislocalized points (26.36 mmHg). These results strengthen the hypothesis that high errors in pressure estimation are strongly associated with localization errors, especially in edge areas where the localization model faces greater ambiguity. Altogether, the findings demonstrate an operational interdependence between the localization and estimation systems: when the former fails, the performance of the latter is inevitably compromised.

The pressure estimation strategy implemented here, based on the inverse-model response, point-specific linear regressions, and proportional scaling, is consistent with data processing approaches commonly reported for optical pressure sensors, where pre-processing steps such as filtering, normalization, or curve fitting are typically combined with direct estimation models or, in some cases, learning-enhanced algorithms (Bi et al., 2023; Bijender et al., 2024; Chang et al., 2012; Katrenova et al., 2022; Wang et al., 2008). This point-based modeling approach yields a mean absolute error of 13.19 mmHg over all test cases, which improves to

about 5 mmHg when the stimulus is correctly localized, showing that reliable pressure estimation can be achieved without necessarily relying on large-scale training datasets or complex learning architectures (de Carvalho et al., 2025; Wang et al., 2008), which is particularly relevant for rapid prototyping and low-cost implementations.

In addition, it is important to consider other sources of error related to the estimation process itself. These include contributions from mathematical noise derived from the numerical transformations involved, such as the use of pseudo-inverses, input vector processing, or point-calibrated estimation models, among others. Such transformations can amplify small variations in the data, especially when combined with location errors or weak signals. Moreover, the need for 41 independent equations, one for each point, since the use of a general equation excessively flattened the response of the model and led to pressure underestimations due to non-representative averages.

Despite these limitations, the results obtained are encouraging and show that, when localization is correct, pressure estimation can achieve an average error close to 5 mmHg, which is very promising for medical or continuous monitoring applications. This suggests that by improving materials, reducing electronic noise, and optimizing localization and estimation algorithms, the system could achieve significantly more robust and reliable performance.

3.3.2 Pressure Sensor Performance Evaluation

To assess the overall performance of the proposed system, including both pressure localization and estimation, a series of quantitative metrics were applied. Among these, Receiver Operating Characteristic (ROC) curves were used for each of the six pressure levels (15, 32, 47, 63, 78, and 95 mmHg) to visualize the relationship between sensitivity (recall) and false positive rate (FPR) under different threshold values.

During the calibration stage, 100 threshold values were generated, evenly distributed between the minimum and maximum values of the R_{mean} vector (41×1). As mentioned before, this

vector corresponds to the mean response obtained from the inverse model for each input. By stacking all R_{mean} vectors from the tests, a 41×41 matrix was built, where each column represents a test case. Each element of this matrix was compared to every threshold generated to binarize the values: if the element exceeded the threshold, it was classified as a positive event, while lower elements were classified as negative. This process yielded a series of binary matrices representing different decision levels.

These binary matrices were then compared, column by column, with a 41×41 identity matrix used as the ideal reference, assuming that the pressure was applied at only one point in each specific test case. This comparison allows the calculation of true positives (TP), true negatives (TN), false positives (FP), and false negatives (FN). Among all thresholds, the one that maximizes the sensitivity while minimizing the false positive rate was considered as the optimal threshold. This corresponded to the point on the ROC curve closest to the upper left corner (recall = 1, FPR = 0). The optimal thresholds for each pressure level were then stored for use during real-time operation, where, once the pressure is estimated, the corresponding threshold is retrieved and used to binarize the spatial pressure map. This enables accurate isolation and identification of the point under pressure based on the estimated pressure (Figure 3.9).

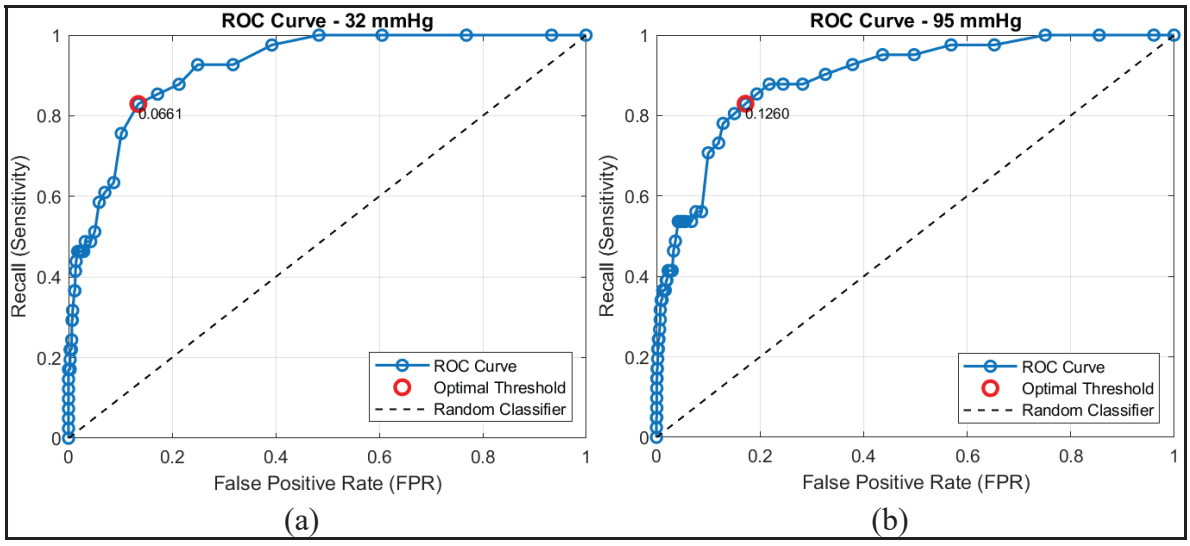

Figure 3.9 ROC curves to visualize the performance of the inverse model. (a) Model performance curve at 32 mmHg; (b) Model performance curve at 95 mmHg

The ROC curves obtained, such as those shown in Figure 3.9, exhibit a pronounced convex shape, indicating strong discriminative performance throughout all pressure levels evaluated. The clear curvature toward the upper left corner shows the model's ability to achieve a high sensitivity while maintaining a low false positive rate. Notably, the curves present a considerable separation from the diagonal reference of a random classifier, confirming the model's predictive capacity at every pressure level.

At lower pressures (15–32 mmHg), the model demonstrates high sensitivity even at low threshold values, achieving excellent recall with minimal false positives, suggesting effective detection under weak stimuli. At intermediate pressures (47–78 mmHg), the curves keep their convexity towards the upper left corner, although a slight rightward expansion is observed, indicating a small increase in false positives. However, sensitivity remains high, and the model's detection performance is still reliable. At the highest pressure (95 mmHg), there is a subtle change in curvature, with a slight decrease in sensitivity. This may suggest that, at higher pressures, the model becomes more stringent and tends to eliminate more false positives.

When comparing the curves across levels, it is observed that the system's performance is consistent, displaying a robust and coherent behavior throughout the full pressure range. In addition, the threshold selection method ensures a balanced ratio between detection and discrimination, reflecting the expected scaling of the system's output in response to higher stimulus intensity.

To complement the ROC analysis and further enhance the evaluation of the system's performance, additional metrics were calculated based on the previously determined optimal thresholds. These thresholds were applied to binarize the spatial pressure maps derived from R_{mean} elements, allowing the identification of the areas of highest-pressure response. The resulting performance metrics, sensitivity (recall), specificity, and precision, provide a more comprehensive evaluation of the system's detection capabilities (Table 3.1).

In general, a high recall is critical for our system, since it ensures the detection of pressure on the sensor pad, even at the cost of accepting some false positives. Specificity measures the system's ability to reject false positives, i.e., the ratio of correctly identified true negatives, while precision represents how many of the positive detections actually correspond to true events, thus serving to indicate the system's reliability in positive detection.

Table 3.1 Metrics Evaluation

Pressure Level (mmHg)	Optimal Threshold	Recall	Specificity	Precision	Comments
15	~0.0440	90.24%	82.44%	11.38%	Good specificity and sensitivity; however, false positives reduce precision.
32	~0.0661	82.93%	86.52%	13.33%	Good overall balance, with a small drop in sensitivity but an improvement in specificity and precision.
47	~0.0743	85.37%	83.84%	11.67%	Recall remains stable, with a slight decrease in specificity and precision compared to 32 mmHg.
63	~0.0919	82.93%	85.06%	12.19%	Recall is stable, while specificity and precision show small improvements.
78	~0.1015	85.37%	83.17%	11.25%	Recall increases slightly, while specificity and precision show modest decreases.
95	~0.1260	82.93	82.80%	10.76%	Slight overall decrease in all metrics, with a balanced sensitivity and specificity, while low precision suggests the presence of false positives.

The metrics indicate a consistent performance across pressure levels, with recall values ranging from 82.93% to 90.24% between 15 and 78 mmHg. This steadily high sensitivity demonstrates that the system effectively detects the presence of applied pressure, even under low-intensity

pressure. Such behavior is particularly valuable in applications where missing an event could compromise timely and appropriate decision-making with very serious consequences.

However, this high recall is accompanied by relatively low precision values (10.76–13.33%), suggesting the presence of false positives. Given the physical nature of the system, it is expected that when pressure is applied at some point on the pad, the areas around the impactor are affected by slight deformations, especially in a soft material like PDMS. This spatial dispersion may lead adjacent points to produce similar voltage responses, causing the system to interpret them as additional positive events. From a functional point of view, this is not completely detrimental; if the false positives are spatially close to the true activation point, they could be exploited to estimate their location through triangulation methods. Therefore, low precision does not necessarily imply poor performance, but rather reflects the physical interaction dynamics between the sensor and the pressure.

On the other hand, the ability of the system to correctly identify negative events (specificity) shows a slight improvement with increasing pressure, ranging from 82.44% to 86.52%. This suggests that, at higher pressures, the system is more effectively ignoring unresponsive regions, possibly because the associated voltage changes become more pronounced, improving the signal-to-noise ratio. This is evident at 95 mmHg, where the system keeps a balanced profile, with recall at 82.93%, specificity at 82.80%, and precision at 10.76%, which implies that despite a slight decline in sensitivity and precision at this highest pressure, the system continues to effectively distinguish positive and negative events, likely due to stronger signal responses that reduce the number of false positives without significantly compromising the detection performance.

Figure 3.10 shows two examples of binarized pressure maps corresponding to pressure levels of 32 mmHg (a) and 95 mmHg (b). In both cases, only the values above the calculated optimal thresholds were preserved, while those below were set to zero. The yellow box highlights the point with the highest value in each test, indicating the most likely location of the applied pressure. In Figure 3.10a, the peak is surrounded by other activated positions (orange or green

boxes), mainly concentrated in the area adjacent to the application zone. This pattern suggests that some false positives might result from the physical dispersion of the pressure across the sensor pad, since the applied forces can slightly deform the neighboring regions. Importantly, these nearby activations could be exploited to improve the spatial localization.

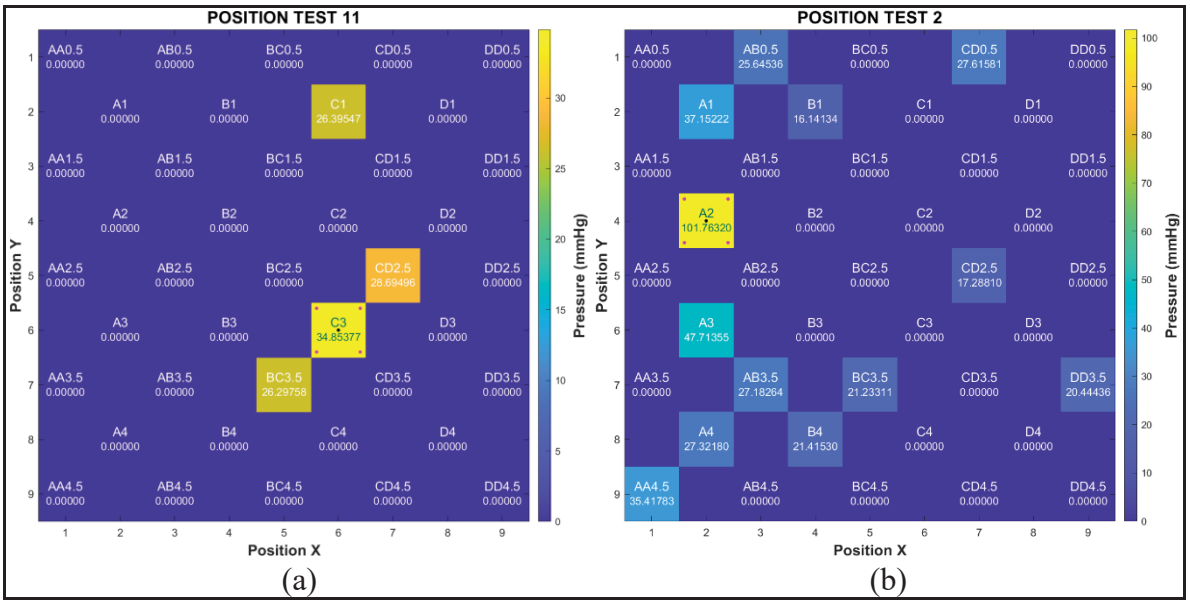

Figure 3.10 Binarized pressure maps generated with the optimal thresholds calculated and applied to R_{mean}. (a) Binarized pressure map of pressure point C3 at 32 mmHg and (b) Binarized pressure of pressure point A2 at 95 mmHg. The black dot marks the experimental point of pressure application. The magenta dots indicate the model's predicted maximum response. Color intensity reflects the model's response magnitude, as shown by the color bar

In contrast, Figure 3.10b presents a scenario where the maximum pressure point appears more isolated, with surrounding activations of significantly lower magnitude. In this case, while some distant responses can be attributed to system noise, nearby points such as A1 and A3 could still provide valuable spatial information to enhance localization accuracy. These two examples illustrate different but valid outcomes of the pressure reconstruction process, in which the system successfully identifies the maximum pressure point despite varying levels of peripheral activity. Particularly, occasional distant activations could also be caused by mechanical or electronic noise, as their locations have no clear physical relationship with the estimated pressure point.

To contextualize these results, the current prototype consists of a 4 × 4 grid of PU-OFs spaced 10 mm apart and embedded in a PDMS pad of 70 mm × 70 mm × 4 mm, establishing a total of 41 measurement points. The performance evaluation presented here was carried out with the sensor pad laid in a flat configuration on a rigid support, under static loading conditions in a controlled laboratory setting, with stabilization periods at each pressure level to ensure steady-state measurements. Under these conditions, this configuration has shown good performance in locating the stimulus (characteristic localization error of ±4.86 mm) and in estimating pressure when the location is correct (MAE of 5.21 mmHg) over the studied range of 0–95 mmHg. These results are encouraging and confirm the feasibility of the proposed approach, providing a solid basis for subsequent versions of the system. However, the current implementation still relies on an external multichannel acquisition system, computer-based processing, and externally powered electronics, so its use is, for now, limited to controlled environments and experimental studies of pressure distribution on relatively small areas. For this reason, dynamic characteristics such as response time, recovery behavior, or frequency-dependent effects were not characterized in this study and left for future investigation, along with the systematic assessments under time-varying pressures and on bent or curved deformable surfaces.

From a design point of view, both the fiber grid architecture and the inverse model used are conceptually scalable to configurations with a larger number of fibers and measurement points. However, practical scalability is limited by several factors identified during the development of the system: the optical attenuation of the current fibers and the total length restrict the physical size of the square pad to around half a meter; and the point-by-point pressure estimation strategy, which is manageable with 41 points, is one of the main scalability bottlenecks in the current implementation, since the experimental calibration and model management effort scales linearly with the number of measurement points. On the computational side, the inverse reconstruction relies on well-established numerical linear algebra and can be extended to larger grids using efficient implementations and appropriate regularization. Scaling to larger or higher resolution matrices would therefore require fibers with improved optical properties, more controlled or industrialized fabrication processes,

acquisition electronics adapted to a larger number of channels or to multiplexing schemes, all of which can realistically be achieved with modern technologies.

Although the current prototype still presents some practical challenges, the intrinsic characteristics of the system, the flexibility of the pad, its ability to generate two-dimensional pressure maps, and the use of low-cost components, are consistent with potential use scenarios where it is important to characterize pressure distribution over relatively small, soft, non-flat contact surfaces, for example in the development of flexible pressure-sensing pads (e.g., for pressure injury prevention) or tactile user interfaces, the instrumentation of soft robotic elements, or experimental platforms to study load patterns on deformable surfaces.

Overall, these results demonstrate the robustness and adaptability of the proposed system. The combined application of the inverse model, the pressure estimation model, and the optimal threshold binarization approach facilitates an effective reconstruction of applied pressure events across diverse pressure patterns. The system achieves a strong balance between sensitivity and false positives, confirming its reliability in a range of scenarios involving physical interaction with the sensor.

3.4 Conclusion

The results obtained in this work demonstrate that the integration of an inverse model based on pseudoinverses with a flexible optical pressure sensor enables the reliable reconstruction of applied pressure events on a 2D sensing matrix. The system achieves a high sensitivity across multiple pressure levels, combined with acceptable specificity and a localization error below 5 mm in most cases. Even though the precision is affected by the large deformation of the soft elastomeric and conformable materials, the presence of multiple fiber-sensing point activations may be functionally exploited to enhance localization accuracy through interpolation or triangulation techniques.

Through the pre-calibration of the inverse model output with a point-specific pressure estimation model, the proposed system not only identifies the location of a pressure stimulus but also estimates its magnitude with promising accuracy and real-time speed. The use of proportional scaling further allows for the construction of realistic and spatially consistent 2D pressure maps. This approach results in a system that is not only responsive and repeatable, but also computationally efficient and adaptable to other fiber-optic-based sensing platforms.

The work is another step towards scalable and conformable sensing materials and methods, and flexible optical sensing technologies.

Author Contributions: Conceptualization and design of experiments, A.A.R., K.N.A., J.-M.L. and B.U.; methodology and conduct of experiments, A.A.R., K.N.A. and D.S.; modeling and interpretation of results, A.A.R., J.-M.L. and B.U.; writing—original draft preparation, A.A.R.; writing—review and editing, A.A.R., K.N.A., J.-M.L. and B.U.; supervision, J.-M.L. and B.U.; funding acquisition, B.U. All authors have read and agreed to the published version of the manuscript.

CHAPTER 4

FUTURE RESEARCH OPPORTUNITIES

Flexible pressure sensors are essential in applications that require adaptation to non-flat or irregular surfaces. Sensors based on soft materials offer remarkable design flexibility, maintaining their ability to bend, stretch, and conform to complex geometries without compromising their sensing functionality (Y. Guo et al., 2024; H. Li et al., 2025; Sabri et al., 2015; Tan et al., 2022; D. Xu et al., 2025; Yang et al., 2022). Optical fiber-based technologies offer an advantageous alternative, as they are intrinsically immune to electromagnetic interference and capable of multi-point or long-distance monitoring. These features make them suitable for applications such as structural health monitoring, advanced robotics, and wearable biomedical diagnostics (Kanellos et al., 2010; Lopez-Higuera et al., 2011; Meng et al., 2022; Min et al., 2022; Yassin et al., 2024).

Despite these advantages, achieving both high sensitivity and a wide sensing range remains a significant challenge. The overall performance of flexible sensors is strongly influenced by the sensing principle employed and the quality of their integration into soft substrates (Al-Mai et al., 2017; Capp et al., 2025; Funnell & Thomas, 2023; Yao et al., 2025). Among the sensing techniques, intensity-based detection via bending loss is one of the most widely adopted due to its simplicity and compatibility with flexible configurations. In this method, an external force deforms the fiber, causing light leakage that results in measurable intensity changes because of the mechanical interaction (Chao-Shih et al., 2007; Gan et al., 2024; Homayounfar & Andrew, 2020; Roriz et al., 2013; Wang et al., 2008).

This sensing principle allows the generation of spatial response patterns that can be interpreted to estimate both the location and magnitude of the applied pressure. These patterns serve as the basis for constructing pressure maps, which may be analyzed using either direct physics-based models or more complex data-driven approaches, depending on the system's design and

target application (de Carvalho et al., 2025; Katrenova et al., 2022; Meng et al., 2024; Wang et al., 2005; Hao Zhang et al., 2024).

Within this context, the present chapter examines the experimental performance of the developed sensor system. The discussion is structured into three sections: (1) the achieved contributions and capabilities of the system, (2) the technical limitations encountered during development, and (3) potential improvements and directions for future innovation.

4.1 Scope and Contributions of the System

The development of the optoelectronic pressure sensor went through two key experimental stages, each with specific objectives and progressive advances. The first stage consisted of implementing simple prototypes with 1×1 and 2×2 configurations of PMMA POFs embedded in PDMS, and the second stage culminated in the manufacture of a more complex configuration with a 4×4 configuration of PU-OFs and the integration of an inverse model for spatial localization and pressure estimation.

In the first stage, the main objective was to validate the operating principle of the sensor under optical intensity modulation (fiber bending loss) induced by applied pressure. Despite the straightforward configurations, the results showed nonlinear response curves, consistent sensitivity at pressures above 998 mmHg (133 kPa), and good repeatability under controlled conditions, even when using a low-cost electronic system. This stage allowed us to establish a solid proof of concept and demonstrated that inexpensive optoelectronic components were capable of measuring pressure changes, especially in high-load tests. In addition, analysis of the curves allowed us to segment the response into low- and high-pressure zones, facilitating their subsequent characterization.

This segmentation approach proved valuable not only for our sensor but also aligns with strategies observed in other bend-loss-based systems, which have demonstrated reliable detection in the high-pressure range but often struggle at lower intensities. For instance, a

microfabricated PDMS-based waveguide sensor reported a 39% change in optical intensity under 0.28 N (equivalent to 500 kPa) over a 2×2 mm² area (Wang et al., 2008), while other designs remained functional up to 1000 kPa (Soetanto et al., 2011). However, several studies highlight limitations in the low-pressure regime, where signal ambiguity or mechanical damping effects affect accuracy (Amouzou et al., 2025; Jeroen et al., 2010; Soetanto et al., 2011). These challenges reinforce the relevance of our decision to segment the pressure response range early in the design process, enabling more targeted calibration and interpretation.

The second stage marked a significant evolution in terms of design, spatial resolution, and signal processing. A flexible pad was fabricated with polyurethane fibers arranged in a 4×4 grid, resulting in a total of 41 measurement points between pressure points (PPs) and intermediate points (IPs). This design increased the spatial resolution of the system, expanding its ability to detect pressure events distributed across the entire sensor area. A multichannel acquisition system DAQ and an inverse model based on the Moore-Penrose pseudoinverse were incorporated, allowing the reconstruction of spatial pressure maps with good agreement between the applied load and the obtained response. The 10 mm spatial resolution places the system within the range reported for other optical fiber-based sensors, such as FBG systems with typical longitudinal spacings between 5 and 10 mm (Kanellos et al., 2010; Katrenova et al., 2022; Shabalov et al., 2024; Zhang et al., 2019), or bend-loss sensors with resolutions of 2 mm (Wang et al., 2008), 5 mm (Chao-Shih et al., 2007; Soetanto et al., 2011), 1 cm (Wang et al., 2005), and even 2 cm (Chang et al., 2012). While Optical Frequency Domain Reflectometry (OFDR) based configurations can theoretically achieve sub-millimeter precision (Katrenova et al., 2022), they require more complex and costly equipment, making our low-cost implementation a competitive alternative.

The accuracy of the localization model was evaluated by fitting a Lorentz distribution to the error data, resulting in a characteristic localization error of ±4.86 mm. This value suggests that the model is capable of estimating arbitrary positions on the grid with a fiber separation of 10 mm. Localization accuracy in optical pressure sensors has been shown to vary depending on

the signal processing approach. Without machine learning (ML), FBG-based systems report localization errors above 6 mm (Kanellos et al., 2010; Shabalov et al., 2024), while some bend-loss sensors operating without ML can reconstruct 2D pressure maps but typically struggle with multiple loads or precise magnitude estimation (Chang et al., 2012; Wang et al., 2008; Wang et al., 2005). In contrast, ML-enhanced models such as k-Nearest Neighbors (k-NN) or convolutional neural networks (CNN) have reported significant improvements, with localization MAEs as low as 2.1 mm (Shabalov et al., 2024) and classification or spatial accuracy exceeding 90% across predefined regions (de Carvalho et al., 2025; Wang et al., 2008). Despite not relying on advanced learning algorithms, the system developed achieved a comparable level of accuracy using only inverse model reconstruction, thus highlighting the effectiveness and methodological efficiency of the implemented approach, and reinforcing its potential for scalable integration in future versions.

Based on this location estimate, an individual pressure estimation model was implemented for each point using calibrated linear regressions, which significantly improved the estimated accuracy when the location was correct (MAE ≈ 5 mmHg). In addition, a proportional scaling system was incorporated for the pressure map, and the system's capabilities were evaluated using ROC curves and metrics such as sensitivity, specificity, and accuracy. The results showed robust and consistent performance across different pressure levels, validating the integration of the physical system with the implemented mathematical models. This strategy, starting from physical modeling and linear regression, is consistent with common approaches reported in the literature, where pressure reconstruction typically involves pre-processing steps such as filtering, normalization, or curve fitting before applying direct estimation models or machine learning (Bi et al., 2023; Bijender et al., 2024; Chang et al., 2012; Katrenova et al., 2022; Wang et al., 2008). However, while neural networks and convolutional architectures have demonstrated higher precision in classification or regression tasks (de Carvalho et al., 2025; Wang et al., 2008), they usually require extensive training datasets and can compromise system transparency. The choice to prioritize a physical point-based model approach, balanced interpretability, and efficiency enables reliable pressure estimation without depending on large-scale training datasets.

Another key aspect of the achievements was the validation of the low-cost electronics developed in the first phase, which were successfully reused in the second sample (4×4 PO-PUs). This result demonstrated their versatility and adaptability to different optical configurations. The printed circuit boards operated correctly in both configurations, showing that the electronic design is robust and scalable. The circuit has a wide spectral response range thanks to the photodiode used, which allows it to work with different light sources (white or colored), adding flexibility to the overall design. Rather than limiting future developments, these electronics can be reused, adapted, or scaled into new sensor designs without major modifications. This reusability contrasts with many systems reported in the literature, where electronic components are often tightly integrated or custom-fitted, limiting flexibility and increasing implementation complexity. In addition, instability in some configurations has been linked to weak coupling between fibers and/or waveguides, or to alignment errors introduced during manual assembly (Meng et al., 2022; Wang et al., 2008; Wang et al., 2005). In our design, the use of standardized optical connectors (ST/SMA) ensures secure fiber fixation and accurate alignment, helping to mitigate displacement and decoupling issues. Therefore, the implemented electronics offer a stable and practical foundation for future integration into more complex sensor architectures, offering both robustness and adaptability without adding unnecessary constraints or compromising functionality.

From a practical implementation perspective, the results obtained in this work demonstrate the technical feasibility of the sensing principle and the associated signal processing framework; however, the current system remains at a laboratory proof-of-concept stage. While the developed prototypes successfully validate spatial localization and pressure estimation under controlled conditions, specifically through inverse-model-based reconstruction and point-wise pressure estimation, their use in everyday applications, such as healthcare monitoring, wearable devices, or soft robotics, would require additional system-level considerations that go beyond sensing performance alone. These considerations are primarily associated with system integration and overall engineering constraints, which are characteristic of early-stage experimental prototypes and are not intrinsic challenges of the underlying sensing principle,

thereby defining the present experimental results as a further step toward more integrated implementations.

In its current configuration, the system relies on external laboratory equipment, including a multi-channel data acquisition unit, computer-based processing, and externally powered electronic circuits, as described in the experimental setup and characterization procedures detailed in Chapters 2 and 3. From this perspective, moving toward a self-contained implementation would imply integrating the custom optoelectronics into a more compact and energy-efficient embedded architecture, eliminating the dependence on external power supplies. Likewise, the signal processing algorithms, currently executed offline, would need to be adapted to an embedded or firmware-level implementation to enable real-time operation. Taken together, the reuse and scalability of the electronics and signal processing framework validated across multiple prototypes indicate that the current system provides a solid basis for future system-level development.

Additionally, practical use outside the laboratory would impose constraints related to mechanical robustness, repeatability, and ease of use, which become more important when the system is used under less controlled conditions. While the present study focused on controlled and repeatable loading conditions to evaluate sensing performance, the characterization results suggest that aspects such as optical coupling stability, encapsulation, and material selection will play a key role in future system-level refinements. Such improvements would be needed to support prolonged operation and repeated loading cycles in less controlled environments. In this context, the contributions presented in this chapter establish a technically sound and experimentally validated baseline upon which a portable, application-oriented pressure-sensing device could be developed through targeted engineering optimizations.

Although the results obtained are promising, several limitations were also identified during the development and testing phases, which are discussed in the following section.

4.2 Technical Limitations Identified

Throughout the whole development process, several technical limitations were identified, both in the physical design of the sensor and in the models used for signal reconstruction and interpretation.

In the first prototypes with POFs, one of the most significant issues was the low sensitivity in low-pressure areas, particularly when using the low-cost electronics. This reduced sensitivity was associated with several factors: the high optical coupling losses observed (>30 dB), the thickness of the PDMS encapsulation, the very low current generated in the photodiodes (∼1.4 μA), and the need to operate the transimpedance amplifiers at extremely high gains, sometimes near their limits. In addition, the mechanical rigidity of PMMA in POFs limited their deformation under load, producing only small bending-loss variations and making it difficult to detect the voltage changes. This combination significantly reduced the overall sensitivity of the system under low loads. In fact, the system could not reliably detect changes in light intensity below 998 mmHg (∼133 kPa), indicating a minimum pressure threshold required to cause an optical response (see Section 2.3).

As a direct consequence, it was decided to seek more flexible alternatives, such as polyurethane fibers, whose elastic behavior improved the interaction between pressure and optical loss. This change proved effective in the second prototype, where the system demonstrated high sensitivity even at 15 mmHg (∼2.0 kPa), with recall values above 90% (see Table 3.1), suggesting that the limitations observed in the earlier version were substantially reduced. These observations align with findings reported in the literature, where several flexible optical sensors showed ambiguous or noisy outputs at low pressure levels, with thresholds ranging from 4.8 to 19.09 kPa (Amouzou et al., 2025; Soetanto et al., 2011), and in some cases, no measurable signal was observed below 70 kPa (Jeroen et al., 2010). This loss of sensitivity has been commonly attributed to the viscoelastic response of soft polymer substrates, which introduces effects such as hysteresis, creeping, and signal oscillations (Alonso Romero et al.,

2023; Kanellos et al., 2010; Soetanto et al., 2011; Wang et al., 2005), or to mechanical constraints like tight winding or excessive bending of the optical fibers (Y. Guo et al., 2024).

Another physical limitation identified was the thickness of the encapsulation in the first prototypes. The height of the PDMS pad made it difficult to effectively compress the fibers, especially under low pressures, which reduced the overall sensitivity of the sensor. In the second version with PU fibers, this limitation was addressed by redesigning the encapsulation and using a precision acrylic mold, which improved the placement of the fibers and ensured a height that favored the deformation of the material over the fibers, thus increasing their bending. In addition, the flexibility and elastic recovery of the PU also contributed to a better mechanical response of the system, complementing the sensitivity improvements previously described. This design evolution is aligned with prior studies showing that badly controlled encapsulation thickness or weak mechanical bonding between fibers and substrates can lead to signal dispersion, differential loading/unloading behavior, and non-local responses (Katrenova et al., 2022; Wang et al., 2005). On the other hand, well-designed embedding geometries have been associated with improved spatial accuracy and reduced ambiguity in optical responses (H. Li et al., 2025; Wang et al., 2008), supporting the effectiveness of the strategies applied in the second prototype.

However, these structural improvements also introduced new complexities. Among them, the ambiguous response observed at intermediate points stands out, where multiple fibers can be simultaneously or partially activated due to PDMS deformation and/or mechanical coupling. This overlapping of signals introduced uncertainty in the location estimated by the model, particularly near the edges, where the inverse model exhibited greater sensitivity to localization errors. As a result, the pressure estimation error increased in mislocalized events, with the MAE rising from ∼5 mmHg to over 23 mmHg in some cases (see Section 3.3.1.3). Overall, the system's accuracy remained relatively low (10% – 13%), possibly due to pressure dispersion caused by PDMS deformation, which led to multiple fiber activations around the actual pressure point. Although these redundant signals may be functionally useful, they make it difficult the strictly identification of the precise stimulated point.

This kind of crosstalk and activation overlap is widely documented in other soft sensor systems. For example, one optical sensor exhibited 58% signal crosstalk when several surrounding points were activated under load, while a structural redesign reduced this to 7.8% (H. Li et al., 2025). Also, in materials like polymers, their inherent optical attenuation can create losses of up to 90% regardless of the pressure applied, which can amplify overlap issues by reducing the contrast between signals (Kanellos et al., 2010; Wang et al., 2008; Zhang et al., 2019). Similarly, PDMS-based systems have shown that when the fibers aren't properly bonded to the substrate, the strain caused by pressure can travel along the fiber and activate other points away from the impact zone (Katrenova et al., 2022). This becomes problematic in zones without rigid fixation, such as the edges, where pressure propagation is uneven and increases the chances of mislocalization. Some redesigns to reduce these responses include introducing physical spacing between fibers (Wang et al., 2008), although this can limit resolution. However, achieving a better balance between spatial density and signal clarity could open the door to new designs that reduce crosstalk without compromising resolution.

Additionally, experimental limitations were identified during the characterization process. Due to the absence of a mobile platform or system that would allow the force gauge to be moved over the sample, while the sample, together with the lighting system, measurement equipment, and acquisition equipment, remained fixed and aligned, it was necessary to manually reposition these components for each test point. This procedure, although performed with care, could introduce small misalignments or lighting variations due to optical decoupling between measurements, affecting the homogeneity and repeatability of the data obtained. These kinds of experimental limitations, while not always explicitly reported, have been indirectly acknowledged in several studies. For example, inconsistencies in sensor outputs have been associated with manual repositioning of components or a lack of mechanical stability in coupling interfaces (Al-Mai et al., 2017; Chen et al., 2023; Meng et al., 2022; Wang et al., 2008; Wang et al., 2005). Manual insertion of fibers into input/output couplers and manually cutting grooves have also been linked to variations in sensitivity or sensor drift during loading (Capp et al., 2025; Katrenova et al., 2022; Wang et al., 2008; Wang et al., 2005).

To address this, various authors have proposed or implemented controlled measurement platforms, such as universal testing machines for controlled loading (Mao et al., 2024), high-precision motorized Z-stages for pressure application (Schwartz et al., 2013), modified 3D printers for programmable displacements (Shabalov et al., 2024), and three-axis displacement stages (Tang et al., 2024). These setups help maintain consistent alignment and reduce measurement variability, which is crucial when characterizing flexible sensors embedded in soft substrates. Although the system proved to be functional despite these restrictions, our experience aligns with this trend, and the future implementation of a measuring station, either automated or equipped with controlled manual displacement mechanisms, is expected to enhance the repeatability of results and improve the reliability of calibration procedures.

On the other hand, the use of 41 individual estimation models increases computational and calibration complexity, which could make the practical or commercial implementation of the system difficult. Likewise, some points on the resulting pressure map were left uncharacterized in the 4×4 sample and appeared without values in the generated graphs. Although this did not represent a technical failure of the system, it does limit the resolution of the model. This type of point-by-point calibration has been reported as a recurring challenge in flexible sensors, where variability between sensing elements or manual alignment steps leads to inconsistent outputs (Wang et al., 2008; Wang et al., 2005). To overcome these issues, some authors have proposed the use of neural networks not only as prediction engines but also as tools for global calibration, eliminating the need to manually adjust or align each sensing element (Shabalov et al., 2024; Wang et al., 2023; Wang et al., 2008).

In our case, the decision to use per-point linear regressions was based on a more traditional approach to sensor characterization, guided by physical principles and reinforced through extensive experimental validation. Despite the increased number of individual models, this strategy offered high interpretability and robust local accuracy. Nevertheless, the challenge of ensuring scalability and efficiency across larger sensor arrays remains a key consideration, especially if the number of sensing points increases significantly.

Finally, the system was tested only under static and controlled conditions, so its behavior under dynamic scenarios, or with multiple simultaneous loads, has not yet been evaluated. While some systems based on direct physical mappings can localize single loads or sequential activations, they often struggle with multiple simultaneous pressures or with providing reliable quantitative estimations (Chang et al., 2012; Wang et al., 2008; Wang et al., 2005). In contrast, systems based on neural networks have shown that it is possible to separate overlapping signals and improve spatial resolution and classification accuracy in soft sensors (de Carvalho et al., 2025; Kumar et al., 2025; Shabalov et al., 2024; Wen et al., 2021).

While our current system relies on an architecture based on an inverse model and a set of point-by-point linear estimators that have already demonstrated robust performance in localization and pressure estimation under controlled conditions, its ability to scale efficiently to larger and more complex configurations will likely require the integration of such techniques in future updates.

Beyond the technical challenges discussed above, several constraints become particularly critical when considering the use of the current system outside the laboratory, where this type of sensor could be useful in areas such as healthcare monitoring or wearable devices. A primary constraint arises from the strong dependence on laboratory equipment for signal acquisition and processing. As demonstrated throughout the experimental evaluation, the use of an external DAQ system, computer-based processing, and electronic boards powered by external supplies restricts portability and prevents continuous or long-term operation under less controlled conditions. While these elements were well-suited and much needed for experimental validation, they represent a practical constraint for using the system in applications where a compact, self-contained, and easy-to-use device would be required.

Another key constraint for practical implementation concerns the robustness and repeatability of the system under non-ideal conditions. Under controlled laboratory conditions, optical coupling, alignment, and loading were carefully controlled; however, experimental results also revealed sensitivity to optical attenuation, mechanical crosstalk, and encapsulation properties,

particularly near intermediate points and sensor edges. In practical use, small variations in how the pad is positioned on the contact surface, gradual deformation of the encapsulation under sustained loading, and repeated loading cycles could increase these effects, potentially worsening signal stability, causing baseline shifts, and making regular recalibration necessary. These factors highlight the need for further evaluation of long-term stability, durability under prolonged use, and strategies to mitigate performance degradation during extended operation.

Finally, the current system architecture has been designed to favor measurement accuracy and physical interpretability over practical usability. While this approach proved effective for experimental characterization, particularly through the use of multiple point-specific estimation models, it increases system complexity in terms of calibration effort and computational management. In practical environments, such complexity may make the system harder to use and scale, especially for non-specialized users or larger sensor arrays. Therefore, the constraints identified in this work are not limited to sensing performance but also stem from the chosen per-point estimation architecture and its calibration requirements, which translate into system-level engineering issues that must be addressed before transitioning from a proof-of-concept prototype to a functional and user-oriented device.

4.3 Proposals for Improvement and Future Work

In future practical implementations, development of the proposed pressure sensing system should focus on addressing the integration challenges at the system level identified in the previous section. While the experimental results demonstrate reliable localization and pressure estimation under controlled conditions, moving toward applications such as healthcare monitoring, wearable sensing, soft robotics, or industrial sensing would require transforming the current laboratory-based architecture into a compact, battery-powered, and user-oriented device. Achieving this will require advances in electronic integration, power management, embedded signal processing implementation, and mechanical robustness, rather than changing the underlying sensing principle.

A critical step in moving from the current proof-of-concept setup to practical use is the replacement of external laboratory equipment with an integrated embedded platform. This includes consolidating the optoelectronic circuits into a portable system capable of low-power operation, enabling battery-based autonomy, and supporting continuous or long-term monitoring without the need for external power supplies or a dedicated computer. In parallel, the signal processing algorithms, currently executed offline on a computer, would need to be migrated to an embedded or firmware-level implementation capable of real-time data acquisition, processing, and decision-making, in line with the inverse-model-based localization and point-wise pressure estimation already validated in this work. Such integration would directly address the portability and autonomy constraints identified during experimental validation and would contribute to reducing overall system complexity.

In addition to integrating the electronics and the signal-processing algorithms, future work should also consider mechanical robustness and operational reliability under repeated and prolonged use. Experimental observations related to optical attenuation, encapsulation, and mechanical coupling suggest that long-term stability studies, durability assessments, and recalibration or self-monitoring strategies will be necessary to keep performance consistent. Working on these aspects is essential to ensure reliable operation in non-controlled environments, particularly in applications involving prolonged contact or repeated pressure events.

Finally, improving system scalability and usability will be essential to making the approach suitable for use outside laboratory settings. As sensor resolution increases and grid sizes grow, the current point-by-point calibration and estimation framework may become impractical. Exploring alternative modeling strategies, such as grouped calibration schemes, hybrid approaches that combine physical models with data-driven adjustments, or machine-learning models that reduce calibration overhead while preserving interpretability, offers a clear pathway for future development. Together, these system-level improvements outline a coherent and feasible roadmap for advancing the proposed sensor from a laboratory proof-of-

concept to a pressure-sensing platform intended for application-driven research and future prototypes.

Building on these system-level considerations, given that the grid architecture has proven to be functional and repeatable, a logical evolution of the system would be to scale it up to configurations with higher spatial resolution, such as 16×16 or even 32×32 fibers. Although low-cost electronic modules have certain limitations, one of them already supports up to 32 LED outputs and could be reused without major redesigns. While this module was not effective with PU fibers in earlier tests, it could be reintegrated if fibers with improved optical transmission are integrated, thus avoiding the need for more expensive lighting systems. In the detection stage, 32 photodiode circuits of the same type used in previous prototypes could be reused, as they have proven to be compatible and reliable. Data acquisition could remain based on a DAQ system, as long as the number of input channels is enough. Otherwise, it is suggested to explore alternative low-cost platforms, such as microcontrollers or embedded systems, that support real-time acquisition, storage, and transmission of signals to a computer for analysis and interpretation.

This approach aligns with the modular and scalable nature of bending-loss-based sensors, which require fewer output channels than resistive or capacitive systems (Chang et al., 2012; H. Li et al., 2025; D. Xu et al., 2025; Yao et al., 2025). In fact, several grid-type architectures embedded in soft materials have been successfully scaled for pressure reconstruction using 2D or 3D mapping strategies (Chang et al., 2012; Soetanto et al., 2011; Wang et al., 2005), demonstrating that increased resolution can be achieved without compromising functionality. Future efforts could focus on improving the optical quality of the fibers while keeping the use of low-cost components, as this would allow scaling to larger configurations without compromising signal quality or system cost.

Improving the optical properties of the fibers is a direct way to enhance system performance. Materials with higher transmission, lower attenuation, and greater sensitivity to bending would generate cleaner and more distinguishable signals, making it easier for the inverse model to

identify the stimulated point. As a result, a reduction in localization and pressure estimation errors is expected, improving overall performance in metrics such as MAE, accuracy, and spatial sensitivity. These improvements have been reported in systems where the use of PDMS waveguides or soft embedding materials to enhance bending sensitivity and signal quality (Wang et al., 2008; Wang et al., 2005). For example, PDMS-based waveguides with porous cladding have shown directional contrast in light attenuation and a good sensitivity under small deformations (Amouzou et al., 2025).

In this regard, PDMS-based waveguides could represent a viable alternative to polyurethane or PMMA fibers. These types of waveguides have already been studied in our research group for other sensing applications, showing good optical and mechanical performance with promising results in integration capabilities that could be exploited in future versions of the sensor presented. For instance, experimental results show that these PDMS-based waveguides are highly sensitive to pressure and deformation, with reported transmission losses as low as 0.16 – 0.37 dB/cm depending on fabrication methods and doping (Amouzou et al., 2022; Zimmermann et al., 2024), but can increase to over 1.85 dB/cm in structures with porous or dyed claddings designed for specific sensing functions (Amouzou, 2025; Amouzou et al., 2025). Their mechanical properties are also favorable, demonstrating robustness after repeated loading cycles, stretchability up to 160%, and good repeatability of ± 2 – 6% in sensitivity measurements (Amouzou, 2025; Amouzou et al., 2025; Amouzou et al., 2022). These characteristics suggest strong optical and mechanical compatibility, making them a viable alternative to traditional fiber materials. While some challenges such as hysteresis, anisotropic responses in specific geometries, and higher attenuation limiting its use to short distances have been reported (Amouzou et al., 2025; Zimmermann et al., 2025), the successful integration of PDMS waveguides into functional sensing systems (Amouzou et al., 2025; Amouzou et al., 2022), along with their tunable optical and structural properties (Amouzou, 2025; Amouzou et al., 2025), suggest that this material could be explored as a core component in future versions of the pressure sensor presented, potentially improving signal quality and spatial sensitivity.

Regarding the pressure estimation models, when scaling the sensor grid, keeping an individual model for each point could become impractical. Although this approach worked well in the current configuration by ensuring high accuracy and physical interpretation, it may not be suitable for larger configurations. For example, moving from a 4×4 grid to a 32×32 configuration would require the management of more than 2100 sensing points, making manual calibration and model fitting a time-consuming and error-prone task. An initial attempt was made to generalize the estimation model globally by averaging the responses of all points to fit a single equation, but it failed due to the loss of local information and was highly sensitive to outliers, reinforcing the decision to use the point-specific models. More robust alternatives could be explored to deal with this modeling challenge in future versions of the sensor.

One strategy could involve grouping or clustering sensing points into zones based on similar optical or mechanical characteristics, allowing the calibration of a reduced set of representative models. Machine learning techniques, especially convolutional neural networks (CNNs), have already demonstrated strong performance in pressure and location estimation tasks for optical sensors, by analyzing all sensor outputs together while reducing the need for point-by-point approach (de Carvalho et al., 2025; Shabalov et al., 2024; Wang et al., 2008). Other techniques, such as CatBoost, k-NN, Support Vector Machine (SVM), Multilayer Perceptrons (MLP), and Random Forests have also been successfully applied in flexible sensing technologies like capacitive or resistive sensors for tasks such as pressure estimation, object recognition, and posture classification (H. Li et al., 2025; Meng et al., 2024; Peruzzi et al., 2025; Shabalov et al., 2024; Tian et al., 2024; D. Wang, B. Li, et al., 2025; D. Xu et al., 2025; Yoon et al., 2024; Hao Zhang et al., 2024), often achieving high accuracy even with overlapping signals or noisy measurements, while reducing calibration requirements.

Although technically speaking, the current system does not apply interpolation by itself, it already includes a validation stage that checks the estimated pressures of neighboring points to correct improbable values, for example, estimations outside the measurable range (0 mmHg – 100 mmHg). This procedure, based on the consistency between adjacent estimations, helped improve accuracy and reduce extreme errors. It reflects the gradual pressure changes across

the pad and could evolve into interpolation methods to estimate pressure values in unmeasured areas. These combined strategies may allow future versions of the sensor to scale efficiently while keeping accuracy and an easy interpretation.

Another potential improvement consists of expanding the characterization of the sensing points that were left unmeasured in the current configuration, either to strengthen the interpolation models proposed earlier or to directly enhance spatial resolution. Expanding this dataset could reduce blind areas, particularly at the edges, and help improve both localization and pressure estimation. In addition, obtaining real measurements at these locations would provide ground truth data to evaluate the reliability of future interpolation models. Although adding these points would increase the computational and experimental workload, the potential benefits for model validation and performance evaluation could justify the effort.

In addition, evaluating the sensor under more dynamic conditions, such as tests in motion or in real-world applications, could help assess the consistency and robustness of the estimations. Previous studies on bend-loss and waveguide sensors have reported signal degradation under motion, especially due to hysteresis, mechanical crosstalk, or non-monotonic deformation behaviors (Amouzou et al., 2025; Jeroen et al., 2010; Kanellos et al., 2010; Soetanto et al., 2011; Wang et al., 2008). Some designs addressed these issues through structural changes, while others applied advanced signal processing techniques or machine learning models to reduce ambiguity and maintain reliable performance under dynamic and noisy conditions (de Carvalho et al., 2025; Shabalov et al., 2024; Wen et al., 2021). These strategies suggest that, with the proper modifications, it may be feasible to transition from static to dynamic scenarios.

Finally, it would be valuable to explore the feasibility of extending the sensor to simultaneously detect pressure and shear, particularly considering potential applications where both variables matter, such as skin injuries prevention or motion analysis across contact surfaces. Although no specific configuration was fully implemented in this version, preliminary tests were performed using alternative fiber geometries, such as wave and "snake" patterns, fabricated with the same materials employed in the final sensor (PU-OFs and PDMS encapsulation).

These static tests yielded inconsistent but suggestive responses, with some indications of sensitivity to lateral forces. This exploratory phase, although inconclusive, highlights the potential of integrating shear detection into future versions.

As a result, a modular design combining dedicated units for pressure and shear, or multi-layer or stacked configurations that capture both forces simultaneously, could be considered. For example, multi-layer designs with stacked fiber grids, either aligned or slightly shifted, can detect shear by tracking the shift between the top and bottom layers, as shear-induced displacement alters the pattern of light attenuation across the layers (Chang et al., 2012; Chao-Shih et al., 2007; Soetanto et al., 2011; Wang et al., 2005). Other approaches use more independent configurations, such as orthogonal fiber pairs that respond to forces along different axes (Al-Mai et al., 2017), or asymmetric fiber arrangements where each layer is shaped to be more sensitive to either normal or shear forces (Chen et al., 2023). These designs show that shear detection can be achieved through structural configurations that differentiate between pressure and shear loads or by multi-layer displacement analysis, offering possible solutions for integrating this capability into future versions of the sensor.

Although challenges remain in signal separation and noise robustness, the combination of adapted geometries and learning based models offers a promising path for extending the sensor’s capabilities toward multi-dimensional force sensing, with potential relevance in biomedical and human-interaction contexts.

CONCLUSION

This research documented the design, fabrication, experimental evaluation, and analytical characterization of a flexible optical pressure sensor and its reconstruction system for spatial localization and pressure estimation. Through the assessment of multiple prototypes, the work established a clear understanding of the mechanisms behind intensity-modulated sensing and the variables that affect performance in polymer-based sensors. The results demonstrated that a low-cost optoelectronic system, based on custom electronics, polymer optical fibers, and an inverse model, can generate meaningful and consistent spatial responses under mechanical loading. This process validated the sensing principle and clarified the conditions under which the system achieves stable localization and interpretable pressure behavior despite the challenges associated with optical attenuation, material variability, and noise.

The analytical evaluation highlighted several key contributions. The integration of the inverse model with the point-specific pressure estimation models developed in this work enabled the reconstruction of spatial pressure responses and demonstrated the direct relationship between localization accuracy and pressure estimation quality. The characterization based on Lorentzian error distributions and their γ-based half-width metrics provided a rigorous framework to assess spatial performance, while ROC-based analyses confirmed consistent discrimination across pressure levels. Together, these findings demonstrate that functional flexible pressure sensors can be manufactured with low-cost materials and that their performance can be systematically quantified through the methodology developed in this work.

At the same time, the experimental process exposed clear limitations that currently constrain system performance. Optical losses reduce sensitivity, electronic noise affects repeatability, and mechanical coupling within the encapsulating substrate introduces variability that impacts both localization and pressure estimation. Rather than weakening the contribution, these limitations outline the boundaries of the present prototype and point to key areas such as materials, fabrication consistency, and noise reduction where further improvement is essential.

Addressing these issues while still achieving a low-cost design is necessary before advancing to application-oriented scenarios.

Overall, this work established a solid proof-of-concept and an analytical foundation for the future development of flexible optical pressure-sensing systems. The results confirmed the viability of the approach and identified the main technical limitations that must be addressed to achieve higher accuracy and robustness in future designs. The system developed in this thesis should be viewed as a foundational platform, one that demonstrates feasibility, highlights the key challenges, and lays the groundwork for subsequent improvements through enhanced materials, optimized models and electronics, and more stable fabrication methods.

ANNEX I

RESEARCH OUTPUTS

Peer-Reviewed Journal Articles

Alonso Romero, A., Amouzou, K. N., Sengupta, D., Zimmermann, C. A., Richard-Denis, A., Mac-Thiong, J.-M., Petit, Y., Lina, J.-M., & Ung, B. (2023). *Optoelectronic Pressure Sensor Based on the Bending Loss of Plastic Optical Fibers Embedded in Stretchable Polydimethylsiloxane*. *Sensors*, *23*(6), 3322. https://doi.org/10.3390/s23063322

Alonso Romero, A., Amouzou, K. N., Sengupta, D., Lina, J. M., & Ung, B. (2026). *Performance Evaluation of Flexible Optical Pressure Sensors Using Inverse Model-Based Pressure Mapping* [Article]. *Applied Sciences (Switzerland)*, *16*(4), Article 2087. https://doi.org/10.3390/app16042087

Peer-Reviewed Conference Paper

A. Romero, K. Amouzou, A. Richard-Denis, J. Mac-Thiong, Y. Petit, J. Lina, and B. Ung, *"Development of a Wearable Optoelectronic Pressure Sensor Based on the Bending Loss of Plastic Optical Fiber and Polydimethylsiloxane,"* in Optical Sensors and Sensing Congress 2022 (AIS, LACSEA, Sensors, ES), Technical Digest Series (Optica Publishing Group, 2022), paper STu4C.3.

Co-authored Journal Articles

Amouzou, K. N., **Romero, A. A.**, Sengupta, D., Mishra, S. K., Richard-Denis, A., Mac-Thiong, J. M., Petit, Y., Lina, J. M., & Ung, B. (2022). *Development of High Refractive Index Polydimethylsiloxane Waveguides Doped with Benzophenone via Solvent-Free Fabrication for Biomedical Pressure Sensing* [Article]. *Photonics*, *9*(8), Article 557. https://doi.org/10.3390/photonics9080557

Amouzou, K. N., **Alonso Romero, A.**, Sengupta, D., Zimmermann, C. A., Kumar, A., Gravel, N., Lina, J. M., Daxhelet, X., & Ung, B. (2025). *Porous-Cladding Polydimethylsiloxane Optical Waveguide for Biomedical Pressure Sensing Applications* [Article]. *Sensors*, *25*(14), Article 4311. https://doi.org/10.3390/s25144311

Amouzou, K. N., **Romero, A. A.**, D., Kumar, A., Lina, J. M., Daxhelet, X., & Ung, B. (2026). *Location-aware pressure sensing based on a colored porous-cladding polydimethylsiloxane optical waveguide* [Article]. *Sensors and Actuators A: Physical*, *402*, Article 117667. https://doi.org/10.1016/j.sna.2026.117667

LIST OF BIBLIOGRAPHICAL REFERENCES

Al-Mai, O., Ahmadi, M., & Albert, J. (2017). A Compliant 3-Axis Fiber-Optic Force Sensor for Biomechanical Measurement. *IEEE Sensors Journal*, *17*(20), 6549-6557. https://doi.org/10.1109/JSEN.2017.2750157

Ali, S. M., Noghanian, S., Khan, Z. U., Alzahrani, S., Alharbi, S., Alhartomi, M., & Alsulami, R. (2025). Wearable and Flexible Sensor Devices: Recent Advances in Designs, Fabrication Methods, and Applications. *Sensors*, *25*(5). https://doi.org/10.3390/s25051377

Alonso Romero, A., Amouzou, K. N., Sengupta, D., Zimmermann, C. A., Richard-Denis, A., Mac-Thiong, J.-M., Petit, Y., Lina, J.-M., & Ung, B. (2023). Optoelectronic Pressure Sensor Based on the Bending Loss of Plastic Optical Fibers Embedded in Stretchable Polydimethylsiloxane. *Sensors*, *23*(6), 3322. https://doi.org/10.3390/s23063322

Amjadi, M., Kyung, K. U., Park, I., & Sitti, M. (2016). Stretchable, skin-mountable, and wearable strain sensors and their potential applications: a review. *Advanced Functional Materials*, *26*(11), 1678-1698. https://doi.org/10.1002/adfm.201504755

Amouzou, K. N. (2025). *Développement et caractérisation de guides d'ondes optiques en élastomères en tant que plate-forme pour capteurs de pression flexibles biomédicaux (Development and characterization of elastomeric optical waveguides as a platform for biomedical flexible pressure sensors)* [Thèse de doctorat électronique, École de technologie supérieure, Montréal, QC]. Retrieved from https://espace.etsmtl.ca/id/eprint/3704/

Amouzou, K. N., Alonso Romero, A., Sengupta, D., Zimmermann, C. A., Kumar, A., Gravel, N., Lina, J.-M., Daxhelet, X., & Ung, B. (2025). Porous-Cladding Polydimethylsiloxane Optical Waveguide for Biomedical Pressure Sensing Applications. *Sensors*, *25*(14), 4311. Retrieved 2025, from

Amouzou, K. N., Romero, A. A., Sengupta, D., Mishra, S. K., Richard-Denis, A., Mac-Thiong, J.-M., Petit, Y., Lina, J.-M., & Ung, B. (2022). Development of High Refractive Index Polydimethylsiloxane Waveguides Doped with Benzophenone via Solvent-Free Fabrication for Biomedical Pressure Sensing. *Photonics*, *9*(8).

Aptabusjaman, M., Islam, S. R., Sadannavar, M. K., Hossain, N., Rahman, M., & Miao, D. (2025). Textile based pressure sensors: a review of materials, fabrication, and applications. *The Journal of The Textile Institute*, *116*(11), 1-23. https://doi.org/10.1080/00405000.2025.2462354

Babangida, A. A., Caraballo-Arias, Y., Decataldo, F., & Violante, F. S. (2025). Advancing Occupational Medicine through Wearable Technology: A Review of Sensor Systems for Biomechanical Risk Assessment and Work-Related Musculoskeletal Disorder

Prevention. *ACS Sensors*, *10*(8), 5410-5432. https://doi.org/10.1021/acssensors.5c01578

Bahin, L., Tourlonias, M., Bueno, M.-A., Sharma, K., & Rossi, R. M. (2023). Smart textiles with polymer optical fibre implementation for in-situ measurements of compression and bending. *Sensors and Actuators A: Physical*, *350*, 114117.

Bai, H., Li, S., Barreiros, J., Tu, Y., Pollock, C. R., & Shepherd, R. F. (2020). Stretchable distributed fiber-optic sensors. *Science*, *370*(6518), 848-852. https://doi.org/10.1126/science.aba5504

Belk, S., Rosset, S., Anderson, I., & Hesam, M. (2025). From Single Sensors to Sensor Arrays: Leveraging Supervised Machine Learning to Read Multiple Soft Capacitive Sensors with a Single Pair of Wires. *Advanced Intelligent Systems*, *7*(7), 2400773. https://doi.org/10.1002/aisy.202400773

Beloshenko, V., Beigel'zimer, Y. E., Varyukhin, V., & Voznyak, Y. V. (2006). Strain hysteresis of polymers. Doklady Physical Chemistry,

Bi, S., Jin, W., Han, X., Metts, J., Ostrosky, A. D., Lehotsky, J., He, Z., Jiang, C., & Asare-Yeboah, K. (2023). Flexible pressure visualization equipment for human-computer interaction. *Materials Today Sustainability*, *21*, 100318. https://doi.org/ARTN 100318 10.1016/j.mtsust.2023.100318

Bijender, Kumar, S., Soni, A., Yadav, R., Singh, S. P., & Kumar, A. (2024). Noninvasive Blood Pressure Monitoring via a Flexible and Wearable Piezoresistive Sensor. *ACS Omega*, *9*(6), 6355-6365. https://doi.org/10.1021/acsomega.3c04786

Butt, M. A., Kazanskiy, N. L., & Khonina, S. N. (2022). Revolution in Flexible Wearable Electronics for Temperature and Pressure Monitoring—A Review. *Electronics*, *11*(5). https://mdpi-res.com/d_attachment/electronics/electronics-11-00716/article_deploy/electronics-11-00716-v2.pdf?version=1646039949

Butt, M. A., Voronkov, G. S., Grakhova, E. P., Kutluyarov, R. V., Kazanskiy, N. L., & Khonina, S. N. (2022). Environmental Monitoring: A Comprehensive Review on Optical Waveguide and Fiber-Based Sensors. *Biosensors*, *12*(11). https://doi.org/10.3390/bios12111038

Capp, E., Pontin, M., Walters, P., & Maiolino, P. (2025, 22-26 April 2025). Soft and Highly-Integrated Optical Fiber Bending Sensors for Proprioception in Multi-Material 3D Printed Fingers. 2025 IEEE 8th International Conference on Soft Robotics (RoboSoft),

Chad Webb, R., Krishnan, S., & Rogers, J. A. (2016). Ultrathin, Skin-Like Devices for Precise, Continuous Thermal Property Mapping of Human Skin and Soft Tissues. In J. A. Rogers, R. Ghaffari, & D.-H. Kim (Eds.), *Stretchable Bioelectronics for Medical*

Devices and Systems (pp. 117-132). Springer International Publishing. https://doi.org/10.1007/978-3-319-28694-5_6

Chang, C.-T., Liu, C. S., Soetanto, W., & Wang, W.-C. (2012). *A platform-based foot pressure/shear sensor* (Vol. 8348). SPIE. https://doi.org/10.1117/12.915396

Chang, K., Zhang, C., & Liu, T. (2025). A Comprehensive Review on Fabrication and Structural Design of Polymer Composites for Wearable Pressure Sensors. *Polymer Science & Technology*, *1*(1), 3-24. https://doi.org/10.1021/polymscitech.4c00047

Chang, T.-S., Chien, C.-W., Guerra, E. I., Wang, T.-Y., Huang, C.-W., Lin, Y.-S., Chang, J.-C., & Liao, W.-S. (2025). Wireless, flexible, and disposable sensing devices enabling real-time long-term patient medical care for pressure injury prevention. *Journal of Materials Chemistry C*, *13*(16), 7943-7956. https://doi.org/10.1039/D4TC05320F

Chao-Shih, L., Gia Wen, C., Xin, L., Per, G. R., & Wei-Chih, W. (2007). Design of a multi-layered optical bend loss sensor for pressure and shear sensing. Proc.SPIE,

Chen, D., Cui, R., Huang, C., Wang, Z., & Niu, L. (2025). Wearable Mechanoluminescent Triboelectric Sensors for Real-Time Monitoring of Nighttime Sports Activities. *ACS Applied Materials & Interfaces*, *17*(12), 18844-18851. https://doi.org/10.1021/acsami.4c22118

Chen, H., Hong, W., Long, Q., Li, X., Hou, M., Zhu, X., Lin, Z., Wang, X., Hou, H., Zhao, Y., Hong, Q., Xu, W., Zhao, X., & Guo, X. (2025). High-Performance Flexible Pressure Sensor Based on Biomimetic Grasshopper Leg Structure for Wearable Devices and Human-Machine Interaction. *IEEE Transactions on Electron Devices*, *72*(3), 1352-1359. https://doi.org/10.1109/TED.2025.3527948

Chen, W., & Yan, X. (2020). Progress in achieving high-performance piezoresistive and capacitive flexible pressure sensors: A review. *Journal of Materials Science & Technology*, *43*, 175-188. https://doi.org/10.1016/j.jmst.2019.11.010

Chen, W., Yan, Y., Zhang, Z., Yang, L., & Pan, J. (2023). Polymer-Based Self-Calibrated Optical Fiber Tactile Sensor. IEEE International Conference on Intelligent Robots and Systems,

Chen, Z., Ma, J., Zhang, X., Wei, A., Luo, N., He, Y., Zhao, Y., Liu, Z., & Xu, J. (2025). High-sensitivity and ultra-broad linear working region flexible piezoresistive pressure sensors based on PDMS/CNT/TPU. *Journal of Alloys and Compounds*, *1010*, 177711. https://doi.org/10.1016/j.jallcom.2024.177711

Chen, Z., Wang, Y., Zhang, Z., Mei, D., & Liu, W. (2025). Flexible dual-mode sensor with accurate contact pressure sensing and contactless distance detection functions for robotic perception. *Journal of Intelligent Manufacturing*, *36*(2), 1445-1457. https://doi.org/10.1007/s10845-023-02314-x

Chenu, O., Vuillerme, N., Bucki, M., Diot, B., Cannard, F., & Payan, Y. (2013). TexiCare: An innovative embedded device for pressure ulcer prevention. Preliminary results with a paraplegic volunteer. *Journal of Tissue Viability*, *22*(3), 83-90. https://doi.org/10.1016/j.jtv.2013.05.002

Cui, Z., Hua, Q., Shi, Y., Wei, R., Dong, Z., Dai, X., Huang, T., Shen, G., Wang, Z. L., & Hu, W. (2025). Skin-integrated haptic interface system based on a stretchable pressure sensor array for wireless tactile visualization applications. *Nano Energy*, *139*, 110911. https://doi.org/10.1016/j.nanoen.2025.110911

de Carvalho, V., Martins, V. H., Flores, W. O. C., Muller, M., Fabris, J. L., & Lazzaretti, A. E. (2025). CNN-based multiplexed optical fiber sensors for multi-load mapping on 2D structures. *Optical Fiber Technology*, *93*, 104231. https://doi.org/10.1016/j.yofte.2025.104231

Dong, C., Bai, Y., Zou, J., Cheng, J., An, Y., Zhang, Z., Li, Z., Lin, S., Zhao, S., & Li, N. (2024). Flexible capacitive pressure sensor: material, structure, fabrication and application. *Nondestructive Testing and Evaluation*, *39*(7), 1749-1790. https://doi.org/10.1080/10589759.2024.2327639

Duan, L., D'hooge, D. R., & Cardon, L. (2020). Recent progress on flexible and stretchable piezoresistive strain sensors: From design to application. *Progress in Materials Science*, *114*, 100617. https://doi.org/ARTN 100617 10.1016/j.pmatsci.2019.100617

Dulal, M., Afroj, S., Ahn, J., Cho, Y., Carr, C., Kim, I.-D., & Karim, N. (2022). Toward Sustainable Wearable Electronic Textiles. *ACS Nano*, *16*(12), 19755-19788. https://doi.org/10.1021/acsnano.2c07723

Egger, P. W., Srinivas, G. L., & Brandstötter, M. (2025). Real-Time Detection and Localization of Force on a Capacitive Elastomeric Sensor Array Using Image Processing and Machine Learning. *Sensors*, *25*(10). https://doi.org/10.3390/s25103011

Farooq, A. S., & Zhang, P. (2022). A comprehensive review on the prospects of next-generation wearable electronics for individualized health monitoring, assistive robotics, and communication. *Sensors and Actuators A: Physical*, *344*, 113715. https://doi.org/ARTN 113715 10.1016/j.sna.2022.113715

Funnell, A. C., & Thomas, P. J. (2023). Design of a Flexible Weight Sensor Using Optical Fibre Macrobending. *Sensors*, *23*(2), 912. https://doi.org/10.3390/s23020912

Gan, J., Yang, A., Guo, Q., & Yang, Z. (2024). Flexible Optical Fiber Sensing: Materials, Methodologies, and Applications. *Advanced Devices & Instrumentation*, *5*, 0046. https://doi.org/10.34133/adi.0046

Gao, H., & Chen, T. (2023). A flexible ultra-highly sensitive capacitive pressure sensor for basketball motion monitoring. *Discover Nano*, *18*(1), 17. https://doi.org/10.1186/s11671-023-03783-y

Gao, K., Zhang, Z., Weng, S., Zhu, H., Yu, H., & Peng, T. (2022). Review of Flexible Piezoresistive Strain Sensors in Civil Structural Health Monitoring. *Applied Sciences*, *12*(19), 9750. https://doi.org/ARTN 9750 10.3390/app12199750

Gao, W., Ota, H., Kiriya, D., Takei, K., & Javey, A. (2019). Flexible Electronics toward Wearable Sensing. *Accounts of Chemical Research*, *52*(3), 523-533. https://doi.org/10.1021/acs.accounts.8b00500

Ghaffar, A., Ru, F., Liu, J., Chen, G. Y., Ni, J., Liu, J., Hussian, S., Yu, J., Das, B., & Mehdi, M. (2024). High pressure sensor based on intensity-variation using polymer optical fiber. *Scientific Reports*, *14*(1), 18604. https://doi.org/10.1038/s41598-024-69094-z

González-Cely, A. X., Diaz, C. A. R., Callejas-Cuervo, M., & Bastos-Filho, T. (2024). Optical fiber sensors for posture monitoring, ulcer detection and control in a wheelchair: a state-of-the-art. *Disability and Rehabilitation: Assistive Technology*, *19*(4), 1773-1790. https://doi.org/10.1080/17483107.2023.2234411

Grosch, K., Harwood, J., & Payne, A. (1968). Hysteresis in Polymers and its Relation to Strength. *Rubber Chemistry and Technology*, *41*(5), 1157-1167.

Gu, Y., Zhang, T., Chen, H., Wang, F., Pu, Y., Gao, C., & Li, S. (2019). Mini review on flexible and wearable electronics for monitoring human health information. *Nanoscale research letters*, *14*(1), 1-15. https://doi.org/10.1186/s11671-019-3084-x

Guo, M., Xia, Y., Liu, J., Zhang, Y., Li, M., & Wang, X. (2025). Wearable Pressure Sensor Based on Triboelectric Nanogenerator for Information Encoding, Gesture Recognition, and Wireless Real-Time Robot Control. *Advanced Functional Materials*, *35*(22), 2419209. https://doi.org/10.1002/adfm.202419209

Guo, X., Li, Y., Hong, W., Yan, Z., Duan, Z., Zhang, A., Zhang, X., Jin, C., Liu, T., Li, X., He, J., Hong, Q., Xu, Y., & Zhao, Y. (2024). Bamboo-Inspired, Environmental Friendly PDMS/Plant Fiber Composites-Based Capacitive Flexible Pressure Sensors by Origami for Human–Machine Interaction. *ACS Sustainable Chemistry & Engineering*, *12*(12), 4835-4845. https://doi.org/10.1021/acssuschemeng.3c06949

Guo, Y., Li, Y., Sun, J., Yao, X., Liu, Q., Li, X., Zeng, S., Zhu, M., & Deng, T. (2024). Status, Applications, and Challenges of Flexible Pressure Sensors Based on 2-D Materials: A Review. *IEEE Sensors Journal*, *24*(7), 9251-9277. https://doi.org/10.1109/JSEN.2024.3359279

Han, S. T., Peng, H., Sun, Q., Venkatesh, S., Chung, K. S., Lau, S. C., Zhou, Y., & Roy, V. (2017). An overview of the development of flexible sensors. *Advanced Materials*, *29*(33), 1700375. https://doi.org/10.1002/adma.201700375

Hanson, D. E., Hawley, M., Houlton, R., Chitanvis, K., Rae, P., Orler, E. B., & Wrobleski, D. A. (2005). Stress softening experiments in silica-filled polydimethylsiloxane provide insight into a mechanism for the Mullins effect. *Polymer*, *46*(24), 10989-10995. https://doi.org/10.1016/j.polymer.2005.09.039

He, R., Shen, L., Wang, Z., Wang, G., Qu, H., Hu, X., & Min, R. (2023). Optical fiber sensors for heart rate monitoring: A review of mechanisms and applications. *Results in Optics*, *11*, 100386. https://doi.org/ARTN 100386 10.1016/j.rio.2023.100386

Heng, W., Solomon, S., & Gao, W. (2022). Flexible electronics and devices as human–machine interfaces for medical robotics. *Advanced Materials*, *34*(16), 2107902. https://doi.org/ARTN 2107902 10.1002/adma.202107902

Homayounfar, S. Z., & Andrew, T. L. (2020). Wearable Sensors for Monitoring Human Motion: A Review on Mechanisms, Materials, and Challenges. *SLAS Technology*, *25*(1), 9-24. https://doi.org/https://doi.org/10.1177/2472630319891128

Hua, J., Su, M., Wu, J., Zhou, Y., Guo, Y., Shi, Y., & Pan, L. (2024). Wearable cuffless blood pressure monitoring: From flexible electronics to machine learning. *Wearable Electronics*, *1*, 78-90. https://doi.org/10.1016/j.wees.2024.05.004

Huang, G., Chen, X., & Liao, C. (2025). AI-Driven Wearable Bioelectronics in Digital Healthcare. *Biosensors*, *15*(7). https://doi.org/10.3390/bios15070410

Huang, J., Liu, H., Chen, Q., Xie, H., & Zhou, S. (2025). Shape-Programmable Lamellar Aerogel Enabling 3D Wireless Point-of-Care Electronics for Assistance in Pressure Injury Prevention. *Advanced Functional Materials*, *35*(13), 2418037. https://doi.org/10.1002/adfm.202418037

Huang, Y., Fan, X., Chen, S.-C., & Zhao, N. (2019). Emerging Technologies of Flexible Pressure Sensors: Materials, Modeling, Devices, and Manufacturing. *Advanced Functional Materials*, *29*(12), 1808509. https://doi.org/10.1002/adfm.201808509

Huang, Y., Fan, X., Chen, S. C., & Zhao, N. (2019). Emerging Technologies of Flexible Pressure Sensors: Materials, Modeling, Devices, and Manufacturing [Review]. *Advanced Functional Materials*, *29*(12), Article 1808509. https://doi.org/10.1002/adfm.201808509

Huang, Z., Duan, Z., Huang, Q., Yuan, Z., Jiang, Y., & Tai, H. (2024). A facilely fabricated electrochemical self-powered pressure sensor for multifunctional applications. *Journal of Materials Chemistry C*, *12*(45), 18320-18326. https://doi.org/10.1039/D4TC03434A

Huang, Z., Ge, C., Li, S., Cai, M., Hui, Y., Liao, X., & Zeng, Q. (2025). Biomimetic Pyrolytic MXene-Based Multifunctional Films with Multi-Level Structure for Wearable Piezoresistive Devices and Bioelectronics. *Advanced Functional Materials*, *35*(17), 2422374. https://doi.org/10.1002/adfm.202422374

Iglio, R., Mariani, S., Robbiano, V., Strambini, L., & Barillaro, G. (2018). Flexible polydimethylsiloxane foams decorated with multiwalled carbon nanotubes enable unprecedented detection of ultralow strain and pressure coupled with a large working range. *ACS Applied Materials & Interfaces*, *10*(16), 13877-13885. https://doi.org/10.1021/acsami.8b02322

Im, S. M., & Kim, M. g. (2024, 2024/10/20/23). Facile and Scalable Fabrication of Micro-Dome Structure Array Based on Liquid Metal and its Application for High-Performance Flexible Pressure Sensors. 2024 IEEE SENSORS,

Jeon, S., Lim, S.-C., Trung, T. Q., Jung, M., & Lee, N.-E. (2019). Flexible multimodal sensors for electronic skin: principle, materials, device, array architecture, and data acquisition method. *Proceedings of the IEEE*, *107*(10), 2065-2083. https://doi.org/10.1109/Jproc.2019.2930808

Jeroen, M., Geert Van, S., Bram Van, H., Erwin, B., Christof, D., Jürgen Van, E., Chunxiao, Y., Eleonora, F., Peter Van, D., Jan, V., Hugo, T., & Dominiek, R. (2010). High density optical pressure sensor foil based on arrays of crossing flexible waveguides. Proc.SPIE,

Jia, B., Li, Z., Zheng, T., Wang, J., Zhao, Z.-J., Zhao, L., Wang, B., Lu, J., Zhao, K., Luo, G., Li, M., Lin, Q., & Jiang, Z. (2024). Highly-sensitive, broad-range, and highly-dynamic MXene pressure sensors with multi-level nano-microstructures for healthcare and soft robots applications. *Chemical Engineering Journal*, *485*, 149750. https://doi.org/10.1016/j.cej.2024.149750

Kanellos, G. T., Papaioannou, G., Tsiokos, D., Mitrogiannis, C., Nianios, G., & Pleros, N. (2010). Two dimensional polymer-embedded quasi-distributed FBG pressure sensor for biomedical applications. *Optics Express*, *18*(1), 179-186. https://doi.org/10.1364/OE.18.000179

Karimian, S., Ali, M. M., McAfee, M., Saleem, W., Duraibabu, D., Memon, S. F., & Lewis, E. (2025). Challenges in Adapting Fibre Optic Sensors for Biomedical Applications. *Biosensors*, *15*(5). https://doi.org/10.3390/bios15050312

Katrenova, Z., Alisherov, S., Abdol, T., Yergibay, M., Kappassov, Z., Tosi, D., & Molardi, C. (2022). Investigation of High-Resolution Distributed Fiber Sensing System Embedded in Flexible Silicone Carpet for 2D Pressure Mapping. *Sensors*, *22*(22). https://doi.org/10.3390/s22228800

Kazanskiy, N. L., Butt, M. A., & Khonina, S. N. (2022). Recent Advances in Wearable Optical Sensor Automation Powered by Battery versus Skin-like Battery-Free Devices for

Personal Healthcare—A Review. *Nanomaterials*, *12*(3). https://mdpi-res.com/d_attachment/nanomaterials/nanomaterials-12-00334/article_deploy/nanomaterials-12-00334.pdf?version=1642759613

Ke, A., Mai, Z., Yu, D., & Zhang, X. (2025). Scalable Photonic Crystal Sensors and Arrays Integrating Power-Free Display Interface With Dual-Mode Optical/Electrical Feedback for Real-Time Physiological Analysis. *Advanced Healthcare Materials*, *n/a*(n/a), e02797. https://doi.org/10.1002/adhm.202502797

Kim, J., Campbell, A. S., de Ávila, B. E.-F., & Wang, J. (2019). Wearable biosensors for healthcare monitoring. *Nature biotechnology*, *37*(4), 389-406. https://doi.org/10.1038/s41587-019-0045-y

Kim, S. W., Lee, J.-H., Ko, H. J., Lee, S., Bae, G. Y., Kim, D., Lee, G., Lee, S. G., & Cho, K. (2024). Mechanically Robust and Linearly Sensitive Soft Piezoresistive Pressure Sensor for a Wearable Human–Robot Interaction System. *ACS Nano*, *18*(4), 3151-3160. https://doi.org/10.1021/acsnano.3c09016

Kim, Y., & Oh, J. H. (2020). Recent Progress in Pressure Sensors for Wearable Electronics: From Design to Applications. *Applied Sciences*, *10*(18). https://doi.org/10.3390/app10186403

Kisannagar, R. R., Lee, J., Park, Y., & Jung, I. (2025). Development of a PVDF/1D–2D nanofiller porous structure pressure sensor using near-field electrospinning for human motion and vibration sensing. *Journal of Materials Chemistry C*, *13*(11), 5700-5710. https://doi.org/10.1039/D4TC05253F

Kumar, S., K M, Y., & D, S. (2025). Developed machine learning algorithm for fiber Bragg grating sensor using Gaussian mixing method. *Discover Sensors*, *1*(1), 14. https://doi.org/10.1007/s44397-025-00014-0

Leal-Junior, A. G., Diaz, C. A. R., Avellar, L. M., Pontes, M. J., Marques, C., & Frizera, A. (2019). Polymer Optical Fiber Sensors in Healthcare Applications: A Comprehensive Review. *Sensors (Basel)*, *19*(14), 3156. https://doi.org/10.3390/s19143156

Leber, A., Cholst, B., Sandt, J., Vogel, N., & Kolle, M. (2019). Stretchable Thermoplastic Elastomer Optical Fibers for Sensing of Extreme Deformations. *Advanced Functional Materials*, *29*(5), 1802629. https://doi.org/https://doi.org/10.1002/adfm.201802629

Lee, H., Kim, G., & Barocio, E. (2025). Investigation of tactile and strain sensing utilizing carbon-fiber network in silicone elastomer matrix. *Functional Composites and Structures*, *7*(1), 015003. https://doi.org/10.1088/2631-6331/adaffe

Lee, K.-P., Wang, Z., Zheng, L., Liang, R., Fok, Q., Lu, C., Lu, L., Cheung, J. P., Yick, K.-L., & Yip, J. (2025). Enhancing Orthotic Treatment for Scoliosis: Development of Body

Pressure Mapping Knitwear with Integrated FBG Sensors. *Sensors*, *25*(5). https://doi.org/10.3390/s25051284

Leitão, C., Pereira, S. O., Marques, C., Cennamo, N., Zeni, L., Shaimerdenova, M., Ayupova, T., & Tosi, D. (2022). Cost-Effective Fiber Optic Solutions for Biosensing. *Biosensors*, *12*(8), 575. https://doi.org/10.3390/bios12080575

Li, G., Zhang, Y., Zhang, X., Zhu, B., Lei, Y., Chen, D., Shui, L., Wu, G., & Xue, L. (2025). Filiform Papillae-Inspired Wearable Pressure Sensor with High Sensitivity and Wide Detection Range. *Advanced Functional Materials*, *35*(5), 2414465. https://doi.org/10.1002/adfm.202414465

Li, H., Zhang, C., Xu, H., Yang, Q., Luo, Z., Li, C., Kai, L., Meng, Y., Zhang, J., Liang, J., & Chen, F. (2025). Microstructured Liquid Metal-Based Embedded-Type Sensor Array for Curved Pressure Mapping. *Advanced Science*, *12*(3), 2413233. https://doi.org/10.1002/advs.202413233

Li, L., Liu, Y., Wang, Z., Wang, D., Yang, K., Hu, H., Qi, S., Fang, L., Han, L., & Zhang, R. (2024). Highly-sensitive ultrathin flexible pressure sensor based on quasi-2D conductive network for human physiological signal monitoring. *Chemical Engineering Journal*, *498*, 154355. https://doi.org/10.1016/j.cej.2024.154355

Li, L., Zheng, J., Chen, J., Luo, Z., Su, Y., Tang, W., Gao, X., Li, Y., Cao, C., Liu, Q., Kang, X., Wang, L., & Li, H. (2020). Flexible Pressure Sensors for Biomedical Applications: From Ex Vivo to In Vivo [https://doi.org/10.1002/admi.202000743]. *Advanced Materials Interfaces*, *7*(17), 2000743. https://doi.org/https://doi.org/10.1002/admi.202000743

Li, X., Zhang, J. M., & Duan, H. (2025). Enhanced Sensitivity and Versatile Detection: Dual-Sized Microsphere-Type Pressure Sensors for Soft Robotics and Wearable Electronics. *ACS Applied Materials & Interfaces*, *17*(7), 11268-11277. https://doi.org/10.1021/acsami.4c19022

Li, Y., Chen, Z., Zhang, K., Wang, S., Bu, X., Tan, J., Song, W., Mu, Z., Zhang, P., & Huang, L. (2024). A Flexible Capacitive Pressure Sensor with Adjustable Detection Range Based on the Inflatable Dielectric Layer for Human–Computer Interaction. *ACS Applied Materials & Interfaces*, *16*(30), 40250-40262. https://doi.org/10.1021/acsami.4c08387

Li, Y., Jiang, D., An, Y., Chen, W., Huang, Z., & Jiang, B. (2024). Wearable flexible pressure sensors: an intriguing design towards microstructural functionalization. *Journal of Materials Chemistry A*, *12*(12), 6826-6874. https://doi.org/10.1039/D3TA05568J

Liu, J. J., Huang, M.-C., Xu, W., & Sarrafzadeh, M. (2014). Bodypart localization for pressure ulcer prevention. 2014 36th annual international conference of the ieee engineering in medicine and biology society,

Liu, R., Xu, K., & Zhang, Y. (2020). Nanomaterial-based wearable pressure sensors: A minireview. *Instrumentation Science & Technology*, *48*(4), 459-479. https://doi.org/10.1080/10739149.2020.1737935

Liu, X., Hao, S., Wang, Y., Zheng, L., Hu, Z., Wen, J., Xu, F., & Yang, J. (2025). Mechanically adaptable microdomed hydrogels for flexible pressure sensors with broad detection range and stable signal output. *Chemical Engineering Journal*, *505*, 159113. https://doi.org/10.1016/j.cej.2024.159113

Lopez-Higuera, J. M., Cobo, L. R., Incera, A. Q., & Cobo, A. (2011). Fiber Optic Sensors in Structural Health Monitoring. *Journal of Lightwave Technology*, *29*(4), 587-608. https://doi.org/10.1109/JLT.2011.2106479

Lu, X., Wang, T., Zhong, S., Cao, T., Zhou, C., Li, L., Zhang, Q., Tian, S., Jin, T., Yue, T., & Xie, S. (2025). Self-Powered Multimodal Tactile Sensing Enabled by Hybrid Triboelectric and Magnetoelastic Mechanisms. *Cyborg and Bionic Systems*, *6*, 0320. https://doi.org/10.34133/cbsystems.0320

Lu, X., Zhang, F., Zhu, L., Peng, S., Yan, J., Shi, Q., Chen, K., Chang, X., Zhu, H., Zhang, C., Huang, W., & Cheng, Q. (2024). A terahertz meta-sensor array for 2D strain mapping. *Nature Communications*, *15*(1), 3157. https://doi.org/10.1038/s41467-024-47474-3

Luo, Z., Li, H., Li, C., Zhang, C., Yang, Q., & Chen, F. (2025). Supermetalphobic surfaces fabricated by femtosecond laser enable reliable and low-hysteresis liquid metal based flexible capacitive pressure sensor. *Applied Materials Today*, *42*, 102621. https://doi.org/10.1016/j.apmt.2025.102621

Ma, H., Zhang, H., Zhu, M., & Zhang, Y. (2025). Flexible Pressure Sensor Based on Highly Oriented PVDF/ZnONRs@Ag Electrospun Fibers for Directional Sensing. *ACS Sensors*, *10*(4), 3033-3043. https://doi.org/10.1021/acssensors.5c00095

Ma, K., Ma, L., Li, C., Zhu, R., Yang, J., Liu, S., & Tao, X. (2025). Textile-Based Mechanoreceptor Array with Tunable Pressure Thresholds for Mutli-dimensional Detection in Healthcare Monitoring. *Advanced Fiber Materials*, *7*(5), 1590-1604. https://doi.org/10.1007/s42765-025-00572-3

Majumder, S., Roy, A. K., Mondal, T., & Deen, M. J. (2025). Flexible Sensors for IoT-Based Health Monitoring. *IEEE Journal on Flexible Electronics*, *4*(2), 63-88. https://doi.org/10.1109/JFLEX.2025.3538808

Mao, L., Pan, T., Lin, L., Ke, Y., Su, H., Li, Y., Huang, W., Li, T., & Lin, Y. (2024). Simultaneously enhancing sensitivity and operation range of flexible pressure sensor by constructing a magnetic-guided microstructure in laser-induced graphene composite. *Chemical Engineering Journal*, *481*, 148639. https://doi.org/10.1016/j.cej.2024.148639

Masihi, S., Panahi, M., Maddipatla, D., Hanson, A. J., Bose, A. K., Hajian, S., Palaniappan, V., Narakathu, B. B., Bazuin, B. J., & Atashbar, M. Z. (2021). Highly Sensitive Porous PDMS-Based Capacitive Pressure Sensors Fabricated on Fabric Platform for Wearable Applications. *ACS Sensors*, *6*(3), 938-949. https://doi.org/10.1021/acssensors.0c02122

Meng, K., Xiao, X., Wei, W., Chen, G., Nashalian, A., Shen, S., Xiao, X., & Chen, J. (2022). Wearable Pressure Sensors for Pulse Wave Monitoring. *Advanced Materials*, *34*(21), 2109357. https://doi.org/10.1002/adma.202109357

Meng, X., Tang, H., Lü, X., Shi, Y., & Bao, W. (2024). Electronic skin with shape sensing and Bending-Insensitive pressure sensing for soft robotic grippers object recognition. *Measurement*, *234*, 114819. https://doi.org/10.1016/j.measurement.2024.114819

Min, R., Hu, X., Pereira, L., Simone Soares, M., Silva, L. C. B., Wang, G., Martins, L., Qu, H., Antunes, P., Marques, C., & Li, X. (2022). Polymer optical fiber for monitoring human physiological and body function: A comprehensive review on mechanisms, materials, and applications. *Optics & Laser Technology*, *147*, 107626. https://doi.org/https://doi.org/10.1016/j.optlastec.2021.107626

Min, R., Liu, Z., Pereira, L., Yang, C., Sui, Q., & Marques, C. (2021). Optical fiber sensing for marine environment and marine structural health monitoring: A review. *Optics & Laser Technology*, *140*, 107082. https://doi.org/https://doi.org/10.1016/j.optlastec.2021.107082

Moeinnia, H., Agron, D. J., Ganzert, C., Schubert, L., & Kim, W. S. (2024). Wireless pressure monitoring system utilizing a 3D-printed Origami pressure sensor array. *npj Flexible Electronics*, *8*(1), 21. https://doi.org/10.1038/s41528-024-00309-z

Moka Vidyanag, N., Grant, J., Dahl, J., Yoon, J., & Cakmak, M. (2025). Flexible and Anisotropic Large-Area Piezoresistive Films for High Spatial Resolution Pressure Mapping. *ACS Applied Materials & Interfaces*, *17*(24), 36148-36169. https://doi.org/10.1021/acsami.5c03350

Ngiejungbwen, L. A., Hamdaoui, H., & Chen, M.-Y. (2024). Polymer optical fiber and fiber Bragg grating sensors for biomedical engineering Applications: A comprehensive review. *Optics & Laser Technology*, *170*, 110187.

Ochoa, M., Algorri, J. F., Roldán-Varona, P., Rodríguez-Cobo, L., & López-Higuera, J. M. (2021). Recent Advances in Biomedical Photonic Sensors: A Focus on Optical-Fibre-Based Sensing. *Sensors*, *21*(19). https://doi.org/10.3390/s21196469

Pan'kov, A. A. (2025). Statistical model for a mechanoluminescent fiber-optic sensor in a polymer indicator coating. *Journal of Optical Technology*, *92*(2), 108-113. https://doi.org/10.1364/JOT.92.000108

Peruzzi, G., Galli, A., Giorgi, G., & Pozzebon, A. (2025). Sleep Posture Detection via Embedded Machine Learning on a Reduced Set of Pressure Sensors. *Sensors*, *25*(2). https://doi.org/10.3390/s25020458

Peters, K. (2010). Polymer optical fiber sensors—a review. *Smart materials and structures*, *20*(1), 013002.

Qi, D., Zhang, K., Tian, G., Jiang, B., & Huang, Y. (2021). Stretchable electronics based on PDMS substrates. *Advanced Materials*, *33*(6), 2003155. https://doi.org/10.1002/adma.202003155

Roriz, P., Frazão, O., Lobo-Ribeiro, A. B., Santos, J. L., & Simões, J. A. (2013). Review of fiber-optic pressure sensors for biomedical and biomechanical applications. *Journal of biomedical optics*, *18*(5), 050903-050903. https://doi.org/10.1117/1.JBO.18.5.050903

Ruth, S. R. A., Feig, V. R., Tran, H., & Bao, Z. (2020). Microengineering Pressure Sensor Active Layers for Improved Performance. *Advanced Functional Materials*, *30*(39), 2003491. https://doi.org/10.1002/adfm.202003491

Sabri, N., Aljunid, S. A., Salim, M. S., & Fouad, S. (2015). Fiber Optic Sensors: Short Review and Applications. In F. L. Gaol, K. Shrivastava, & J. Akhtar (Eds.), *Recent Trends in Physics of Material Science and Technology* (pp. 299-311). Springer Singapore. https://doi.org/10.1007/978-981-287-128-2_19

Schwartz, G., Tee, B. C. K., Mei, J., Appleton, A. L., Kim, D. H., Wang, H., & Bao, Z. (2013). Flexible polymer transistors with high pressure sensitivity for application in electronic skin and health monitoring. *Nature Communications*, *4*(1), 1859. https://doi.org/10.1038/ncomms2832

Shabalov, N., Wolf, A., Kokhanovskiy, A., Dostovalov, A., & Babin, S. (2024). Soft 2D tactile sensor based on fiber Bragg gratings and machine learning algorithms. *Sensors and Actuators A: Physical*, *369*, 115219. https://doi.org/10.1016/j.sna.2024.115219

Shang, X., Zhang, C., Cai, C., Han, L., & Li, Z. (2025). Mold-assisted self-assembled electrospun fiber membranes with ordered microstructure arrays for flexible pressure sensors. *Chemical Engineering Journal*, *519*, 165111. https://doi.org/10.1016/j.cej.2025.165111

Shen, G. (2021). Recent advances of flexible sensors for biomedical applications. *Progress in Natural Science: Materials International*, *31*(6), 872-882. https://doi.org/10.1016/j.pnsc.2021.10.005

Shiyi, W., Xiaoliang, C., Sheng, L., Bai, S., Xiaoming, C., Hongmiao, T., Chunhui, W., Xiangming, L., & Jinyou, S. (2025). Advances in micro/nano-engineered flexible sensor arrays for intelligent human-machine interaction. *Energy Materials*, *5*(3), 28. https://doi.org/10.20517/ss.2025.11

Shu, J., Wang, J., Su, Y., Liu, M., Li, Y., Lu, H.-Y., Alam, M. M., Ti, C.-H. E., Tong, S. F., Gao, Z., Guo, Z., Li, Z., & Tong, R. K.-y. (2025). Magnetoelastic Sensing: A Study of Flexible Magnetoelastic Strain Sensors for Highly Deformed Posture Perception. *Advanced Materials Technologies*, *10*(12), 2401496. https://doi.org/10.1002/admt.202401496

Shu, Q., Pang, Y., Li, Q., Gu, Y., Liu, Z., Liu, B., Li, J., & Li, Y. (2024). Flexible resistive tactile pressure sensors. *Journal of Materials Chemistry A*, *12*(16), 9296-9321. https://doi.org/10.1039/D3TA06976A

Soetanto, W., Nguyen, N., & Wang, W.-C. (2011). *Fiber optic plantar pressure/shear sensor* (Vol. 7984). SPIE. https://doi.org/10.1117/12.880680

Son, D., Koo, J. H., Lee, J., & Kim, D.-H. (2016). High-Performance Wearable Bioelectronics Integrated with Functional Nanomaterials. *Stretchable Bioelectronics for Medical Devices and Systems*, 151-171.

Souri, H., Banerjee, H., Jusufi, A., Radacsi, N., Stokes, A. A., Park, I., Sitti, M., & Amjadi, M. (2020). Wearable and stretchable strain sensors: materials, sensing mechanisms, and applications. *Advanced Intelligent Systems*, *2*(8), 2000039. https://doi.org/ARTN 2000039 10.1002/aisy.202000039

Stankova, N. E., Atanasov, P. A., Nikov, R. G., Nikov, R. G., Nedyalkov, N. N., Stoyanchov, T. R., Fukata, N., Kolev, K. N., Valova, E. I., Georgieva, J. S., & Armyanov, S. A. (2016). Optical properties of polydimethylsiloxane (PDMS) during nanosecond laser processing. *E-MRS 2015 Spring Meeting Symposium CC: "Laser and plasma processing for advanced applications in material science", 11-15 May 2015, Lille (France)*, *374*, 96-103. https://doi.org/10.1016/j.apsusc.2015.10.016

Sun, Y., He, W., Jiang, C., Li, J., Liu, J., & Liu, M. (2025). Wearable Biodevices Based on Two-Dimensional Materials: From Flexible Sensors to Smart Integrated Systems. *Nano-Micro Letters*, *17*(1), 109. https://doi.org/10.1007/s40820-024-01597-w

Sweeney, D. C., Schrell, A. M., & Petrie, C. M. (2021). Pressure-Driven Fiber-Optic Sensor for Online Corrosion Monitoring. *IEEE Transactions on Instrumentation and Measurement*, *70*, 1-10. https://doi.org/10.1109/TIM.2021.3089231

Taharat, A., Kabir, M. A., Keats, A. I., Rakib, A. K. M., & Sagor, R. H. (2025). Advancing optomechanical sensing: Novel CMOS-compatible plasmonic pressure sensor with Silicon-Insulator-Silicon waveguide configuration. *Optics Communications*, *578*, 131495. https://doi.org/10.1016/j.optcom.2025.131495

Takeda, Y., Wang, Y.-F., Yoshida, A., Sekine, T., Kumaki, D., & Tokito, S. (2024). Advancing Robotic Gripper Control with the Integration of Flexible Printed Pressure Sensors. *Advanced Engineering Materials*, *26*(9), 2302031. https://doi.org/10.1002/adem.202302031

Tan, Y., Liu, X., Tang, W., Chen, J., Zhu, Z., Li, L., Zhou, N., Kang, X., Xu, D., Wang, L., Wang, G., Tan, H., & Li, H. (2022). Flexible Pressure Sensors Based on Bionic Microstructures: From Plants to Animals. *Advanced Materials Interfaces*, *9*(5), 2101312. https://doi.org/10.1002/admi.202101312

Tang, X., Yang, J., Luo, J., Cheng, G., Sun, B., Zhou, Z., Zhang, P., & Wei, D. (2024). A graphene flexible pressure sensor based on a fabric-like groove structure for high-resolution tactile imaging. *Chemical Engineering Journal*, *495*, 153281. https://doi.org/10.1016/j.cej.2024.153281

Tchantchane, R., Zhou, H., Zhang, S., Dunn, A., Sariyildiz, E., & Alici, G. (2025). Advancing Human–Machine Interface (HMI) through Development of a Conductive-Textile Based Capacitive Sensor. *Advanced Materials Technologies*, *10*(6), 2401458. https://doi.org/10.1002/admt.202401458

Tian, S., Wang, L., & Zhu, R. (2024). A flexible multimodal pulse sensor for wearable continuous blood pressure monitoring. *Materials Horizons*, *11*(10), 2428-2437. https://doi.org/10.1039/D3MH01999C

Usman, M., Jamhour, N., Hettinger, J., & Xue, W. (2023). Smart Wearable Flexible Temperature Sensor with Compensation against Bending and Stretching Effects. *Sensors and Actuators A: Physical*, *353*, 114224. https://doi.org/ARTN 114224 10.1016/j.sna.2023.114224

Wang, B., Shi, Y., Li, H., Hua, Q., Ji, K., Dong, Z., Cui, Z., Huang, T., Chen, Z., Wei, R., Hu, W., & Shen, G. (2024). Body-Integrated Ultrasensitive All-Textile Pressure Sensors for Skin-Inspired Artificial Sensory Systems. *Small Science*, *4*(9), 2400026. https://doi.org/10.1002/smsc.202400026

Wang, C., He, T., Zhou, H., Zhang, Z., & Lee, C. (2023). Artificial intelligence enhanced sensors - enabling technologies to next-generation healthcare and biomedical platform. *Bioelectronic Medicine*, *9*(1), 17. https://doi.org/10.1186/s42234-023-00118-1

Wang, D., Li, B., Ma, Z., Zhang, C., Liu, L., Niu, S., Han, Z., & Ren, L. (2025). Capacitive pressure sensors based on bioinspired structured electrode for human-machine interaction applications. *Biosensors and Bioelectronics*, *271*, 117086. https://doi.org/10.1016/j.bios.2024.117086

Wang, D., Ma, G., Zhang, X., Zheng, K., Zhang, J., Ma, Z., Han, Z., & Ren, L. (2025). Flexible Pressure Sensor Composed of Multi-Layer Textile Materials for Human–Machine Interaction Applications. *ACS Sensors*, *10*(1), 350-359. https://doi.org/10.1021/acssensors.4c02583

Wang, L., Jiang, K., & Shen, G. (2021). Wearable, Implantable, and Interventional Medical Devices Based on Smart Electronic Skins [https://doi.org/10.1002/admt.202100107].

Advanced Materials Technologies, *6*(6), 2100107. https://doi.org/https://doi.org/10.1002/admt.202100107

Wang, L., Jones, D., Chapman, G. J., Siddle, H. J., Russell, D. A., Alazmani, A., & Culmer, P. (2020). A Review of Wearable Sensor Systems to Monitor Plantar Loading in the Assessment of Diabetic Foot Ulcers. *IEEE Transactions on Biomedical Engineering*, *67*(7), 1989-2004. https://doi.org/10.1109/TBME.2019.2953630

Wang, R., Du, Y., Wan, X., Xu, J., & Chen, J. (2025). On-Mask Magnetoelastic Sensor Network for Self-Powered Respiratory Monitoring. *ACS Nano*, *19*(29), 26862-26870. https://doi.org/10.1021/acsnano.5c07614

Wang, S. Y., Chen, X. L., Li, S., Sun, B., Chen, X. M., Tian, H. M., Wang, C. H., Li, X. M., & Shao, J. Y. (2025). Advances in micro/nano-engineered flexible sensor arrays for intelligent human-machine interaction. *Soft Science*, *5*(3), 28. https://doi.org/10.20517/ss.2025.11

Wang, W. C., Ledoux, W. R., Huang, C. Y., Huang, C. S., Klute, G. K., & Reinhall, P. G. (2008). Development of a Microfabricated Optical Bend Loss Sensor for Distributive Pressure Measurement. *IEEE Transactions on Biomedical Engineering*, *55*(2), 614-625. https://doi.org/10.1109/TBME.2007.912627

Wang, W. C., Ledoux, W. R., Sangeorzan, B. J., & Reinhall, P. G. (2005). A shear and plantar pressure sensor based on fiber-optic bend loss [Article]. *Journal of Rehabilitation Research and Development*, *42*(3), 315-325. https://doi.org/10.1682/JRRD.2004.07.0076

Wang, X., Kang, S., Dai, Z., Li, H., Guo, J., Zeng, Q., Tang, D., Wang, Z., & Wang, G. (2025). Flexible electrospinning pressure sensing film with wide pressure detection range and high sensitivity. *The Journal of The Textile Institute*, *116*(1), 71-79. https://doi.org/10.1080/00405000.2024.2316418

Wang, Y., Gao, Z., Wu, W., Xiong, Y., Luo, J., Sun, Q., Mao, Y., & Wang, Z. L. (2025). TENG-Boosted Smart Sports with Energy Autonomy and Digital Intelligence. *Nano-Micro Letters*, *17*(1), 265. https://doi.org/10.1007/s40820-025-01778-1

Wang, Z. L., & Song, J. (2006). Piezoelectric Nanogenerators Based on Zinc Oxide Nanowire Arrays. *Science*, *312*(5771), 242-246. https://doi.org/10.1126/science.1124005

Wei, C., Xu, Y., Hu, Y., Zhang, Q., Wei, N., Zeng, W., & Wu, R. (2025). Ti3C2Tx MXene paper-based flexible wearable pressure sensor with wide pressure detection range for human motion detection. *Journal of Alloys and Compounds*, *1017*, 179126. https://doi.org/10.1016/j.jallcom.2025.179126

Wen, C., Dematties, D., & Zhang, S.-L. (2021). A Guide to Signal Processing Algorithms for Nanopore Sensors. *ACS Sensors*, *6*(10), 3536-3555. https://doi.org/10.1021/acssensors.1c01618

Wu, W. (2019). Stretchable electronics: functional materials, fabrication strategies and applications. *Science and Technology of Advanced Materials*, *20*(1), 187-224. https://doi.org/10.1080/14686996.2018.1549460

Xie, X., Wang, Q., Zhao, C., Sun, Q., Gu, H., Li, J., Tu, X., Nie, B., Sun, X., Liu, Y., Lim, E. G., Wen, Z., & Wang, Z. L. (2024). Neuromorphic Computing-Assisted Triboelectric Capacitive-Coupled Tactile Sensor Array for Wireless Mixed Reality Interaction. *ACS Nano*, *18*(26), 17041-17052. https://doi.org/10.1021/acsnano.4c03554

Xu, C., Chen, J., Zhu, Z., Liu, M., Lan, R., Chen, X., Tang, W., Zhang, Y., & Li, H. (2024). Flexible Pressure Sensors in Human–Machine Interface Applications. *Small*, *20*(15), 2306655. https://doi.org/10.1002/smll.202306655

Xu, D., Zhou, P., Wu, J., Xiang, G., Zhong, Y., Guo, H., Zhang, X., Xia, Y., Yu, H., & Liu, L. (2025). Recent Progress in High-performance Flexible Pressure Sensors: Materials, Design, Fabrication, and Applications. *Advanced Materials Technologies*, *10*(15), 2500192. https://doi.org/10.1002/admt.202500192

Xu, H.-C., Liu, Y., Mo, Y.-P., Chen, Z.-Y., Pan, X.-J., Bao, R.-R., & Pan, C.-F. (2025). All-fiber anti-jamming capacitive pressure sensors based on liquid metals. *Rare Metals*, *44*(7), 4839-4850. https://doi.org/10.1007/s12598-024-03071-3

Xu, J., Duan, C., Wan, X., Che, Z., Zhao, X., Zhou, Y., Song, Y., Yin, J., Tat, T., Li, S., & Chen, J. (2025). A soft magnetoelastic sensor to decode levels of fatigue. *Nature Electronics*, *8*(8), 709-720. https://doi.org/10.1038/s41928-025-01418-x

Xu, J., Xue, Y., Xu, W., Li, X., Su, W., Fan, J., Ma, Y., & Han, D. (2025). Flexible Pressure Sensors for Optimizing Pressure Garment Therapy in Periarticular Scar Treatment: Preclinical and Clinical Applications. *Advances in Wound Care*. https://doi.org/10.1089/wound.2024.0139

Xue, Z., Gai, Y., Wu, Y., liu, Z., & Li, Z. (2024). Wearable mechanical and electrochemical sensors for real-time health monitoring. *Communications Materials*, *5*(1), 211. https://doi.org/10.1038/s43246-024-00658-2

Yan, J., Chen, A., & Liu, S. (2024). Flexible sensing platform based on polymer materials for health and exercise monitoring. *Alexandria Engineering Journal*, *86*, 405-414. https://doi.org/10.1016/j.aej.2023.11.085

Yan, L., Dillard, D. A., West, R. L., Lower, L. D., & Gordon, G. V. (2010). Mullins effect recovery of a nanoparticle-filled polymer Part B Polymer physics.

Yang, J.-S., Chung, M.-K., Yoo, J.-Y., Kim, M.-U., Kim, B.-J., Jo, M.-S., Kim, S.-H., & Yoon, J.-B. (2025). Interference-free nanogap pressure sensor array with high spatial resolution for wireless human-machine interfaces applications. *Nature Communications*, *16*(1), 2024. https://doi.org/10.1038/s41467-025-57232-8

Yang, W., Qin, Y., Wang, Z., Yu, T., & Ge, Z. (2022). Recent Advances in the Development of Flexible Sensors: Mechanisms, Materials, Performance Optimization, and Applications. *Journal of Electronic Materials*, *51*(12), 6735-6769. https://doi.org/10.1007/s11664-022-09922-y

Yang, Z., Wang, Q., Yu, H., Xu, Q., Li, Y., Cao, M., Dhakal, R., Li, Y., & Yao, Z. (2024). Self-Powered Biomimetic Pressure Sensor Based on Mn–Ag Electrochemical Reaction for Monitoring Rehabilitation Training of Athletes. *Advanced Science*, *11*(25), 2401515. https://doi.org/10.1002/advs.202401515

Yao, Z., Wu, W., Gao, F., Gong, M., Zhang, L., Wang, D., Guo, B., Zhang, L., & Lin, X. (2025). Flexible Tactile Sensing Systems: Challenges in Theoretical Research Transferring to Practical Applications. *Nano-Micro Letters*, *18*(1), 37. https://doi.org/10.1007/s40820-025-01872-4

Yassin, M. H., Farhat, M. H., Soleimanpour, R., & Nahas, M. (2024). Fiber Bragg grating (FBG)-based sensors: a review of technology and recent applications in structural health monitoring (SHM) of civil engineering structures. *Discover Civil Engineering*, *1*(1), 151. https://doi.org/10.1007/s44290-024-00141-4

Ye, X. W., Su, Y. H., & Han, J. P. (2014). Structural Health Monitoring of Civil Infrastructure Using Optical Fiber Sensing Technology: A Comprehensive Review. *The Scientific World Journal*, *2014*, 652329. https://doi.org/10.1155/2014/652329

Yip, M., Da He, D., Winokur, E., Balderrama, A. G., Sheridan, R., & Ma, H. (2009). A flexible pressure monitoring system for pressure ulcer prevention. 2009 Annual International Conference of the IEEE Engineering in Medicine and Biology Society,

Yoon, J., Moon, A., & Son, S. W. (2024). Effective Posture Classification Using Statistically Significant Data From Flexible Pressure Sensors. *IEEE Journal on Flexible Electronics*, *3*(5), 173-180. https://doi.org/10.1109/JFLEX.2024.3400151

Yousefi, R., Ostadabbas, S., Faezipour, M., Farshbaf, M., Nourani, M., Tamil, L., & Pompeo, M. (2011). Bed posture classification for pressure ulcer prevention. 2011 Annual International Conference of the IEEE Engineering in Medicine and Biology Society,

Yu, M., Zhang, Y., Han, Y., & Zhang, Y. (2022, 2022/12/09/11). Flexible Pressure Sensors and Their Applications in Wearable Electronics. 2022 4th International Academic Exchange Conference on Science and Technology Innovation (IAECST),

Yu, S., Xu, Y., Cao, Z., Huang, Z., Wang, H., Yan, Z., Wei, C., Guo, Z., Chen, Z., Zheng, Y., Liao, Q., Liao, X., & Zhang, Y. (2025). Alterable Robotic Skin Using Material Gene Expression Modulation. *Advanced Functional Materials*, *35*(11), 2416984. https://doi.org/10.1002/adfm.202416984

Yuan, Y., Xu, H., Zheng, W., Liu, M., Li, S., Yan, J., Wang, D., Liu, K., Zhang, H., Chen, G., Wang, W., Wu, G., Xue, C., Cheng, H., & Gao, L. (2024). Bending and Stretching-Insensitive, Crosstalk-Free, Flexible Pressure Sensor Arrays for Human-Machine Interactions. *Advanced Materials Technologies*, *9*(5), 2301615. https://doi.org/10.1002/admt.202301615

Zahid, A., Dai, B., Hong, R., & Zhang, D. (2017). Optical properties study of silicone polymer PDMS substrate surfaces modified by plasma treatment. *Materials Research Express*, *4*(10), 105301. https://doi.org/10.1088/2053-1591/aa8645

Zavanelli, N., Lee, Y. J., Kim, M., Bateman, A., Guess, M., Kim, H., Patel, D. K., & Yeo, W.-H. (2025). Stretchable Wearable Wireless Bioelectronics Using All Printed Pressure Sensors and Strain Gauges. *Advanced Materials Technologies*, *10*(3), 2400998. https://doi.org/10.1002/admt.202400998

Zeng, H., He, Y., Zhao, R., Li, Z., Wang, W., Yang, M., Li, P., Tao, G., Sun, J., & Hou, C. (2024). Intelligent health and sport: An interplay between flexible sensors and basketball. *iScience*, *27*(3), 109089. https://doi.org/10.1016/j.isci.2024.109089

Zhang, H., Chen, X., Liu, Y., Yang, C., Liu, W., Qi, M., & Zhang, D. (2024). PDMS Film-Based Flexible Pressure Sensor Array with Surface Protruding Structure for Human Motion Detection and Wrist Posture Recognition. *ACS Applied Materials & Interfaces*, *16*(2), 2554-2563. https://doi.org/10.1021/acsami.3c14036

Zhang, H., Fang, Y., Lee, J., Jeong, C. K., & Zhang, Y. (2024). Templates-Built Structural Designs for Piezoelectrochemical Pressure Sensors. *ACS Applied Materials & Interfaces*, *16*(45), 62617-62626. https://doi.org/10.1021/acsami.4c12507

Zhang, J.-w., Zhang, Y., Li, Y.-y., & Wang, P. (2022). Textile-Based Flexible Pressure Sensors: A Review. *Polymer Reviews*, *62*(1), 65-94. https://doi.org/10.1080/15583724.2021.1901737

Zhang, S., Feng, W., Jiang, Y., Li, Y., Liu, Y., Yu, D., & Wang, W. (2024). Flexible pressure sensor based on 3D printing MXene@dual-scale porous polymer. *Chemical Engineering Journal*, *498*, 155356. https://doi.org/10.1016/j.cej.2024.155356

Zhang, W., Ni, X., Wang, J., Ai, F., Luo, Y., Yan, Z., Liu, D., & Sun, Q. (2019). Microstructured Optical Fiber Based Distributed Sensor for In Vivo Pressure Detection. *Journal of Lightwave Technology*, *37*(9), 1865-1872. https://doi.org/10.1109/JLT.2019.2894299

Zhang, X., Zheng, J., Zhu, Z., Hu, C., Peng, H., & Liu, B. (2024). Transparent, Flexible Nanoporous Sensors with Humidity and Pressure Sensing Capabilities for Sports Health Status Monitoring. *ACS Applied Nano Materials*, *7*(17), 21209-21220. https://doi.org/10.1021/acsanm.4c04697

Zhang, Z., Zhang, Z., Mei, D., & Wang, Y. (2025). Multifunctional flexible sensor with both contact pressure sensing and internal ultrasonic detection for robotic grasping. *Sensors and Actuators A: Physical*, *383*, 116202. https://doi.org/10.1016/j.sna.2025.116202

Zhao, H., O'Brien, K., Li, S., & Shepherd, R. F. (2016). Optoelectronically innervated soft prosthetic hand via stretchable optical waveguides. *Science Robotics*, *1*(1), eaai7529. https://doi.org/10.1126/scirobotics.aai7529

Zhao, J., Yang, Y., Bo, L., Qi, J., & Zhu, Y. (2024). Research Progress on Applying Intelligent Sensors in Sports Science. *Sensors*, *24*(22). https://doi.org/10.3390/s24227338

Zhao, L., Lin, Z., & Lai, K. W. C. (2024). Skin-Integrated, Stretchable Electronic Skin for Human Motion Capturing and Pressure Mapping. *Advanced Sensor Research*, *3*(1), 2300025. https://doi.org/10.1002/adsr.202300025

Zhao, X., Zhao, S., Zhang, X., & Su, Z. (2023). Recent progress in flexible pressure sensors based on multiple microstructures: from design to application. *Nanoscale*, *15*(11), 5111-5138. https://doi.org/10.1039/D2NR06084A

Zhao, Z., Tang, J., Yuan, J., Li, Y., Dai, Y., Yao, J., Zhang, Q., Ding, S., Li, T., Zhang, R., Zheng, Y., Zhang, Z., Qiu, S., Li, Q., Gao, B., Deng, N., Qian, H., Xing, F., You, Z., & Wu, H. (2022). Large-Scale Integrated Flexible Tactile Sensor Array for Sensitive Smart Robotic Touch. *ACS Nano*, *16*(10), 16784-16795. https://doi.org/10.1021/acsnano.2c06432

Zhen, L., Cui, M., Bai, X., Jiang, J., Ma, X., Wang, M., Liu, J., & Yang, B. (2024). Thin, flexible hybrid-structured piezoelectric sensor array with enhanced resolution and sensitivity. *Nano Energy*, *131*, 110188. https://doi.org/10.1016/j.nanoen.2024.110188

Zhi, Y., Zhang, H., Zhang, L., Li, Q., Kuang, X., Wu, W., Zhou, Q., Li, P., Li, W., & Zhang, H. (2025). Pressure Sensors Based on Densely Structured Graphene Fibers for Motion Monitoring. *Advanced Fiber Materials*, *7*(2), 541-553. https://doi.org/10.1007/s42765-024-00502-9

Zimmermann, C. A., Amouzou, K. N., Sengupta, D., Kumar, A., Demarquette, N. R., & Ung, B. (2024). Novel elastomeric spiropyran-doped poly(dimethylsiloxane) optical waveguide for UV sensing. *Frontiers of Optoelectronics*, *17*(1), 21. https://doi.org/10.1007/s12200-024-00124-4

Zimmermann, C. A., Amouzou, K. N., & Ung, B. (2025). Recent Advances in PDMS Optical Waveguides: Properties, Fabrication, and Applications. *Advanced Optical Materials*, *13*(1), 2401975. https://doi.org/https://doi.org/10.1002/adom.202401975